2019-08-01

Search for Dwarf Emission Line Galaxies in Galaxy Voids

Christian D. Draper
Brigham Young University

Search for Dwarf Emission Line Galaxies in Galaxy Voids

Christian D. Draper

A dissertation submitted to the faculty of
Brigham Young University
in partial fulfillment of the requirements for the degree of

Doctor of Philosophy

J. Ward Moody, Advisor
Michael Joner
Denise Stephens
Eric Hintz
Darin Ragozzine

Department of Physics and Astronomy

Brigham Young University

ABSTRACT

Search for Dwarf Emission Line Galaxies in Galaxy Voids

Christian D. Draper
Department of Physics and Astronomy, BYU
Doctor of Philosophy

The population and formation of dwarf galaxies, $M_{r'} > -14$, contain clues about the nature of dark matter. The best place to search for these dwarf galaxies without influence from nearby large galaxies is within galaxy voids, where no galaxies have yet been found. To search for this potential dwarf galaxy population we have developed and applied a new photometric technique. We use three redshifted $H\alpha$ filters, designated $H\alpha8$, $H\alpha12$, and $H\alpha16$, along with the Sloan broadband filters, g′, r′, and i′ to identify emission line galaxies. From the ratio of the object flux through the $H\alpha$ filters, $H\alpha12/H\alpha8$ and $H\alpha12/H\alpha16$, we are able to determine the distance to these galaxies and the strength of the emission line captured in the filter set. One problem with using just the three $H\alpha$ filters is that the system will be sensitive to any emission line which has been redshifted enough to fall within the set. Of particular concern are the [OII] and [OIII] lines which will contaminate the sample. To overcome this we use a color-color relation, g′ - r′ and r′ - i′, to help separate which type of emission has been detected. We have applied this method to search for galaxies within the void FN2 and FN8. From this we have found 23 candidate objects which could have $H\alpha$ emission placing them inside of the void. To better understand the population density dwarf galaxies through voids we have also modeled the population of objects which we will detect having $H\alpha$ emission compared to the contamination of back ground objects which we can then use to compare the density in the void with the mean galaxy density. We have also begun taking spectra of the emission objects, to ensure our method does detect emission line objects, to test how well the distance and emission strength determination is, and to begin identifying which type of emission we have detected. To date we have taken spectra on 6 objects. All 6 showed emission, 4 with [OII] and 2 with [OIII]. Though none was $H\alpha$ we formed a "pseudo-redshift" to determine the accuracy of our measurements. This shows that our method is accurate to -127 ± 204 km·sec^{-1}.

Keywords: galaxy void, dwarf galaxy, dark matter, large-scale structure

ACKNOWLEDGMENTS

Contents

List of Figures

List of Tables

Chapter 1

Introduction

It has been well established that matter is not evenly distributed on the largest scales. We have found that galaxies group together in galaxy clusters, which then group together into superclusters (see Figure 1.1). These groupings of galaxies create filaments, walls, and sheets, with regions with no galaxies found in between. These regions of nothing are known as voids. This overall structure is known as the large-scale structure (LSS). The LSS and its evolution over cosmic time holds keys to understanding cosmology, dark matter, and dark energy.

1.1 Formation of Large-Scale Structure

The seeds of the LSS were first formed during the initial formation of the universe. The current understanding of the beginning of the universe is known as the Big Bang. This states that all that we see of the universe began as a sudden expansion from a very dense, very hot state. During the very early time there were small quantum fluctuations in the distribution of matter. During the inflationary epoch, which started at 10^{-36} seconds after the Big Bang and ended at 10^{-32} seconds after the Big Bang, an energy level shift caused the entire universe to expand at a much greater rate than had happened previously, or has happened since. This extreme expansion caused the
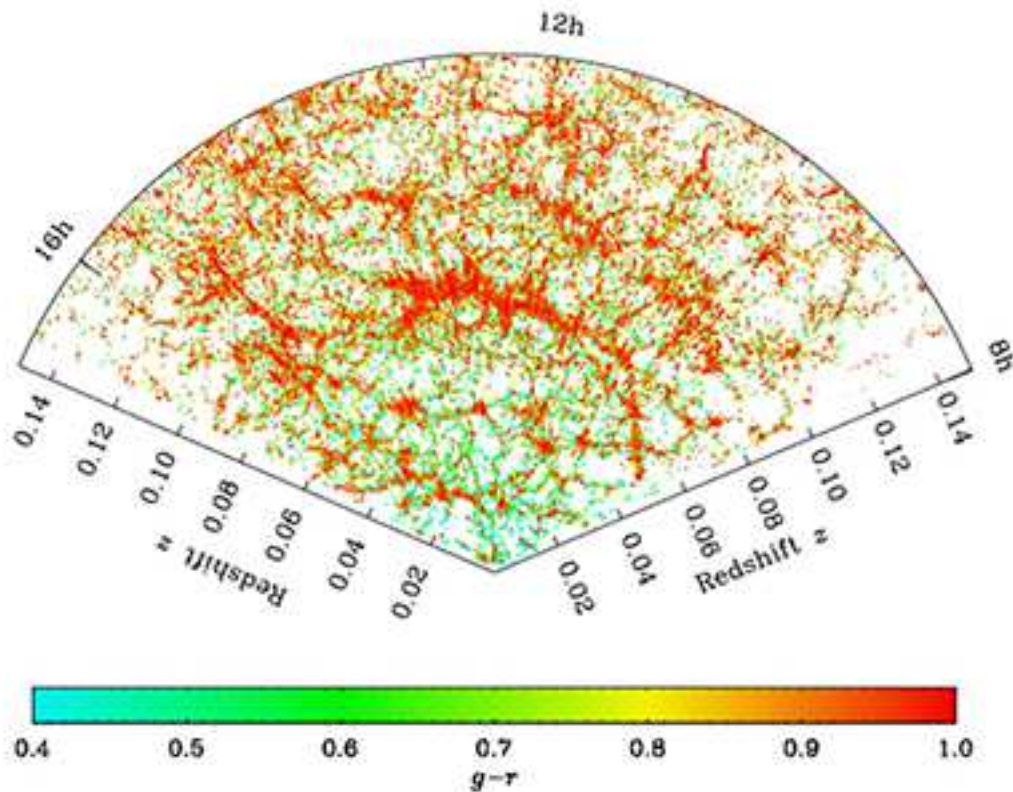
Figure 1.1 A plot of the distribution of galaxies in the north galactic cap with distance. This spans 8 hours in right ascension, 8° in declination and out a z of 0.15. Each dot corresponds to the position of a galaxy. Regions with many galaxies trace filaments. Regions with few galaxies show galaxy voids. The colors are related to the color of the galaxy, with redder dots being older galaxies, and green and blue being younger galaxies. It is interesting to note that the older galaxies tend to follow along the center of filaments and walls, with the younger galaxies around this core. Taken from (Zehavi et al. 2002)

quantum fluctuations to be increased to macroscopic scales. As this happened, it also lead to a general smoothing of the distribution of matter, to the point that the density difference between the most dense and least dense regions was around 1 part in 10,000. (Roos 2015)

As the universe continued to expand and cool, many different effects occurred. Due to the expansion of space itself the wavelength of light became stretched, making it redder than when it was first emitted. This process of reddening light is known as cosmological redshift, and still affects light traveling through the universe, because of the ongoing expansion of space. Also, as the universe cooled matter was able to form out of the concentrated energy. At first there was so much energy that particles of any mass were able to form. Then as the universe cooled, and light became less energetic due to cosmological redshifting, lower mass particles were able to form. It is presumed that during this time the dark matter of the universe formed. Starting at about 2 seconds after the Big Bang and continuing until about 10 minutes after, the entire universe was hot and dense enough to begin nuclear fusion. This fusion is the source of most of the universe's helium. Predictions of the primordial chemical abundance are a test of the Big Bang model, and have been confirmed in part leading to the widespread acceptance of this model. (Roos 2015)

During the next 380,000 years after the Big Bang, the entire universe was so hot that matter and light were completely intertwined. The temperature had not yet cooled off enough for the first atoms to form. Light was constantly interacting with the free charges from unbound electrons and atomic nuclei. Matter would be pulled into regions of higher dark matter concentration. As the matter became denser, the light pressure would increase causing the normal matter to then begin to expand again. The expansion lowered the pressure and once the pressure had decreased, the matter would then begin to collapse again into the regions of greater dark matter concentration. This is known as the baryon acoustic oscillations. (Weignberg et al. 2013)

1.2   Cosmic Microwave Background and Baryon Acoustic Oscillations

At 380,000 years after the Big Bang, the universe had cooled off enough that atoms were able to combine with nuclei for the first time. This is known as the period of recombination. As the free charges were becoming bound, this allowed light to break free of matter and begin streaming in straight lines over large distances for the first time. This produced the oldest light it is possible for us to detect, known as the Cosmic Microwave Background (CMB) (see Figure 1.2). When the light was first emitted from the CMB it was a blackbody spectrum peaking in the visible spectrum, but due to the expansion of space since that time until now, the peak is now in the microwave part of the spectrum. At the point where light and matter decoupled, the motion of the oscillations stopped, freezing in the distribution of matter. Regions of higher density appear hotter, regions of lower density appear cooler in Figure 1.2. Many features of the universe can be found by analyzing the angular scale of these regions. Fig. 1.3 shows the power spectrum of the baryon acoustic oscillations determined from the Planck satellite CMB measurements. The three largest peaks in the graph correspond to regions of oscillation which have reached some extreme. The first and tallest peak corresponds to matter that has just collapsed to its smallest size at the time of recombination. The second peak corresponds to regions which have collapsed, and then rebounded to their maximum expansion. The third peak corresponds to regions which have collapsed, rebounded, and have then re-collapsed to their minimum size again. The amplitude and angular size of these peaks contain great detail about the composition of our universe. (Weignberg et al. 2013)

The first peak in Figure 1.3 can be used to determine the total energy density. According to general relativity, the universe can have three possible shapes; spherical, flat and hyperbolic as determined by the total energy density of the universe. If the energy density is above a limit called the critical density, then the universe will be spherical. This means parallel lines will eventually
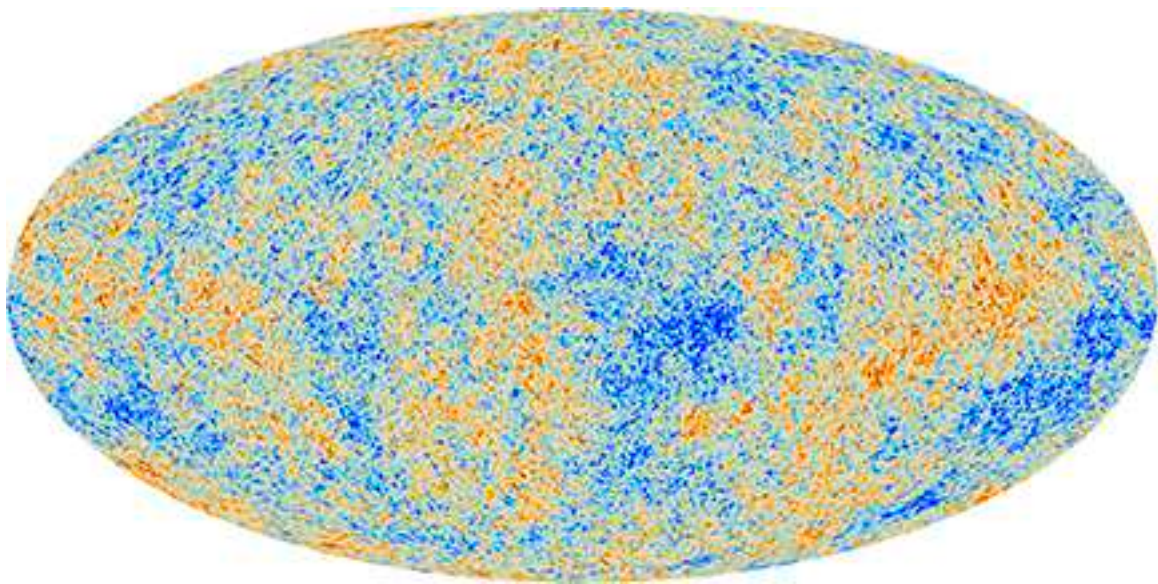
Figure 1.2 An image of the Cosmic Microwave Background from the Planck mission (Collaboration Accessed June 1, 2019). The color differences show differences in temperature and density from the time of re-ionization, about 380,000 years after the Big Bang. The redder the color the higher temperature and the density of matter in the region, the bluer the color, the lower and temperature and the density. This shows the seeds of what will become the large-scale structure of the universe. The high density regions will collapse due to gravity to form into galaxy clusters, filaments, walls and sheets. The low density regions regions will have material swept out forming into galaxy voids.

converge, like lines of longitude on the earth all converging at the poles. If the energy density is below the critical density, it will be hyperbolic. This means parallel lines will eventually diverge. If it is at the critical density the universe will be flat. In this case parallel lines will always remain parallel.

The regions of maximum collapse which correspond to the first peak in 1.3 will eventually form into the galaxy clusters of the modern universe. We can compare the size of galaxy clusters in the universe with the scale these high density regions must have had at the time of recombination to tell the overall shape, and therefore energy density of the universe. If the high density regions are too large, then light has converged causing a magnifying effect, so the universe is spherical. If the high density regions appear too small, light has diverged causing a minimizing effect, so the universe is hyperbolic. If the high density regions are the size we expect, then the light has traveled in straight lines and the universe has the critical density. Based on the scale we see in this power spectrum these regions are the size we expect, so the universe has the critical energy density. (Weignberg et al. 2013)

The second peak from the left in Figure 1.3 corresponds to the amount of baryonic matter. Baryonic matter is all of what we consider to be normal matter in the universe. Comparing the size of the first peak to the second shows that baryonic matter makes up about 5% of the total energy density. The rest of the peaks to the right determine the amount of dark matter to be 26.8%.

The distribution of matter from the time of the recombination, imprinted into the CMB, has then led to the LSS of the modern universe. The regions of higher density will continue to collapse forming into galaxy clusters, while regions of lower density will have material swept from them forming galaxy voids. Many computer simulations have been done to show this evolution of the LSS. Two of these are the Millennium Simulation (Springel et al. 2005) and the EAGLE simulation (Schaye et al. 2015). Both of these simulations began with data seeded from the distribution of matter determined from the variations in the CMB. The Millennium Simulation specifically showed
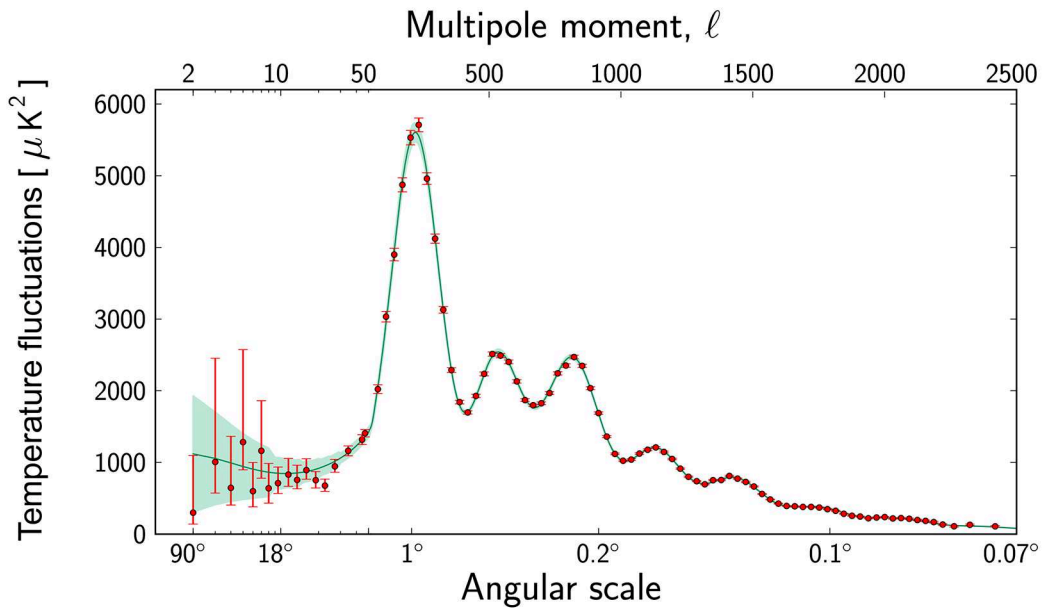
Figure 1.3 An image of the power spectrum of the baryon acoustic oscillations determined from the CMB (Collaboration Accessed June 3, 2019). The first from the left shows the total energy density of the universe, the total amount of dark energy, dark matter and baryonic matter. This also is used to show that the universe is flat. The second peak shows that baryonic matter makes up about 5% of the energy density of the universe. The smaller peaks to the left determine the ratio of dark matter to baryonic matter, showing that dark matter makes up about 26.8% of the energy density of the universe. (Weignberg et al. 2013)

how dark matter formed into the cosmic web. This simulation considered over 1 billion dark matter particles in a volume of 8 billion cubic light years. As the simulation evolved, a galaxy was assumed to form if the dark matter reached a particular density. Though this did not give an accurate view of the baryonic matter distribution on the small scale, it did show how the current cosmological model of cold dark matter with a cosmological constant (ΛCDM) leads to the LSS of the current universe. The EAGLE simulation not only tracked the dark matter but also included baryonic effects. In this way, the EAGLE simulation produced the large scale structure of the universe and also showed galaxy morphology and galaxy cluster-formation details.

Both of these simulations have been useful in determining the nature of the LSS and informing our understanding of galaxy voids. (Ceccarelli et al. 2013) formed a void catalog using data from the Millennium simulations, compared this catalog to the size and distribution of voids in the Sloan Digital Sky Survey (SDSS), (a survey of locations of galaxies in the LSS, Abazajian et al. 2009), and found good agreement between the two. Paillas et al. (2017) compared the void populations in the Millennium simulation with those of the EAGLE simulation and found that the dark-matter-only Millennium simulation produced more voids which also tended to be larger.

1.3   Dark Matter and Structure Formation

The interplay between galaxies and dark matter is obviously significant in galaxy-formation processes (Bullock & Boylan-Kolchin 2017). The exact nature of dark matter remains unknown at present, however we can determine some of its properties based on astronomical observations. One of the earliest observations which lead to the discovery of dark matter was the velocity dispersion of galaxies in rich galaxy clusters. Zwicky (1933) showed that the galaxies were moving too fast to be held together be the amount of luminous matter seen in the cluster. He posited that there must be extra matter which could not be seen, which was holding the cluster together. Further studies of the

rotation curves of galaxies also showed that there is more mass in a galaxy than what is detected by light, cementing the fact dark matter exists (Rubin et al. 1980).

The possibility of what dark matter could be tends to fall into two categories. The first idea is that it is objects made of normal matter that don't produce much light (White & Rees 1978). These are referred to as Massive Compact Halo Objects or MACHOs. Some possible candidates are brown dwarfs, objects with near stellar masses which didn't begin nuclear fusion, cold white dwarf stars, neutron stars and even black holes.

Detecting these objects is very difficult because they don't produce their own light. Instead we can look for micro-lensing events. According to general relativity, objects with mass are able to bend light. As a MACHO crosses between us and a distant star, the star's light will become focused onto the earth causing the distant star to appear brighter. As the MACHO moves away from out line of sight, the star dims back to its original brightness. This causes a tell-tale light curve. Alcock et al. (2000) did a 5.7 year long survey toward the Large Magellanic Cloud looking for these micro-lensing events. In that time they were able to find 13-17 events. This means that even taking the most generous assumptions about the population and detection rates, MACHOs can only make up to 20% of the dark matter within a galaxy, and it is far more likely that it is actually significantly lower. Simply, MACHOs cannot account for all, or even most, of the unseen mass.

The second possibility for what dark matter could be is Weakly Interacting Massive Particles, or WIMPs. WIMPs are subatomic particles which do not interact through the electromagnetic force. These could interact with the weak nuclear force or forces which are as yet unknown and weaker than the weak nuclear force. Many of the candidates for WIMPs come from extensions of the Standard Model of particle physics, which is our current model of all sub-atomic paricles (de Swart et al. 2017). Some possibilities are sterile neutrinos, neutrinos which don't interact in any way other than gravity, super-symmetric particles, particles predicted by super-symmetric theories and axions, a theoritical particle postulated to explain the lack of CP violation in strong nuclear interactions

(Frenk & White 2012).

Because MACHOs cannot explain dark matter, WIMPs are the source of most current investigations. WIMPs can be nicely organized into three categories based on the mass of the particle, which will correspond to when the particle decoupled from light at early times, and therefore determine the speed of the particles in the current universe. These are Hot Dark Matter (HDM), Warm Dark Matter (WDM), and Cold Dark Matter (CDM) (Bond et al. 1980). HDM are particles with masses in the 10's of eV and would have thermally decoupled at relatively late times, and are therefore still relativistic. WDM have masses in the keV range and would have thermally decoupled at an earlier time so they are no longer relativistic. CDM have masses in the GeV range and would have thermally decoupled at early times and would now be far below relativistic speeds. The dark matter's speed will determine the size of objects it can form as it collapses. HDM will produce dark matter halos with masses on the scale of galaxy super clusters. WDM will form halos with masses in the range of dwarf galaxies. CDM will produce dark matter halos with masses on the scale of the Earth (Frenk & White 2012).

WIMPs are presumed to be so weakly interacting that they do not interact significantly even with themselves, similar to neutrinos. However, (Carlson et al. 1992) have proposed that the dark matter may not interact strongly with normal, or baryonic, matter, but may interact strongly with itself. This type of dark matter is called Self-Interating dark matter, (SIDM).

The type of dark matter influences the degree to which it is able to collapse and therefore the overall large scale structure. These differences give a way to discriminate between the types of dark matter. Computer simulations by (White et al. 1983) showed that HDM formed top-down, meaning that large structures, like giant clouds the size of super clusters of galaxies formed first, then fragmented into smaller objects. Other simulations like the Millennium simulation (Springel et al. 2005) using CDM show that the structure formed bottom-up, meaning that smaller objects began forming first, and were then swept up into larger structures. See Figure 1.4 for differences in
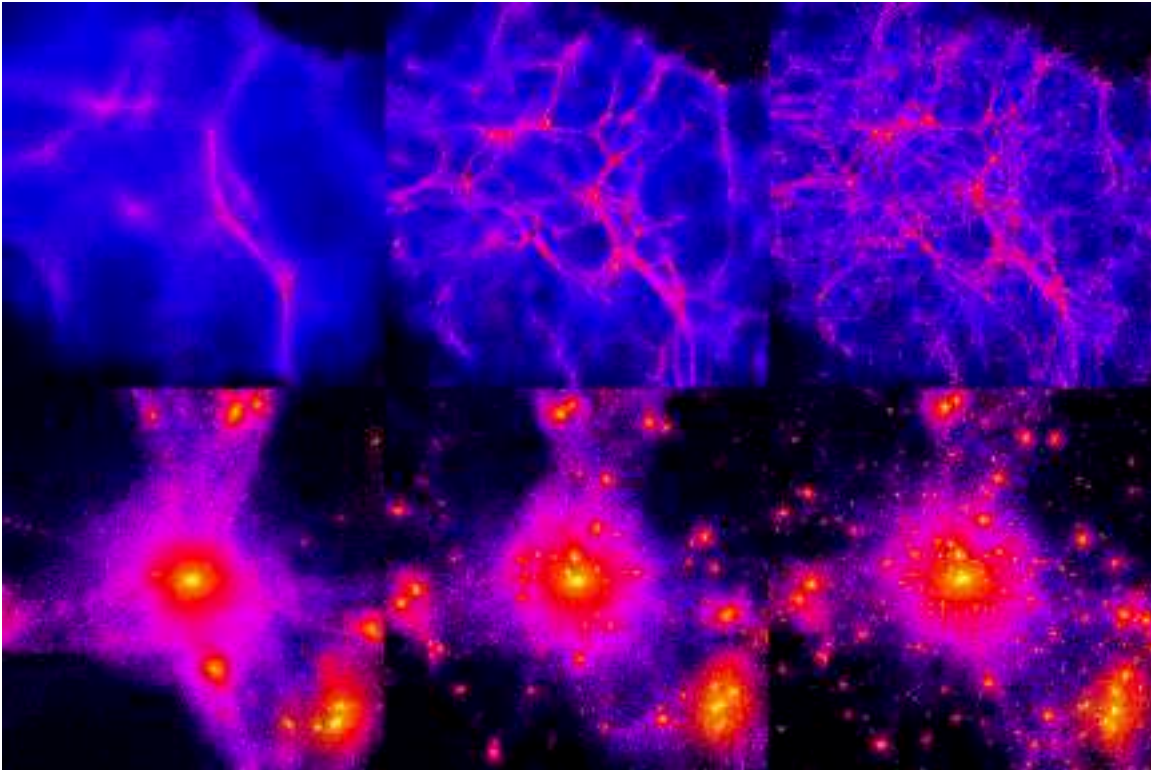
Figure 1.4 The formation of structure for Hot Dark Matter, Warm Dark Matter, and Cold Dark Matter. The top shows the distribution of matter at early times, from left to right are HDM, WDM, and CDM. Along the bottom are the structures at the present time in the same order as above. Note how in the top row HDM forms more diffuse structures, and WDM and CDM more defined. In the bottom row more smaller objects are formed in WDM and CDM. The HDM model has been ruled out based on observations of the present LSS (Zehavi et al. 2002). This image was originally produced by Ben Moore with the University of Zurich. (Mihos Accessed June 4, 2019)

the formation of structure for the different categories of dark matter.

Based off observations such as data from the Sloan Digital Sky Survey (Zehavi et al. 2002), HDM has been ruled out. The structure that it predicts does not match what we see. Both WDM, CDM, and SIDM trace out the overall "cosmic-web" which is seen in these large galaxy surveys. The currently accepted model for cosmology is ΛCDM, a universe dominated by dark energy, and cold dark matter.

1.4   Problems with Λ*CDM*

Though simulations using the Λ*CDM* model, such as the Millennium Simulation and EAGLE, have been successful on the large scale, there remain many questions and problems on smaller scales, the size of galaxies within galaxy clusters. Of particular interest is how dark matter affects the production of, and distributes through, dwarf galaxies. To begin understanding how the density fluctuations of the early universe form into galaxies at later times, Press & Schechter (1974) extended the linear collapse into the non-linear regime using a spherical collapse model. More recently, these ideas have been better developed (Sheth et al. 2001) forming the extended Press-Schechter models. Though this seems that it would produce poor modeling because it is a linear model in a non-linear regime, the size of the dark matter halos predicted match those found in the Millennium and other simulations.

Another interesting prediction from Λ*CDM* is the distribution of dark matter through galaxies. Based on simulations of galaxy formation in Λ*CDM*, the best description for the distribution density profile of dark matter is the Navarro-Frenk-White (NFW) functional form:

$$\rho(r) = \frac{4\rho_s}{(r/r_s)(1+r/r_s)^2} \tag{1.1}$$

(Navarro et al. 1997). ρ_s is a characteristic density at the point r_s. r_s corresponds to the transition point between the $\frac{1}{r}$ of the inner profile and the $\frac{1}{r^3}$ of the outer profile, which is a scale radius. However, when studying the motion of observed dwarf galaxies, a constant density profile is a better match. This difference between simulation and observation is known as the "cusp-core" problem. The computational modeling predicts a cusp, rising steeply at small radius, whereas the observed motion predicts a core of nearly uniform density (Walker & Penarrubia 2011).

Another well-known challenge to Λ*CDM* theory is the missing-satellite problem. According to Λ*CDM* simulations, there should be more satellite galaxies around large galaxies, such as our Milky Way, than are actually found. Λ*CDM* simulations of structure show that large dark matter halos

will have smaller sub-halos inside, many of which are large enough to host dwarf satellite galaxies around the large central galaxy. This suggests that there should be thousands of dwarf satellite galaxies around large galaxies like the Milky Way and the Andromeda galaxy. There are only around 50 known satellites of the Milky Way and 30 known satellite galaxies around Andromeda. (Garrison-Kimmel et al. 2014; Griffen et al. 2016).

An additional challenge to the standard Λ*CDM* model suggests there is more to the criteria for galaxy formation than the size of the dark matter halo, as was assumed in the Millennium Simulation. As shown by the missing satellite problem, simulations of dark matter sub-halos suggest there should be more galaxies within large sub-halos than what is actually seen. A solution to the missing-satellite problem is that below a certain mass the sub-halo cannot form a galaxy. When testing this idea on satellite galaxies in the local group, it was found that large sub-halos did not necessarily produce galaxies, but that there were some small sub-halos which did (Boylan-Kolchin et al. 2011; Tollerud et al. 2014). This discrepancy between the size of the dark matter sub-halo and galaxy formation is known as the "too-big-to-fail" problem.

One possible solution to these problems is different environments. Dawoodbhoy et al. (2018) show that re-ionization can dampen dwarf galaxy formation. In their simulation they modeled galaxy formation in a completely coupled radiation-hydrodynamic code. They found that the re-ionization of the inter-galactic medium suppressed star formation in satellite galaxies around large galaxies. Another possibility is that the Λ*CDM* model is incorrect and dark matter behaves differently than we currently understand. Yang et al. (2015) showed that a warm dark matter model produced fewer dwarf galaxies in galaxy clusters than have been predicted in CDM simulations. In Figure 1.4 it is possible to see this effect in comparing the far right panels, (which show simulations of CDM) with the middle panels (which show simulations of WDM). There are far fewer high density regions in WDM than in CDM. Similarly, SIDM may explain the "core-cusp" problem. Valli & Yu (2018) show that using interaction strengths between dark matter particles similar to what is measured in

baryonic matter, they are able to produce dark matter cores, instead of dark matter cusps, similar to what are observed in dwarf galaxy populations.

1.5 Measuring the Large-Scale Structure

It is difficult to disentangle the effects of dark matter from the environmental impact of nearby large galaxies on dwarf-galaxy formation. Therefore, it makes sense to explore regions where the galaxy population is low, such as in galaxy voids. Within these low density regions, dwarf galaxies presumably form with less ionizing influence from other galaxies. A greater reason for such a search is simply to understand how galaxy formation occurs in all different types of environments.

From a simple picture it is impossible to accurately determine the distance of astronomical objects. One of the mostly widely used methods for determining distances to other galaxies is by the redshift of the galaxy's spectrum. The spectrum of a galaxy is a blend of all the light produced by all of its constituent parts. There are stars of varying temperatures as well as the interstellar medium (ISM) made of gas and dust absorbing and emitting light.

Fig. 1.5 shows the spectra from 4 galaxies. The top left is from an elliptical E4 galaxy. These galaxies are characterized by an old population of stars and thin ISM. Because there is very little interstellar medium, there is no ongoing star formation, and therefore no way to replenish the short lived high-mass, high-temperature stars as they die out. The top right shows the spectrum of an Sa spiral galaxy. This type of galaxy tends to also have an older population of stars, with little star formation. The bottom left is the spectrum of an Sc galaxy. These galaxies contain large amounts of ISM, which leads to a large amount of star formation. This causes the blue end of the spectrum to produce more light. The star formation also produces many emission nebula, which then cause emission line features in the spectrum. The bottom right is a dwarf irregular galaxy. The overall spectrum is similar to the Sc, but irregulars tend to have even more star formation, producing even
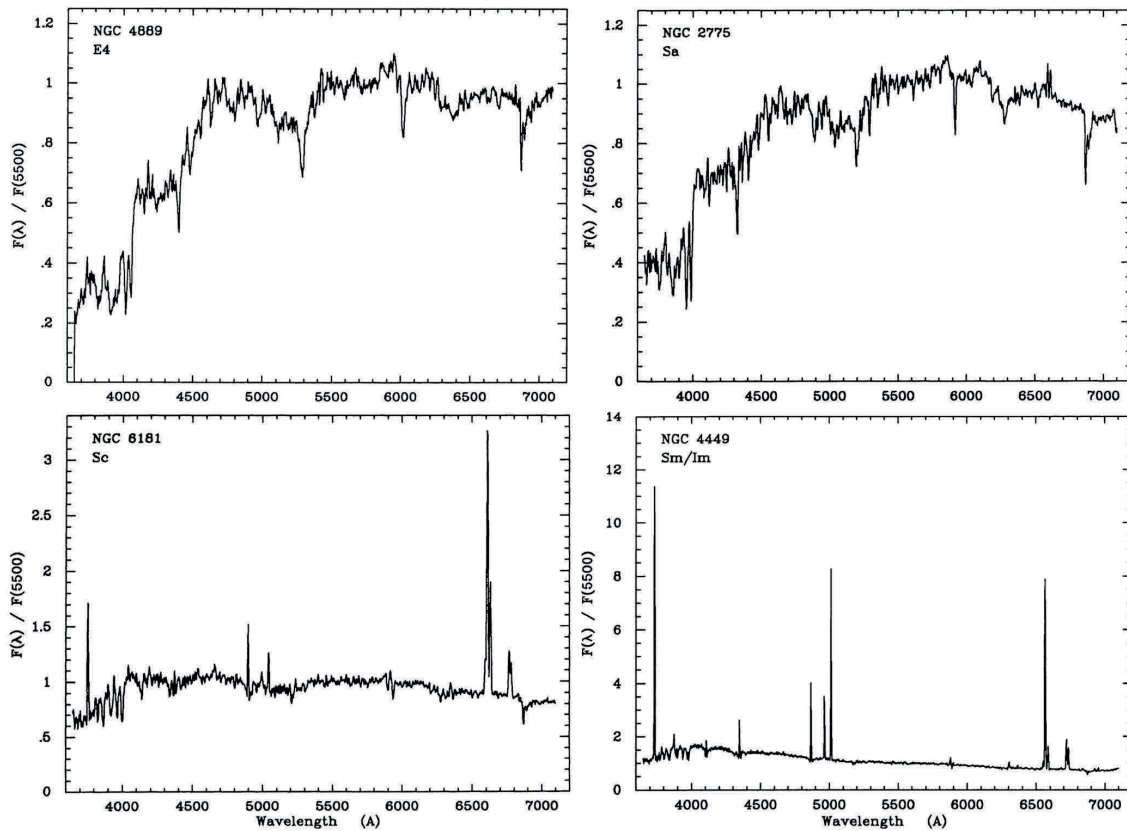
Figure 1.5 Four examples of galaxy spectra. The top left is the spectrum of an E4 elliptical galaxy. The spectrum is dominated by the emission from low-mass, cool stars. The top right is the spectrum of an Sa spiral galaxy. This is also dominated in the visible part of the spectrum by low-mass, cool stars similar to the E4. On the bottom left is the spectrum of an Sc spiral galaxy. The blue end (left side) of the spectrum is much stronger than in either the E4 or Sa. This galaxy has a large amount of interstellar medium, leading to strong star formation replenishing the hot blue stars. This also leads to emission nebulae, which cause strong emission features, such as the $H\alpha$ emission line at 6365 Å. The bottom right is the spectrum of a dwarf irregular galaxy. This galaxy has a large amount of ISM, and star formation similar to the Sa. However, the star formation is much stronger leading to more emission nebulae, and stronger emission features. Image taken from (Kennicutt 1992)

stronger emission line features in the spectrum (Kennicutt 1992).

As astronomers began taking spectra of galaxies, they found an interesting pattern. The farther away a galaxy was the more redshifted its spectrum was. At least for the nearby universe, the trend follows a linear pattern. This has been formally called the Hubble-Lemaitre Law. Specifically,

$$v = H_\circ D \qquad (1.2)$$

where v is the velocity of the galaxy measured in km·s^{-1}, H$_\circ$ is known as Hubble's constant measured in $\frac{km \cdot s^{-1}}{Mpc}$, and D is the distance to the galaxy measure in Mpc. (Roos 2015)

Recently the value for Hubble's constant has been under great debate. The primary mission of the Hubble Space Telescope was to determine the value for H$_\circ$ by identifying and determining the distance to Cepheid variable stars in other galaxies. Comparing the redshift with the luminosity of the stars gave a calibration for determining the distance with the redshift. Another method for determining the value of H$_\circ$ is by using the CMB. Assuming the ΛCDM model is correct, then the basic parameters of the energy density of the universe can be used to find the value for H$_\circ$. The current value for H$_\circ$ from Hubble is 74.03 $\pm$ 1.42 (Riess et al. 2019). The most recent data from the CMB pased on the Planck mission data is 67.66 $\pm$ 0.42 (Aghanim et al. 2018). The difference between these values has reached the 4.4σ level, meaning that the two cannot both be correct. This difference has started to be called the Hubble tension. There are no current definite explanations for this difference. For simplicity I'm going to assume a value for H$_\circ$ of 70 $\frac{km \cdot s^{-1}}{Mpc}$, splitting the difference with a nice round number.

At first the redshift detected from the light in these galaxies was assumed to be a Doppler shift. The wavelengths of light being stretched out because the galaxies are moving away from us, similar to how the sound of a car moving away has its wavelengths stretched causing it to sound lower pitched. It is now accepted that it is actually being caused by the expansion of space itself. As space expands it pushes galaxies away from each other. It is similar to a loaf of cinnamon bread with chocolate chips inside. As the entire loaf rises, the dough pushes the chocolate chips apart. Looking at Hubble's constant can help us understand exactly what is going on. For H$_\circ$ = 70 $\frac{km \cdot s^{-1}}{Mpc}$, as I've assumed, for every 1 Mpc away a galaxy is, it is being pushed away from us at 70 km·s^{-1}. So if it is 1 Mpc away, it is being pushed by space at 70 km·s^{-1}. At 2 Mpc, it will be pushed away at 140

km·s^{-1} and so. This expansion of space also stretches out the wavelength of light. This is known as cosmological redshift, and is the same cosmological redshift as that was mentioned previously in section 1.1. (Roos 2015)

Redshift is defined as

$$z = \frac{\lambda - \lambda_\circ}{\lambda_\circ} \tag{1.3}$$

with z being the redshift, λ the measured wavelength of the spectral feature, and $\lambda_\circ$ being the original wavelength of the spectral feature. For example, using the $H\alpha$ emission line which has an unshifted wavelength of at 6563 Å, and then measuring the feature to be redshifted to 6629 Å, we get z = 0.01. It is sometimes convenient to state the speed of a galaxy away from us, v in Hubble's Law, in terms of the redshift. For objects closer than a z of about 0.1 we often use v = cz, where c is the speed of light. For the above redshift, the galaxy would therefore have a speed cz = 3000 km·s^{-1} away from us.

Using the method of measuring the redshift of a galaxy's light is how many surveys determine the distance to galaxies. These types of surveys are known as redshift surveys. A noteworthy survey complete to a B mag limit of 15.5 was performed by the Harvard-Smithsonian Center for Astrophysics (CfA) in 1982 (Davis et al. 1982). This survey firmly established the cosmic-web morphology of the LSS. More recently the 2 degree Field Galaxy Redshift Survey (Colless et al. 2001) and the Sloan Digital Sky Survey (Zehavi et al. 2002) have expanded the overall structure of the LSS to a survey depth of 19.5 in R and 17.7 in the r'. As mentioned previously, the overall structure of the LSS from these surveys matches well with the Millennium and EAGLE simulations. However, these do not probe faint enough to find the the dwarf galaxies of interest within the large galaxy voids. These are regions which will help to discriminate between the different types of dark matter.

Dwarf galaxies are very dim and difficult to find, requiring long exposure times in photometric

surveys. Getting their spectra, to determine their distance, is very time consuming, which naturally means that few surveys have been able to probe to adequately faint limits. For example, the SDSS spectroscopic limit in r$'$ of 17.77 is sufficient to locate theoretically interesting dwarf galaxies with $M_{r'}$ = -14 only out to a z of 0.006. At a distance of z = 0.03, the limit is $M_{r'}$ = -18 which is less than 3 magnitudes below the magnitude of average or M_* galaxies. Well-defined, average-sized void centers are not reached until a z = 0.013 to 0.02. So the all-important cosmological test of either finding dwarf galaxies in the centers of voids or ruling out their existence has yet to be accomplished be these redshift surveys.

A method to determine distance solely photometrically will allow fainter objects to be found at a faster rate. Photometric surveys, where we image through various color filters, are able to probe larger parts of the sky and find fainter objects. Since the light is not spread out in wavelength, as happens when taking spectra, these methods are able to gather more light in the same amount of time. These are also able to be done using a wide field of view covering a relatively large area of the sky, increasing the speed of detection. The trade off is in the accuracy of the distance measurement. The SDSS's photometric uncertainties σ_z^{ph} are approximately 0.02 in z. This uncertainty translates to the width of well-defined galaxy voids, which have a diameter in z between 0.01 and 0.02, meaning that the error in the distance measurement is sufficient that it is not possible to positively identify if the object is in the void or not. To map the LSS to a greater depth and sufficient resolution more quickly, a more accurate photometric method is necessary.

My research has been to develop a photometric method, with significantly more accurate distance measurements, to allow us to search for the dwarf population within galaxy voids. Our idea is to search for galaxies which produce strong emission lines, like the Sc and dwarf irregular spectra found in Figure 1.5 using a set of three intermediate-band filters and the Sloan g$'$, r$'$, and i$'$ filters. The three intermediate-band filters have the profile of the $H\alpha$ filter, but have been redshifted by 8 nm, 12 nm, and 16 nm, see Figure 2.1. This redshift of the filters will allow the emission line to be

detected only if the galaxy has been sufficiently redshifted so the emission line falls within the set. Depending on where the emission line falls in the set will allow us to determine the redshift of the line and therefore determine the distance to that galaxy. The Sloan g′, r′, and i′ filters are necessary to distinguish which emission line feature has been detected, clearing any ambiguity.

Using intermediate and narrow band filters to search for hightly redshifted emission line objects has been used for decades. In the mid 1980's Djorgovski et al. (1985) used a filter centered at 5139 Å with a FWHM of 90 Å to search for redshifted Lymanα lines. This found a galaxy with z=3.2, which was compared to a near neighbor QSO. In 1996 Thompson et al. (1996) used the infrared J, H, and K′ filters to find galaxies with emission at z=2. In 2000 Rhoads et al. (2000) did a similar search to our method. This used filters centered at 6559 Å 6611 Å 6650 Å 6692 Å and 6730 Å. This searched for the Lymanα emission from galaxies at z=4.5. This also found galaxies with [OIII] emission at a redshift of z=0.34 though this was not the goal of the survey.

More recently Matthee et al. (2017) performed a narrow band filter survey in the infrared with 6 filters from 0.4-2.1 μm, searching for Lymanα galaxies from z=0.4 to 4.7. Specifically they were looking for luminosity evolution in star-forming galaxies. In a similar survey Ouchi et al. (2018) looked for mass and clustering evolution from z=5.7-6.6. Sobral et al. (2018) looked for galaxies with $H\alpha$ at z = 0.40, 0.89, 1.47, 2.23 to determine the evolution of galaxies with $H\alpha$ emission. particularly looking at the evolution of the characteristic luminosity L^*, and of the star formation rate history of the universe for the last 11 billion years.

All of these show that it is possible to identify faint objects through detection of emission line features using a set of intermediate band filters. All of this previous work has been developed to search at large z. We will apply similar methods to low z, searching for dwarf galaxies within nearby galaxy voids.

In this work, chapter 2 describes the methods of our technique, chapter 3, present the observations and data of our initial search for dwarf galaxies in nearby galaxy voids, and chapter 4, shows the

first spectra taken from candidate objects. Chapter 5 contains the conclusions.

Chapter 2

Methods

2.1 $H\alpha$ Filters

Our survey was designed around the capabilities of the KPNO Mayall 4-m telescope located at Kitt Peak National Observatory (KPNO) in Airzona, using the Wide Field Mosaic 1.1 Imager. KPNO possesses an excellent set of redshifted $H\alpha$ filters, the first four of which are designated k1010, k1011, k1012, and k1013. These filters are all approximately 80 Å wide and are centered at 6620.5, 6654.2, 6698.5, and 6730.7 Å respectively. Of these, the set of three filters with the largest shift (k1011, k1012, and k1013) capture the $H\alpha$ emission line for distances of 2300 km·s^{-1} < cz < 9200 km·s^{-1} (0.008 < z <0.031). Hereafter, I refer to these filters as $H\alpha8$ (k1011), $H\alpha12$ (k1012), and $H\alpha16$ (k1013). The number after "$H\alpha$" is the approximate shift of the filter from the original $H\alpha$ filter's center in nanometers. Traces of these filters with their bandpasses shifted appropriately for the f/3.1 Mayall 4m telescope + Mosaic 1.1 Wide Field Imager are given in Figure 2.1 (see http://www.noao.edu/kpno/mosaic/filters/.)

These three filters are appropriate for exploring the nearest well-defined voids. They are tuned especially well for the second and eighth entries in the void catalog of (Foster & Nelson 2009)
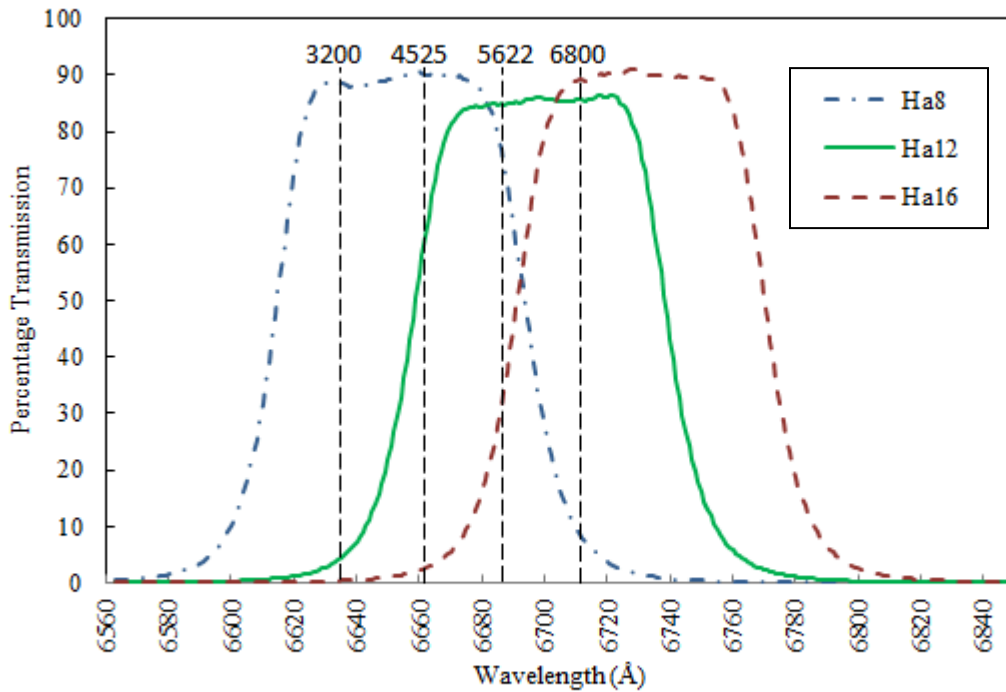
Figure 2.1 Transmission profiles for the redshifted $H\alpha$ filters $H\alpha 8$, $H\alpha 12$ and $H\alpha 16$. The NOAO filter names are k1011, k1012, and k1013, respectively. Along the horizontal axis is the wavelength of light in Angstroms. The vertical axis is the transmission percentage. Note that each of the filters have "wings", which overlap from one filter to the next. This will allow a comparison of the transmission percent in one filter to the next to determine the redshift of the detected emission line. These traces are modeled for the f/3.1 optics of the Mayall telescope (see http://www.noao.edu/kpno/mosaic/filters/). The vertical dashed lines correspond to different distances for which a hypothetical redshifted $H\alpha$ emission line would be detected measured in cz.

which we call "FN2" and "FN8" respectively. The center of FN2 is at $\alpha = $ 4h 2m, $\delta = 18° 50'$, and $cz = $ 4550 km·s^{-1} (z=0.0152), with a diameter of 3550 km·s^{-1} (z=0.0118). The center of FN8 is at $\alpha = $ 12h 50m, $\delta = 72° 40'$, and $cz = $ 4980 km·s^{-1} (z=0.0166) with a diameter of 3660 km·s^{-1} in redshift space (z=0.0122). Therefore, the void extends from 3140 km·s^{-1} $< cz <$ 6820 km·s^{-1} (0.0105<z<0.0227). The maximum transmission plateaus of the $H\alpha$8, $H\alpha$12, and $H\alpha$16 filters cover $H\alpha$ for 2600 km·s^{-1} $< cz <$ 8100 km·s^{-1} (0.009<z<0.027), meaning they are an ideal set for capturing $H\alpha$ at any distance within these voids as well as on the front and back sides.

Dwarf irregular galaxies with strong emission having $M_{r'} > -14.0$ are not thought to reside in voids. Any survey which looks to detect them, must be sensitive enough to detect these faint objects at least in the center of the void. To establish that dwarfs of this magnitude are *not* in a void, the survey depth should be faint enough to detect galaxies of a similar magnitude range as far as the back of the void. Therefore, our survey must be capable of detecting objects with $M_{r'} > -14.0$ at a distance of 8,000 km·s^{-1} (z=0.027). For an H_o of 70 km·s$^{-1}Mpc^{-1}$, this is an apparent magnitude in the Sloan r' filter of 21.3.

When beginning to model how we can use these filters to detect galaxies within these voids, our first approach was to simply try to determine which filter the emission was detected in. If it was in the $H\alpha$8 filter, then the galaxy would be on the near side of the void, if it was in the $H\alpha$12 filter it would be in the center of the void, and if it was in the $H\alpha$16 filter it would be in the far region of the void. This would only give a very coarse understanding of where the galaxy was located, but it did show that it was possible to start finding these faint objects within the void.

Upon further analysis we realized that the filters overlap, which would allow a more detailed position determination. If the object was only in the $H\alpha$8 filter it would be closer to us than the void. If it was in both $H\alpha$8 and $H\alpha$12 then it was in the void on the near side. If it was only in $H\alpha$12 it would be at the center of the void. If it was in both $H\alpha$12 and $H\alpha$16 it would be in the void on the far side. If it was only in the $H\alpha$16 filter then it would be beyond the void on the far side.

Then we noticed that the wings of the transmission of the filters made it possible to get an even more accurate measure of the distance. Depending on the redshift, the emission line will pass through different transmission regions of each filter changing its color index. to measure the change we formed a color-color relation from photon counts through each filter. A color-color plot, as used here, allows us to compare the brightness of the objects in three different filters.

Counts can be transformed into magnitude using $-2.5 * log_{10}(counts) + C$, where C is a constant determined by finding the magnitude of a standard star.We chose to work in count ratios rather than magnitude differences because it is what is actually measured from the detector. Color-color plots are usually made by plotting the magnitude difference in one pair of filters against the magnitude difference in another pair of filters. We therefore conducted our assessment using the quantities $Hα12/Hα8$ and $Hα12/Hα16$ which is equivalent to magnitude of $Hα12$ - magnitude of $Hα8$ and the magnitude of $Hα12$ - magnitude of $Hα16$. We assume that the throughput of objects without emission line features will be close to the same in each filter, so taking the ratio between the different filters as described above will give a number close to 1.0 with some scatter based on variations from a perfectly flat spectrum.

Of particular concern to us were late type stars. Stars are classified based on spectral types, O B A F G K and M. This is extended to include brown dwarfs with types L, T and Y. Each letter is then further divided by adding a number strating with 0 and going through 9, so O0, O1, O2 etc. This is a temperature sequence with O type stars being the very hottest, and M type stars being the very coolest, and the brown dwarfs being even cooler. The coolest stars and the brown dwarfs, have many absorption features which we were concerned would fall within the bandpasses and produce a signature we would mistake as an emission line. To investigate this we took sample spectra of M stars and L brown dwarfs and looked at their spectrum through the bandpasses of the $Hα$ filters. An example spectrum can be seen in Figure 2.2. The spectrum is for an L1 type brown dwarf and does remain flat through the filter bandpasses, showing that the ratios will be close to 1.0. Example

Hα Filters and L1 Star Spectrum
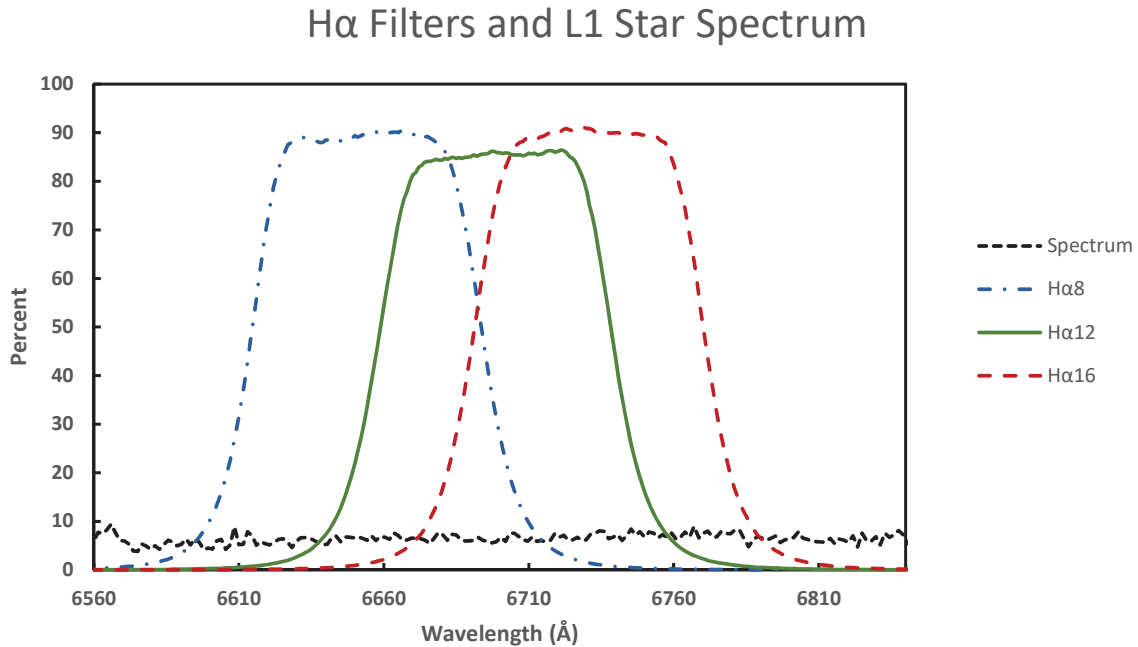
Figure 2.2 An example of a stellar spectrum passing through the three $H\alpha$ filter band-passes. The spectrum does remain flat through all three filters. This shows that the ratios $H\alpha12/H\alpha8$ and $H\alpha12/H\alpha16$ should remain near 1.0 for these types of stars. The spectrum compared with the transmission of the $H\alpha$ filters for the other types of stars of most concern to us can be found in appendix A.

spectra for these objects can be seen in appendix A. Random noise and seeing conditions will cause this population to form a bivariate normal distribution, which will allow us to remove these objects from those with emission line features.

Figure 2.3 shows a theoretical plot of $H\alpha12/H\alpha8$ vs $H\alpha12/H\alpha16$ for lines with equivalent widths of 50, 100, 200, and 1,000 Å. The equivalent width is a measure of the strength of an

absorption or emission line. On a graph of intensity vs. wavelength it is the width of a rectangle with the same area as the area of the spectral feature, with the height of the continuum. Formally,

$$W_\lambda = \int_{\lambda 1}^{\lambda 2} (1 - \frac{F_\lambda}{F_0}) d\lambda \qquad (2.1)$$

where F_0 is the flux of the continuum, F_λ is the intensity over the wavelength range $\lambda 1$ to $\lambda 2$, and W_λ is the equivalent width. As a feature increases in strength, the equivalent width will also increase. The large value of 1,000 Å EW was chosen as an upper limit, though there are rare galaxies which may produce stronger emission features. These curves were created by stepping a simulated $H\alpha$ line of the different equivalent widths through redshifts from 3,200 to 6,800 km·s^{-1}.

The counts detected will be related to the continuum and the strength of the emission line by

$$Counts = C * (EW_{line} * T + EW_{filter}) \qquad (2.2)$$

where C is the contribution from the continuum, EW_{line} is the equivalent width of the emission line, T is the transmission percent of the filter at the calculated redshifted wavelength of the $H\alpha$ emission line, and EW_{filter} is the equivalent width of the entire filter, which, in the case of the $H\alpha$ filters, is near 80 Å. So taking a galaxy with a continuum strength of 10, an $H\alpha$ emission equivalent width of 50, and redshifted to a cz of 4525 km·s^{-1} (z=0.015) we get a total count for the filter $H\alpha 8$ of

$$Counts = 10 * (50 * .90 + 80)$$

$$Counts = 1250.$$

Similarly for the $H\alpha 12$ filter

$$Counts = 10 * (50 * .61 + 80)$$

$$Counts = 1105$$

Table 2.1 This table contains modeled values for the number of counts in each of the $H\alpha$ filters detected from four hypothetical galaxies as well as the ratio of the counts for the different filters. The counts are determined from eq. 2.2. Each galaxy has a continuum of 10, and a transmission determined from the poition within the filter that the emission line is located. Two galaxies are modeled at a redshift of cz = 4525 km·s^{-1} with equivalent width of 50 and 500 Å, and two are modeled at a redshift of cz = 5622 km·s^{-1} again with equivalent width of 50 and 500 Å. Notice that the ratios for $H\alpha12/H\alpha8$ and $H\alpha12/H\alpha16$ shift farther away from the point (1.0, 1.0) with greater emission at both distances. Also, the values shift to larger values in $H\alpha12/H\alpha8$ with greater distance.

cz	4525 km·s^{-1}		5622 km·s^{-1}	
EW	50 Å	500 Å	50 Å	500 Å
$H\alpha8$	1250	5300	1302	5102
$H\alpha12$	1105	3850	1347	5547
$H\alpha16$	815	950	1045	2558
$H\alpha12/H\alpha8$	.75	0.72	1.034	1.087
$H\alpha12/H\alpha16$	1.13	4.05	1.289	2.152

and for the $H\alpha16$ filter

$$Counts = 10 * (50 * 0.03. + 80)$$

$$Counts = 815.$$

This will give an $H\alpha12/H\alpha8$ ratio of 0.75 and an $H\alpha12/H\alpha16$ of 1.13. Table 2.1 shows values for four hypothetical galaxies. Two at a cz of 4525 (z=0.015) with equivalent widths of 50 and 500, and two at a cz of 5622 (z=0.019) with equivalent widths of 50 and 500.

From the table of example modeled data we can see two trends. First, no matter the redshift, the stronger the emission, the farther from the point (1.0,1.0) the ratios become. The second, with greater redshift the value for $H\alpha12/H\alpha8$ shifts more to higher values. As will be discussed below this shows there is a direct correlation between the value of the ratios, $H\alpha12/H\alpha8$ and

$H\alpha12/H\alpha16$, and the galaxies redshift and equivalent width.

Stars and galaxies without emission in this range are expected to fall within the region close to the point (1.0, 1.0) as discussed above. The ellipse around this point shows the scatter from objects without strong emission and is estimated from the expected variation in stellar continuum slope through the filter range. The actual spread will additionally depend on the signal-to-noise level of the survey data.

2.2 Redshift, Equivalent Width, and Continuum Determination

Curves created by stepping the emission line through varying distances are shown in Figure 2.3. Note that the curves of different equivalent widths do not cross. Therefore, the placement of the bandpasses of the $H\alpha8$, $H\alpha12$, and $H\alpha16$ filters can form a relationship of $H\alpha12/H\alpha8$ vs $H\alpha12/H\alpha16$ which is uniquely determined by line equivalent width and redshift value. This relationship makes it possible to map $H\alpha12/H\alpha8$ vs $H\alpha12/H\alpha16$ onto both equivalent width and *cz*.

To do the equivalent width mapping, we first modeled the expected $H\alpha12/H\alpha8$ and $H\alpha12/H\alpha16$ ratios using the filter tracings from KPNO as discussed previously. We modeled them for discrete values of line equivalent widths in steps of 10 Å from 10 to 200 Å and in steps of 50 Å from 200 to 500 Å. We then made a look-up table of $H\alpha12/H\alpha8$ vs $H\alpha12/H\alpha16$ for values from 0.95 to 3.0 in each axis at a resolution of 0.05 (see appendix B for the equivalent width table and appendix C for the table for the cz distance). Not all steps contained values from the modelling step. We tried three different interpolation techniques. We started with a two-dimensional polynomial fit that assumed the two axes were independent. First we determined the values along one axis then along the other axis. The second method was a nearest neighbors approach, determining the value of missing data
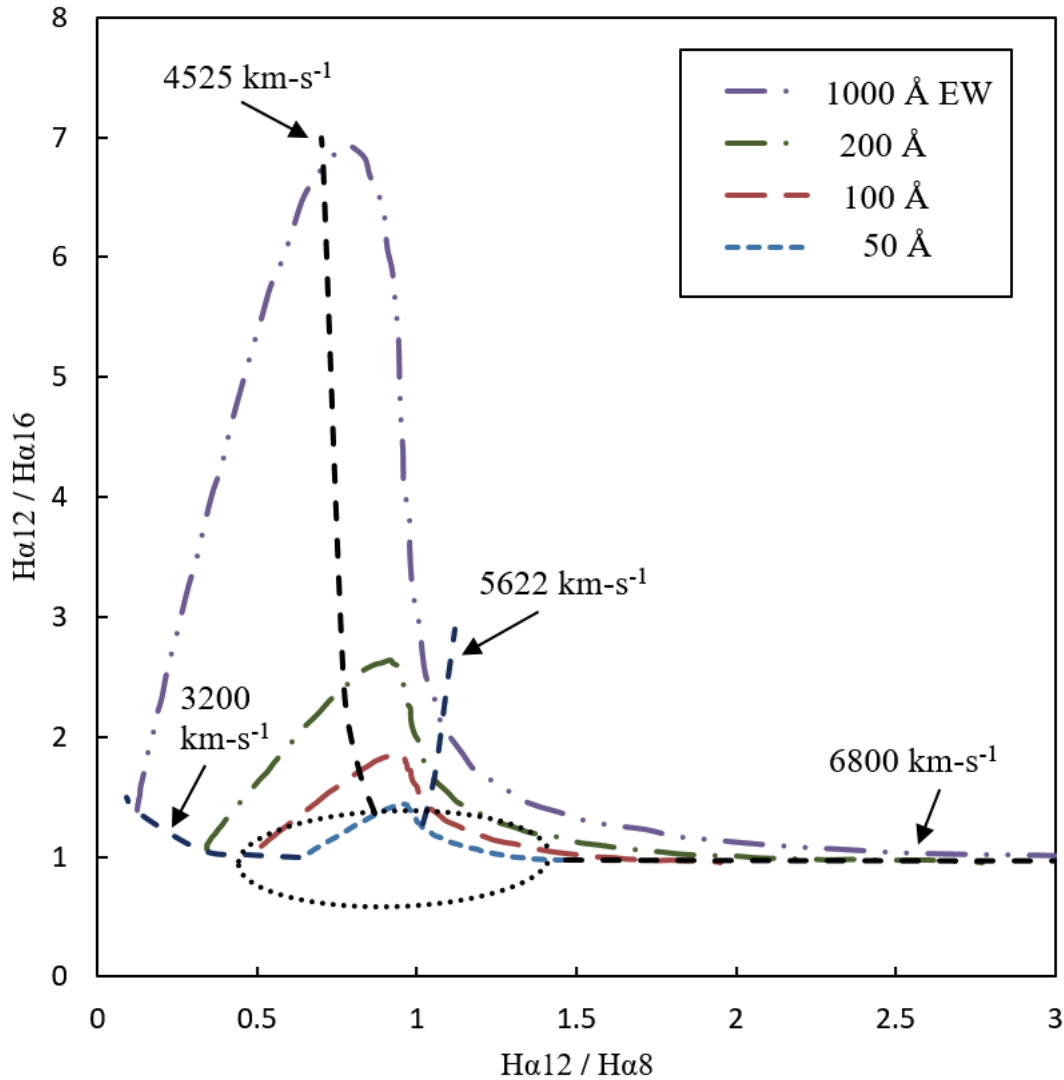
Figure 2.3 A plot showing the relationship between the $H\alpha12/H\alpha16$ and $H\alpha12/H\alpha8$ ratios for $H\alpha$ emission lines of various equivalent widths and at various redshifts. Four curves showing the relationship of the ratios as a function of redshift are given for lines of 50, 100, 200, and 1,000 Å equivalent width as indicated in the key. The strength of the line is related to the height of the curve. As the redshift is increased the values follow along the line from left to right. Four dashed black lines indicate the redshifts of the front edge of void FN8 (3,200 km·s^{-1}), one third through the void (4,525 km·s^{-1}), two thirds through the void (5,622 km·s^{-1}), and the back edge of the void (6,800 km·s^{-1}). The dotted region indicates the scatter of objects without emission features. The inherent scatter is such that objects must have an equivalent width greater than 50 Å to be detected at all and greater than 100 Å to be detected in the front and back void volume. Objects with emission greater than 50 Å equivalent width can be detected in the important central third of the void.

points based on the values of all the nearest neighbors. The third approach was a two dimensional spline. Based off spectra from actual galaxies discussed in chapter 4, it was determined that the first approach of a simple polynomial fit was the best fit to the real data. This was only determined based off 6 spectra, so this may change in the future as more spectra are taken. The *cz* mapping was done in the same way, assuming, of course, that the line detected is $H\alpha$.

Determining the line equivalent width of candidate objects allows us to estimate a galaxy's r' magnitude based off the continuum without any emission line. Such a magnitude may be useful in more precisely defining the surveyed population, and help in planning follow up observations of these objects. To do this, note that the total counts detected through any of the three $H\alpha$ filters can be given by Eqn. 2.1. We can then rearrange to solve for the continuum contribution to get the relationship

$$C = \frac{Counts}{EW_{line} * T + EW_{filter}}.$$

(2.3)

The counts above can be translated into an r$'$ magnitude using tabulated magnitude values from calibrated stars within the field of view.

2.3 Expected Numbers

While we are interested only in $H\alpha$ emission, there are three other prominent emission lines, [OIII]$\lambda 5007, \lambda 4959$ Å, (hereafter [OIII]) and [OII]$\lambda 3727$ Å, (hereafter [OII]) which will fall within the filter bandpasses for background objects at specific redshifts. $H\alpha$ emission is captured within the redshift range of $0.003 < z < 0.031$ as discussed previously. [OIII] is captured from $0.31 < z < 0.35$. These objects are at a distance of 1308 Mpc or, 4.27 billion light years. [OII] is captured from $0.77 < z < 0.82$ which is a distance of 2793 Mpc or 9.112 billion light years away. Significantly more objects will be included from these unwanted lines than from $H\alpha$, since those objects are from much larger volumes. For these most distant objects the light has been traveling for 6.8 billion

years. The light from these objects is older than our solar system. This does suggest that our method may help to determine the LSS at much greater distances than a z of 0.31. In our analysis of these emission lines we ignore the [OIII]λ4959 Å line, which always accompanies the [OIII]λ5007 Å line and is detected at essentially its same range. Its bluer emission will cause our estimate of the λ5007 Å line to be infered as being slightly bluer that it really is by 12 Å.

To estimate the number of objects with unwanted emission we take the galaxy luminosity distribution to be a Press-Schechter function (Press & Schechter 1974) given as,

$$M = 0.4 * ln(10) * \Phi_* \int_{M1}^{M2} [10^{0.4*(M_*-M)}]^{\alpha+1} * exp[-10^{0.4*(M_*-M)}]dM. \tag{2.4}$$

The values we used are, $M_* = -19.74$, $\Phi_* = 0.19x10^{[}-2]h^3Mpc^{[}-3]$, and $\alpha = -1.18$ taken from Hoyle et al. (2005). The expected $m_{r'}$ magnitude limit for a 30-minute exposure using the Mayall 4m+Mosaic 1.1 imager and redshifted $H\alpha$ filters is approximately 23. This sets different faint magnitude limits at each of these volumes. For the faint magnitude cut off we chose to use the luminosity distance to each object because the expansion of space will cause the objects to appear farther. For the volume where $H\alpha$ is detected this will give a faint magnitude limit of -12.6. For the distance where [OIII] is detected the limit will be -18.35, and for the distance for [OII] it will be -20.58. We assume this to be the limit when setting the low-luminosity cutoff for the Press-Schechter function through each volume.

Since detection is a function of line strength, we also must know the percentage of galaxies with $H\alpha$, [OIII], and [OII] emission as a function of equivalent width. Gregory et al. (2000) measured 350 galaxies in the Arizona-New Mexico Spectroscopic Survey of Galaxies (ANM) of the Perseus supercluster specifically to get spectral emission and absorption characteristics for a complete sample of galaxies away from rich clusters. Their results for the percentage of galaxies having equivalent widths greater than 10, 20, 50, and 100 Å are given in Table 2.2. Nakamura et al. (2004), using data from the SDSS DR1, published line strength data on $H\alpha$ in their Fig 1. These data, translated from their graph by us, are also listed in Table 2.2 and agree reasonably well with

Table 2.2 The assumed fraction of galaxies with emission line equivalent widths of $H\alpha$, [OIII], and [OII] and the values for the power law used to model the percentage of galaxies with the given emission line. The first column of Table 2.2 is the emission line observed. Columns 2, 3, 4 and 5 are the fraction of all galaxies with an equivalent width greater than the header value. Columns 6 and 7 are the a and b values used in the estimation formula $y = ax^b$, where y is the fraction of galaxies, and x is the equivalent width of the emission line.

Emission Line	10 Å	20 Å	50 Å	100 Å	a	b
$H\alpha$ (ANM)	0.24	0.097	0.009	0.003	27.93	-1.99
$H\alpha$ (Nakamura)	0.22	0.12	0.028	0.004	15.62	-1.72
$[OIII]$	0.083	0.037	0.006	0.003	2.88	-1.52
$[OII]$	0.33	0.15	0.029	0.006	22.65	-1.75

the ANM results, although their number of galaxies with $EW > 50$ Å is about three times more numerous. From these data, averaged in the case of $H\alpha$, we modeled the number of galaxies as a function of $H\alpha$, [OIII], and [OII] emission line strength using a simple power law. The power law takes the form $y = ax^b$, where y is the fraction of galaxies, and x is the equivalent width of the emission line. In Table 2.2 the first column gives the emission line. The fractions of galaxies with emission greater than this value are given in columns 2-5, and the values for a and b are shown for each of the three emission lines in columns 6 and 7.

Using the power law values of Table 2.2 we calculated the percentage of galaxies which will fall in each of the distance ranges sampled by our filters. We found that in a given frame, for a uniform distribution of galaxies, we can expect $H\alpha$ to be between 2.2 - 3.2%, [OIII] to be about 46%, and [OII] to be about 51% of the candidates observed.

These values erroneously assume that the percentage of galaxies having emission is constant with respect to absolute magnitude. Exactly how the emission percentage varies with absolute

magnitude is not abundantly clear, but the variance with respect to any of the three emission lines should be similar. Because we are essentially considering the ratio of galaxies with $H\alpha$ emission to the other two types, the variance will cancel out for the brighter part of the luminosity function that is mutually sampled in all volumes.

There is significant evidence that less-luminous galaxies have a greater percentage of emission than more luminous ones (Nakamura et al. 2004). Since the $H\alpha$-detected galaxies are closer than those detected by emission in [OIII] and [OII], an increase in their population percentage at fainter magnitudes will elevate the expected detection percentage. On the other hand, it is presumed that emission within a galaxy should diminish with time. This suggests that galaxies at earlier times, and therefore greater distances from us should show a greater amount of emission than nearby galaxies. This evolutionary effect works opposite to the trend of low luminosity galaxies having a greater percentage of emission, and will decrease the expected percentage of galaxies with $H\alpha$ emission. This effect will likely not be as strong as the above trend, meaning we are underestimating the fraction of galaxies with emission. Even so, for our purposes here we will assume that $\approx 3\%$ of the sample should have $H\alpha$ emission.

2.4   Broadband Observations

The high sensitivity to unwanted emission makes it necessary to identify and separate out as many galaxies which are detected from their [OII] and [OIII] emission as possible. Fortunately, each of these emission lines are from galaxies with a significantly different amount of redshift, and the difference in their average Sloan broadband g'-r' and r'-i' colors should be large.

To investigate the differences between these galaxies, we first took a model spectrum for a galaxy with strong emission from the SDSS DR7 (Abazajian et al. 2009), and artificially redshifted the spectrum so that the $H\alpha$ emission line would fall within the band passes of the three $H\alpha$ filters.
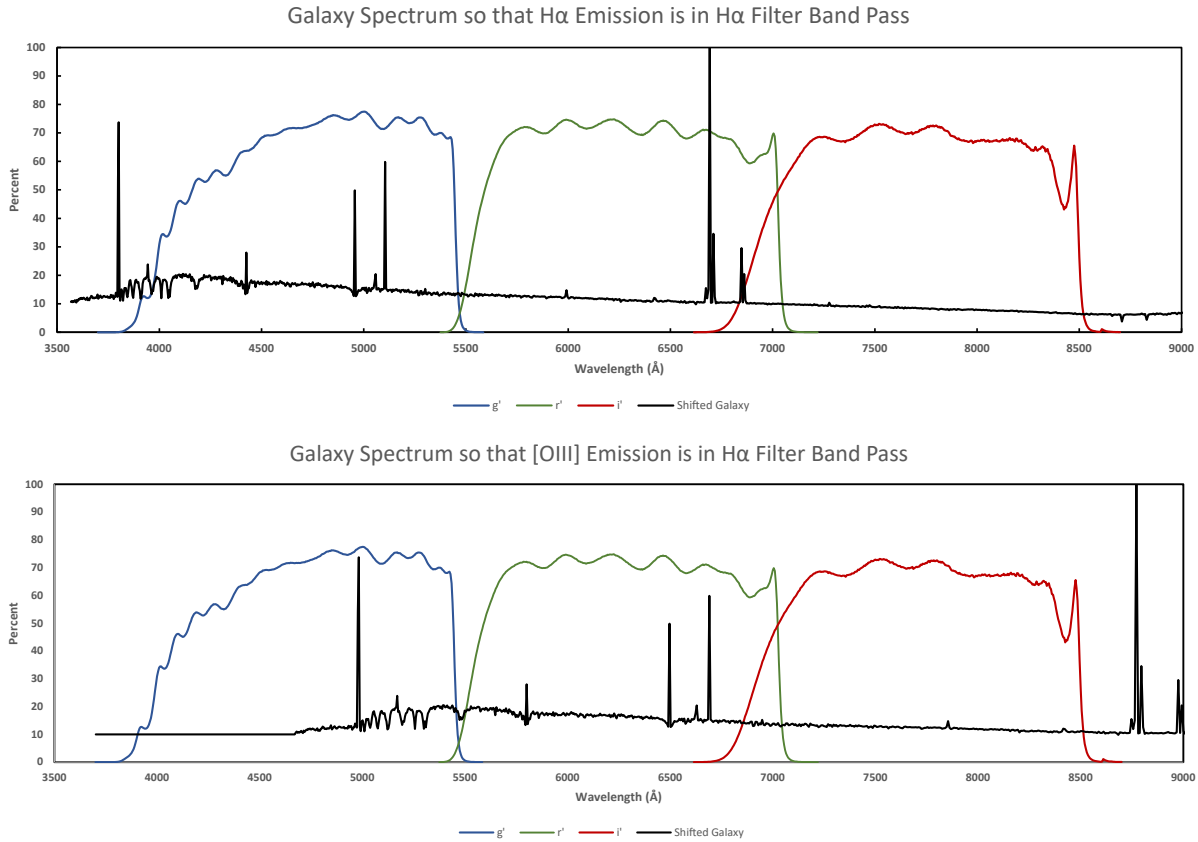
Figure 2.4 Comparison of the same emission galaxy spectrum, but shifted so that the $H\alpha$ emission line falls within the band passes of the three $H\alpha$ filters on top, and so that the [OIII] emission line falls within the three $H\alpha$ filter band passes on the bottom. Also shown are the filter band passes for the Sloan g', r', or i' filters. Due to the overall shape of the spectrum there is a significant change in the amount of light through each of the g', r', or i' filters. This indicates that it should be possible to begin separating which emission feature is detected using the three $H\alpha$ filters, based on the color-color, g'-r' vs r'-i' relation.

Then taking the profile of the Sloan g', r' and i' filters from KPNO, and the response of the Mosaic 1.1 CCD, we modeled an expected color difference, g'- r' and r'-i'. We then did the same for both the [OIII] and the [OII] lines, and found that there is a significant change in the color relation with the spectrum appropriately redshifted. See Figure 2.4 for a comparison of the spectrum through the g', r' and i' filters.

To further investigate this difference, we used galaxies from SDSS DR7 to quantify the color

differences between the three emission types. We queried the entire database for galaxies with emission and having magnitude errors no greater than 0.2 in either g', r', or i'. Of these we found 700 objects with $H\alpha$ emission at the correct distance for $H\alpha$ emission to fall within the band passes, and the same number for [OIII] and [OII] emission. The choice of 700 objects for each type of emission was determined by the number of objects with [OII] emission since these distant objects were least common.

Taking the Petrosian g', r' and i' magnitudes from SDSS, we formed the color-color relation, $g'-r'$, $r'-i'$, presented in Figure 2.5. In this figure each emission type is shown in a different color. The size of each galaxy's symbol is proportional to the strength of its equivalent width with the scale normalized to give each emission-line group the same range in sizes.

There are clear clusters of the different types of objects when the emission is weak. The $H\alpha$ objects cluster at an $r'-i'$ near 0.0 and a $g'-r'$ of 0.3. The [OII] objects are redder than this in $r'-i'$ while the [OIII] objects are redder in $g'-r'$.

As the emission of the $H\alpha$ objects strengthens, both of the color values become bluer, pushing the trend mainly toward the left but also down. The [OIII] objects follow a similar trend with strengthening emission at first, but then begin shifting to the right and down. This reddening in $g'-r'$ is because [OII] emission is in the g' band and is weakening as [OIII] emission strengthens. The [OII] objects, like the $H\alpha$ objects, tend to move down and to the left and unfortunately intrude into the $H\alpha$ weak-line cluster.

Since we are interested in finding objects with $H\alpha$, we determined the bivariate normal contour of this population and plot the 1σ and 2σ contours on Fig. 2.5. Considering the 2σ contour, we then determined how many of the [OIII] and [OII] objects fall within that range. Of the 827 objects within it, $H\alpha$ makes up 78.4%, [OIII] 2.4%, and [OII] 19.2%.

From this, we can expect that if a void had a distribution following the Press-Schecter function, 19.2% of the emission objects with colors in the 2σ contour will have $H\alpha$ emission, 7.4% will
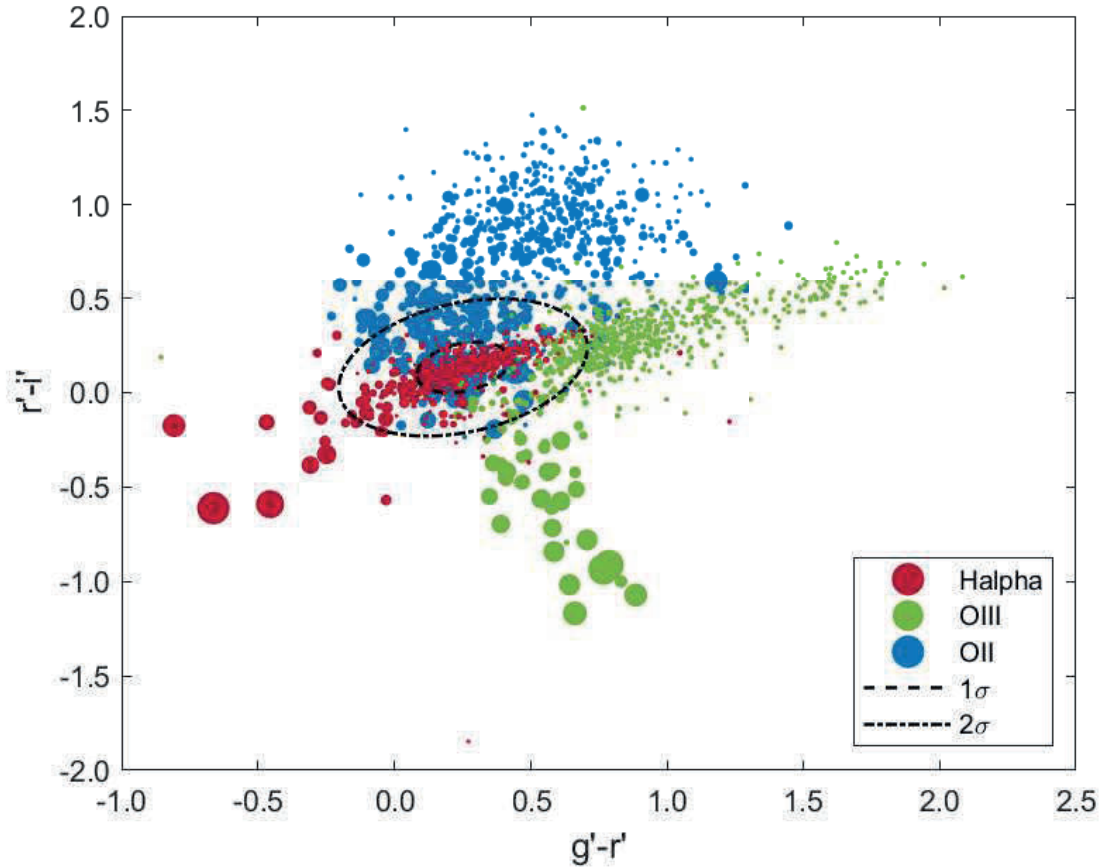
Figure 2.5 A color-color plot of g'-r' vs r'-i' for galaxies with emission of the correct emission lines at the correct distances to be picked up by the three intermediate band $H\alpha$ filters. There is a clear separation between the objects with $H\alpha$ emission and [OIII] emission. There is some overlap between $H\alpha$ and [OII], but there is still enough difference to allow us to reduce the number of false positives from looking for objects with emission from the $H\alpha$ filters. The black dashed oval shows the region containing 2σ of the objects with $H\alpha$ emission. The smaller dash dot oval shows a region of 1 sigma inclusion of those with $H\alpha$ emission. The population in the two sigma region contains 78.4% $H\alpha$, 2.4% [OIII], and 19.2% [OII]. The 1σ region contains 91.9% $H\alpha$, 0.2% [OIII], and 7.9% [OII]. Using the narrower region will give us a clear advantage in separating which type of emission feature is detected, but will also reduce many of the likely candidates. Note the region in the lower left which only contains objects with $H\alpha$ emission. Any objects found in this region are the best candidates to fall within the void.

have [OIII], and 73.4% will have [OII]. Considering this and assuming a binomial distribution, we can determine the density of the void based on the number of objects found within the void. For example, if we take 22 spectral observations of objects within the 2σ range and none of these are found to be $H\alpha$, the void has a maximum density of 1% of the mean. With 33 observations and none of these found in the void, the density is 0.1% of the mean.

The smaller 1σ oval for $H\alpha$ includes 481 total objects. This smaller distribution has 91.9% as $H\alpha$, 0.2% [OIII], and 7.9% [OII]. From these we can expect that 40.0% of emission objects should be $H\alpha$, 1.3% should be [OIII], and 58.6% should be [OII]. Using a binomial distribution, this suggests that with 9 spectral observations with none being objects at the correct distance for the $H\alpha$ emission to be in the $H\alpha$ filters, the mean density of the void is 1%, and with 14 spectral observations the density is 0.1%. Though the smaller 1σ relation gives better statistics, it does mean a reduction in the total number of candidate objects.

Of particular interest in Fig. 2.5 is the scattering of $H\alpha$ objects to the lower left of the ellipses. These are objects with very strong $H\alpha$ emission and occupy a region on the graph that is completely devoid of objects with O[III] and [OII] emission. Objects in this area are prime candidates to be at the right distance to place them within the void.

As will be discussed later in Chapter 4, we were given time on the Gemini 8 meter telescope to begin taking spectra of candidate objects. At the time we had not yet finished the color-color and broadband filter analysis. In total we were able to get spectra on 6 objects. After analyzing the broadband color-color we were able to confirm that this approach is able to guide which type of emission line is being detected. Of the 6 objects for which the spectrum was taken, FN8-74-20192, FN8-74-19127, and FN8-74-4837 all fall within the 2σ, so it is not clear from the region if the detected emission line is $H\alpha$ or [OII]. From the spectrum all of these have [OII] emission captured in the intermediate filters. As discussed previously in this region it is most likely that the objects in the 2σ region are most likely [OII]. Two of the objects for which we have spectra, FN8-74-6095

and FN8-74-9573, fall in the region where [OIII] only emission occurs and both objects did have the [OIII] emission captured. The last object, FN8-74-12858 has its broadband color-color values in the region of objects with [OII] emission only, and the spectrum does show that the [OII] emission line is what was captured.

Chapter 3

Photometric Observations and Analysis

3.1 Observations, Data Reduction, and Analysis

In 13-17 of February 2013 we used the KPNO Mayall 4 meter telescope and MOSAIC 1.1 imager to image through the center of the voids we designate as FN8 and FN2 as described in chapter 2. We chose these voids for being reasonably large, well-defined, having been cataloged by Hoyle & Vogeley (2002) as well as by Foster & Nelson (2009), far enough north to be readily accessible, and at an ideal distance and diameter for the $H\alpha$ filters. We imaged 12 36 arcmin $\times$ 36 arcmin fields centered at RA = 12h 40m, DEC = +70 deg 40 arcmin in FN8 (see Figure 3.1) and five 36 arcmin $\times$ 36 arcmin fields centered at RA = 3h 42m, DEC = +17 deg 20 arcmin (see Figure 3.2). Each field was imaged with a dithered exposure of 5 minutes for 5 intervals, for a total of 25 min. each. A dither is when the image is shifted by a small amount in between images. This is needed to fill in the gaps between the 8 CCDs that make up the Mosaic 1.1 imager. The total exposure times are sufficient to obtain an integrated S/N $\approx$ 10 for objects with $M_{r'} = -12.0$ at the void center of 4980 km·sec^{-1} (z=0.017). We then took Sloan g', r', and i' broadband images with an exposure of 5x150 seconds each to allow for color-color determinations.
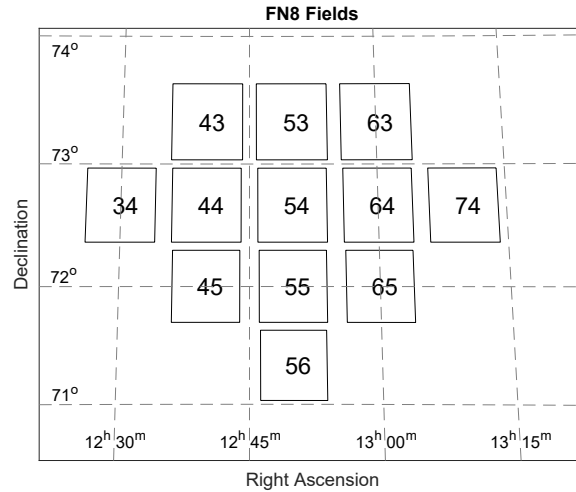
Figure 3.1 Finder chart for each of the 12 fields imaged during Feb. 13-17 2013, in the void FN8. Each field was imaged with a dithered exposure for 5 min. each for 5 intervals for a total exposure of 25 min.
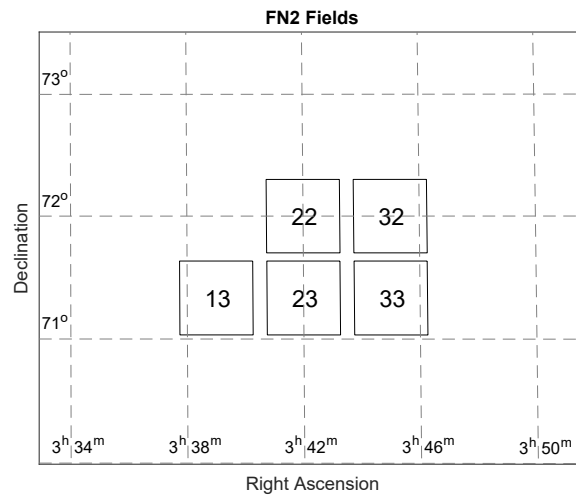
Figure 3.2 Finder chart for each of the 5 fields imaged during Feb. 13-17 2013, in the void FN2. Each field was imaged with a dithered exposure for 5 min. each for 5 intervals for a total exposure of 25 min.

The images were processed using the KPNO pipeline (Valdez & Tody 1998). Modern imaging relies on the charged-couple device (CCD). This piece of equipment images by generating electron counts when a pixel is struck by a photon. Though these devices have had a great impact in allowing faster and fainter images to be taken, it is necessary to clean up the images. During the imaging, and readout processes errors distort the data. To reduce these effects it is necessary to process the data images with three types of calibration images, zeros (or bias), darks and flats. The zero image is produced simply by turning on the CCD, then immediately reading out the data. This is done to see how electrons will get stored in the pixels of the CCD simply by turning it on. Usually many zero images are taken and averaged together to make a single master zero image that is then subtracted from the data image.

The dark image is taken while the CCD is still in the dark with no light hitting it. This is usually accomplished by keeping the shutter of the camera closed. The dark has an exposure length for the same amount of time as the data image. The dark is taken to account for any electron drift that will occur as the CCD is recording the data. As with the zero image, many dark images are taken and then averaged to make a master dark image, which is then subtracted from the data image.

The last type of calibration image is the flat image. This is taken while the CCD is exposed to a region that is uniformly lit by light. This can either be a region of the sky during sunset, or a large flat screen inside the telescopes dome with very careful lighting. The flat is taken to test the pixels response to light. Some pixels may be more sensitive and others less sensitive. This can lead to spots that are either too bright or too faint on the data image. Again, we take many flat images and average them to form a master flat from the data image. After doing all of this, the data image will have reduced errors from how the CCD responds.

The Mosaic 1.1 imager is actually made of 8 separate CCDs, which causes lines between the CCDs where no light is recorded (see right image of Figure 3.3). To correct for these regions we dithered the image, taking 5 images slightly off from one another. The KPNO image reduction

Figure 3.3 An image of field FN8-74, which has been processed using zero, dark, and flat images, but which has not been corrected by overlaying the dithered images to remove the missing regions between the 8 CCDs.

pipeline then used these images to make a composite image which has much of the missing data replaced (see left image of Figure 3.3). Though this did fill in the gaps through the center of the image, there remain regions around the edges of which are missing data, or have reduced net exposure times.

After receiving the processed images, identification of emission line objects followed two paths. The first was a by-eye search using subtracted images $H\alpha12 - H\alpha8$ and $H\alpha12 - H\alpha16$. Doing this, any object with only continuum emission passing through the filters would be subtracted out, but any object with strong emission of the right wavelengths would appear bright (see Figure 3.4). We decided to take this path as a quick check to see if there were objects with emission lines falling within the filter set, and as a way to keep objects where a strong emission line may also be on top of a bright continuum. The bright continuum would cause some objects with detectable emission to be removed in the other identification process for not having a strong enough emission line.

The second method to identify candidate objects was to sum the $H\alpha8$, $H\alpha12$, and $H\alpha16$ frames
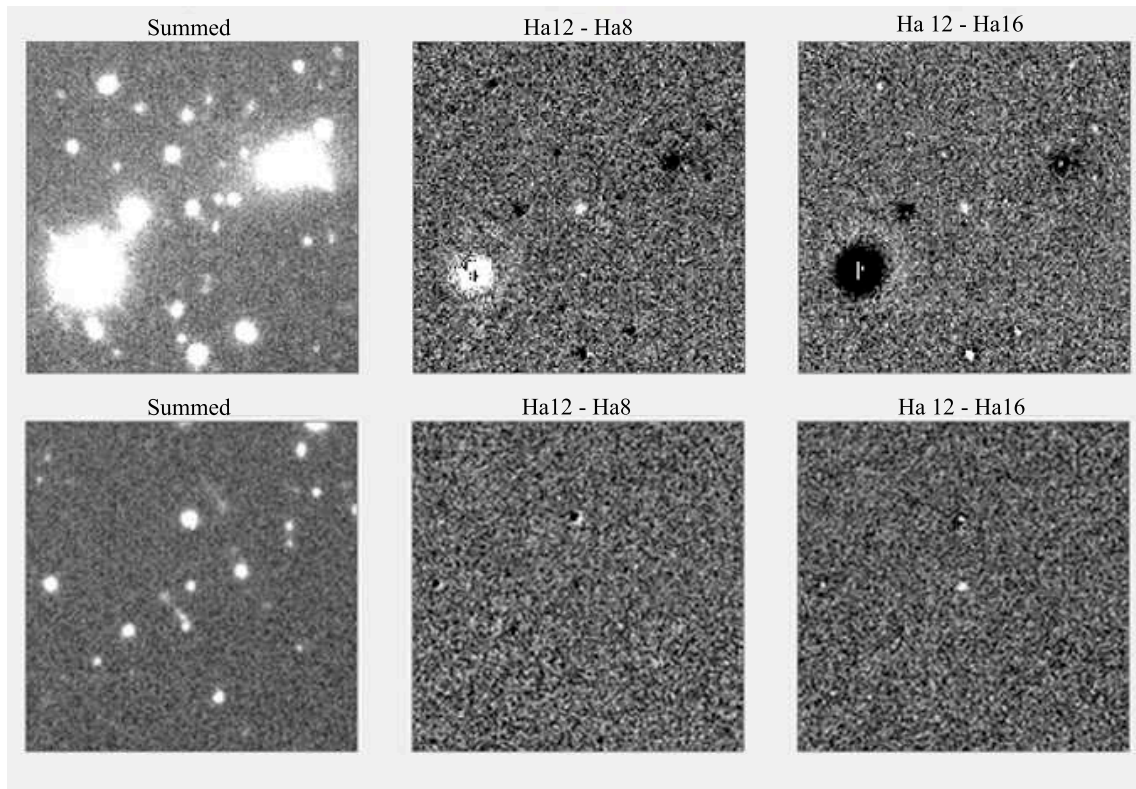
Figure 3.4 Two examples of how subtracting the $H\alpha 8$ and $H\alpha 16$ images from the $H\alpha 12$ image will cause objects with emission lines to stand out compared to objects with no emission lines. In each case the left image is the sum of all three frames, $H\alpha 8$, $H\alpha 12$, and $H\alpha 16$ which will help enhance faint objects. The middle image is $H\alpha 12 - H\alpha 8$. The right image is $H\alpha 16 - H\alpha 12$. In the top row the object clearly stands out in both the middle and the right frames. This shows that there is an emission line which falls among the filters at the correct position so that the transmission of the emission line is brighter through the $H\alpha 12$ filter than either of the other two. In the bottom row, the object disappears in the middle frame, but appears bright in the right frame. This shows that the emission line falls so that the transmission is nearly equivalent in the $H\alpha 8$ and $H\alpha 12$ filters, but is much weaker in the $H\alpha 16$ filter. In both instances this shows that there is a detectable emission line falling within the filter band passes.

of each field together, to increase survey depth. On this summed frame we used SourceExtractor (Bertin & Arnouts 1996) to compile a list of object positions. SourceExtractor identified on the order of 20,000 objects per field. Using this catalog of objects we then determined the counts for the identified objects from each of the individual $H\alpha$ images again using SourceExtractor.

We next determined the magnitude offset of each of the $H\alpha$ images in each field. To compare fields it was essential to place the photometry on a system that is consistent across all fields and filters, compensating for variations in seeing and weather. Each frame was tied to the USNOB catalog r' magnitude as part of the KPNO data reduction procedure. However, Valdez & Tody (1998) state that this calibration is only accurate to 0.5 mag. To improve on this we considered the 5,000 brightest objects on each image. Ignoring the brightest 1,000, to exclude any objects which were saturated, we found the average magnitude of the next brightest 4,000 objects. We then scaled the object counts from each filter in each field so that the average was the same as that for field FN8-74 in the $H\alpha$12 filter. A sample of these adjustments is in Table 3.1. Taking these values, we multiplied the counts determined by SourceExtractor for each field and filter to make sure they were consistent.

SourceExtractor flags objects when the algorithm may give an incorrect magnitude. We rejected all objects that were flagged except those which were flagged for having overlapping isophotal rings (flags 1, 2 and 4) suggesting overlapping objects. We then rejected all objects that were within 150 pixels of an edge because these did not have the full integration time due to dithering (see right image of Figure 3.3). We also rejected all objects with an error larger than 0.2 mag within any of the $H\alpha$ filters so that the remaining objects had a greater chance of being detected. We also rejected any objects with less than 500 total counts in all three of the $H\alpha$ filters. Any object with less than 500 counts will have a signal to noise of less than 5 making the uncertainties too large.

We next divided the photon counts from SourceExtractor in the three redshifted $H\alpha$ filters to form the ratios $H\alpha12/H\alpha8$ and $H\alpha12/H\alpha16$ as discussed in Chapter 2. These ratios were

Table 3.1 The count offset for each field and each filter used to make certain the photometry was well calibrated between the frames. The farther the number is from 1 the greater the adjustment needed to match the $H\alpha12$ filter of field FN8-74.

Field	$H\alpha8$	$H\alpha12$	$H\alpha16$
FN8-74	0.97	1.00	1.03
FN8-65	1.06	1.11	1.03
FN8-64	1.02	0.97	0.97
FN8-63	1.02	0.97	1.03
FN8-56	1.08	1.08	0.93
FN8-54	0.89	0.95	0.95
FN8-53	1.28	1.19	1.17
FN8-45	1.12	1.21	1.13
FN8-43	1.25	1.13	1.06
FN8-34	0.90	0.93	0.93
FN2-13	1.42	1.45	1.45
FN2-22	1.78	2.16	2.52
FN2-23	2.09	1.92	1.78
FN2-32	0.14	0.05	0.05
FN8-33	3.73	2.80	2.87

chosen because a galaxy with $H\alpha$ emission at the center of the void would have a value greater than one in both ratios, while objects without emission and nearly flat continuum have values near one. We rejected any object with both ratios less than one, as our analysis shows that no object within the void would have these values. Any object which was identified based on the ratios to have an emission line with an equivalent width greater than 100,000 was also removed for being nonphysical. Fig. 3.5 shows a plot of $H\alpha12/H\alpha8$ vs $H\alpha12/H\alpha16$ for FN8-74. Objects without emission form a bivariate normal distribution centered on one in each axis. The width and height of the distribution is caused by slight differences in the slope of the continuum in the filters, as well as differences in seeing which remained even after adjusting the images as mentioned above. We then rejected all objects within 2σ of this center as most probably being non-emitters or having weak emission. Some objects with weak emission are detectable by eye if their overall magnitudes are bright. These are the objects included in the initial by-eye pass. These form a separate population than the continuum objects and are included in the list of candidate objects.

The final cut was done by eye to make sure that no bad pixel or cosmic ray strikes were included. This was done using the software *Compare Images* developed by Dr. J. Moody. This software displays the data from a co-registered 50×50 pixel section of each field. The section to be displayed is read in from a text file or may be entered by hand. Data from each of the individual redshifted $H\alpha$ filters is displayed together with a summed frame, each of the $H\alpha$ filters, and the difference frames of $H\alpha12 - H\alpha8$ and $H\alpha12 - H\alpha16$. (See Figure 3.6.) An object with strong emission in $H\alpha12$, corresponding with the center of the void, would appear bright in both frames. Using the software we checked all candidate objects by eye to remove any false detection, particularly from cosmic ray strikes.

To separate which emission line is being detected, $H\alpha$, [OIII], or [OII], we formed a color-color relation of the Sloan broadband filters, $g' - r'$, and $r' - i'$, as described in chapter 2. Fig. 3.7 shows the distribution of the candidate emission objects in color-color space. Note the general agreement
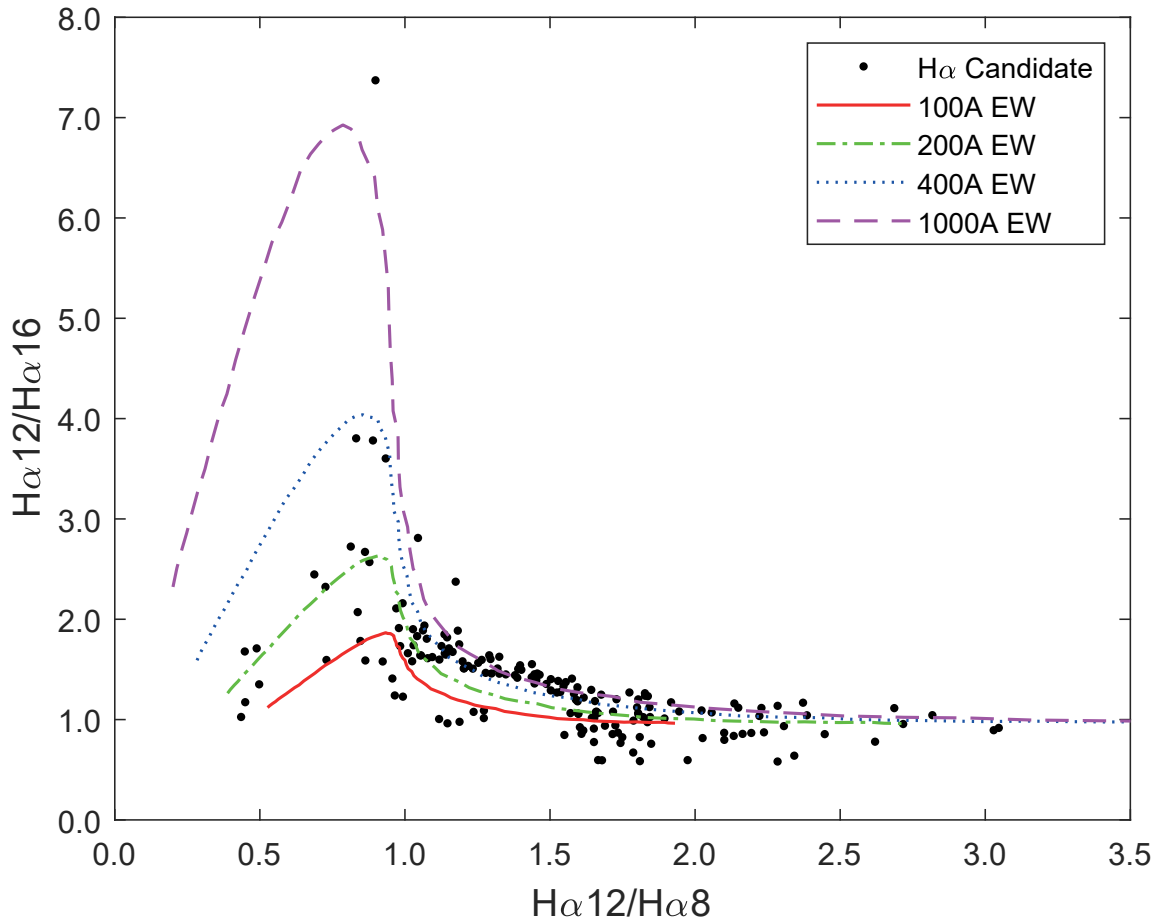
Figure 3.5 A plot showing all candidate objects found for the field FN8-74. The horizontal axis is $H\alpha12/H\alpha8$ and the vertical axis is $H\alpha12/H\alpha16$. Each black dot is an emission-line object. The curves show the traces of varying equivalent widths from Fig 2.3.
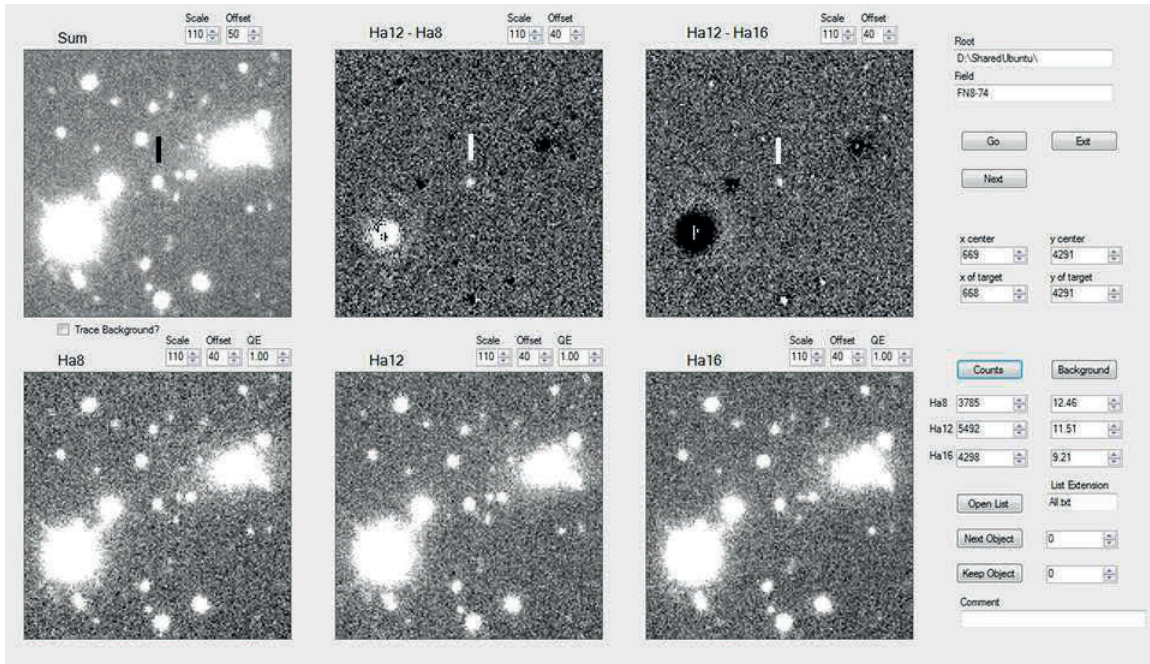
Figure 3.6 A screen shot of the software Compare Images developed by us for this project. The images across the top are the summed data from the $H\alpha 8$, $H\alpha 12$, and $H\alpha 16$ filters (left), the difference frame of $H\alpha 12 - H\alpha 8$ (center) and the difference frame of $H\alpha 12 - H\alpha 16$ (right). The images across the bottom are the $H\alpha 8$ image (left), the $H\alpha 12$ image (center), and the $H\alpha 16$ image (right). The object shown has significant emission in the center of filter $H\alpha 12$, making it appear white in both the $H\alpha 12 - H\alpha 8$ and $H\alpha 12 - H\alpha 16$ images. The strength of the image in two difference frames gives a visual estimate of the emission-line placement: An object whose image is brighter in $H\alpha 12 - H\alpha 8$ is at a greater redshift while an object whose image is brighter in $H\alpha 12 - H\alpha 16$ is at closer redshift.
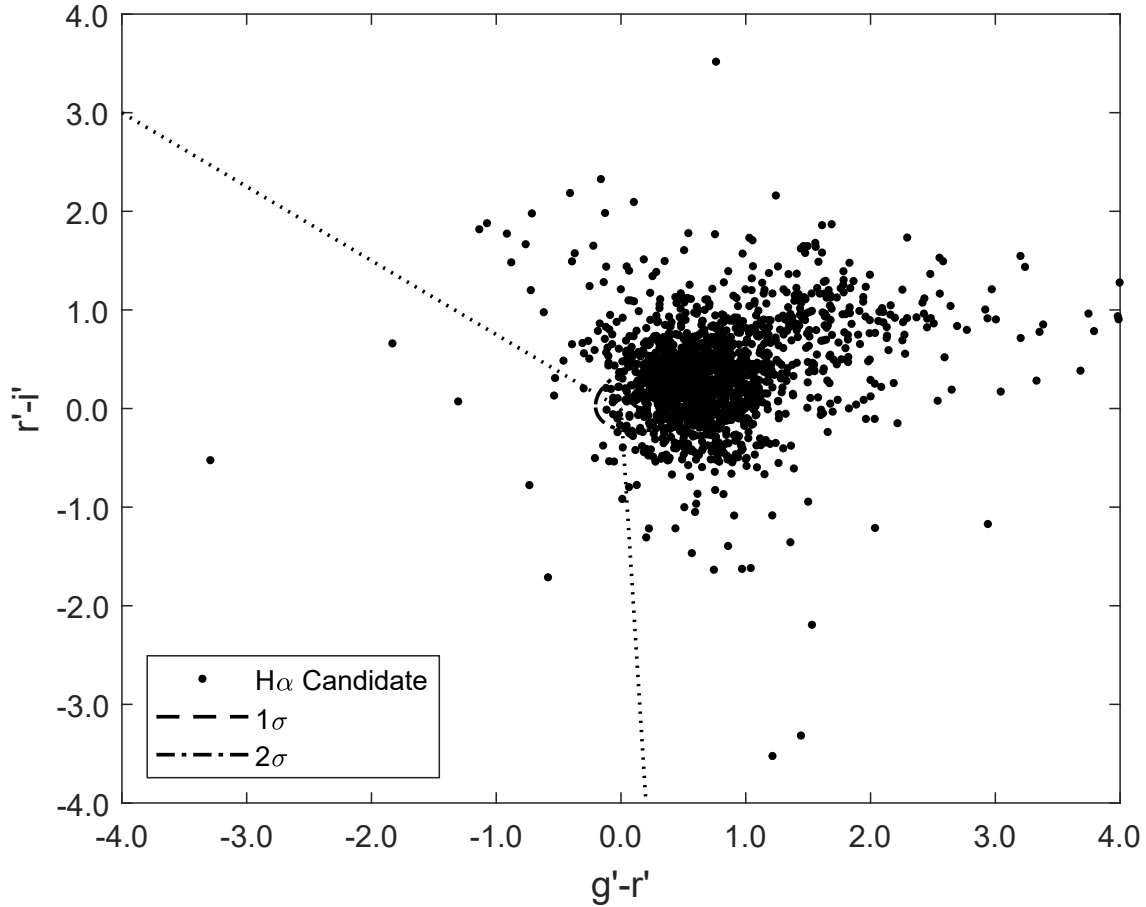
Figure 3.7 A color-color ($g' - r'$ vs. $r' - i'$) plot of all the $H\alpha$ emission line candidates from our survey. The region in the left corresponds to objects which likely have $H\alpha$ emission without contamination from [OII] or [OIII].

of the distribution of objects with what was found in chapter 2.

Using the theoretical curves and look-up tables discussed in chapter 2, we have determined the redshifts and equivalent width for all of these objects.

3.2 Discussion

Altogether we identified 2374 objects with strong emission, with 23 objects falling within the $H\alpha$ emission line region of the color-color relation as defined in chapter 2. There are 75 objects which

Table 3.2 A sample table for the emission line candidate objects found in the survey consisting of the first 6 lines of the table in Appendix D. The columns are the Field designation, ID, RA, Dec, r' magnitude, equivalent width and cz of the objects. Entries left blank are not listed because they fall within a region of large error on the look-up table discussed in chapter 2. This table only includes the objects which fall in the $H\alpha$ only region. The full tables are found at the end, Appendix D, Appendix E, and Appendix F.

Field	ID	RA	Dec	r'	EW (Å)	cz (km·s^{-1})
FN8-74	12783	13:13:28.446	72°43'01.906"	23.3	195	4300
FN8-74	20280	13:13:32.278	72°57'52.557"	22.4		
FN8-74	13993	13:11:11.503	72°45'8.622"	23.0	210	4200
FN8-63	12974	13:3:29.223	73°24'59.824"	26.2		3800
FN8-63	10903	13:3:19.059	73°19'55.135"	27.0		4200
FN8-63	3857	12:59:57.453	73°05'4.278"	27.3		

fall within the 1σ region, and 452 which are within the 2σ (including all objects which fall within the 1σ region). Of particular interest are 7 objects which fall within both the $H\alpha$ and 2σ regions. Table 3.2 provides a sample catalogue for all of these objects, including the Field designation, ID, RA, Dec, r' magnitude, the equivalent width of the emission line, and finally the distance to the object measured in cz, assuming that the emission is $H\alpha$ and not either [OII] or [OIII].

With the assumption that all 23 objects within the $H\alpha$ region do fall within the void, they compose 0.96% of the total population. The analysis of chapter 2 predicts that a normal distribution of objects through the void should come up with 3.2% of objects being $H\alpha$ emission objects. This suggests that, if all 23 objects are $H\alpha$ emission objects, the void has a density of no more than 30% of the cosmic mean. All of these objects have magnitude errors large enough that any of them may actually fall outside of the $H\alpha$ region. This demonstrates the need to obtain spectra on these objects, and to begin to take spectra on the objects which fall within the 1σ region to have a better

understanding of the true void density population.

Chapter 4

First Spectra

4.1 Observation and Analysis

As we were still in the process of modeling and refining our analyzing technique and processing the data from the redshifted $H\alpha$ survey we were able to begin taking spectra of our candidate $H\alpha$ objects using the Gemini 8 m telescope. Unfortunately, because of the scheduling of the time allocated for these spectra, we had not yet completed our color-color and broadband analysis identifying the $H\alpha$ emission objects. We therefore chose objects by eye. For these first spectra we wanted to sample a range in emission-line strength to better understand the sensitivity of the selection criteria. Therefore, some objects were purposely chosen for a strong signal and others for their weaker emission. We did not sample at the very edge of detection because, with time to observe only a few objects, we wanted to be reasonably certain that those we examined did in fact have emission.

Finally, we decided to choose objects from the same field, #74 in our grid of void FN8 (see Figure 3.1). Seeing and weather varied from field to field, and we felt we could get a better understanding of the survey selection function by limiting our sample to objects imaged under the

same conditions. Fourteen objects were chosen for possible observing. All of these were chosen by-eye using the subtracted images $H\alpha12$-$H\alpha8$ and $H\alpha12$-$H\alpha16$, searching for objects which stood out in one or both of these images. Time was obtained to observe six of these: FN8-74-20192, FN8-74-19127, FN8-74-6095, FN8-74-4837, FN8-74-12858, and FN8-74-9573. For FN8-74-1 the slit was placed to also observe a weak candidate just south of it, called FN8-74-20192b.

The spectral data were taken 2016 January 1, 20, and 21 with the Gillett Gemini telescope and GMOS spectrometer as part of program GN-2015B-FT-15. Spectra of all but FN8-74-20192b are shown in Figure 4.1. In four of the spectra only one line, the [OII]$\lambda3727$ doublet, is visible. In the other two spectra, the [OIII]$\lambda4959$, 5007 and Hβ lines are visible. Since none of these emission lines was Hα, none of the candidate objects were within the void.

The distinctive pattern of the [OIII]$\lambda4959$, 5007 and Hβ lines made their identification trivial. Identifying a single emission line in a low S/N spectrum is more challenging, but is not impossible (cf. Lilly et al. 1995). First, in a spectrum covering 2500 Å like ours, it is expected that several emission lines should be in the spectral window for any reasonable redshift range. Of the four objects with only one detected emission line, the spectrum for FN8-74-19127 has the highest S/N and a signal sufficient to detect any line with EW > 5 Å. Upon that basis it seemed unlikely that the emission-line was $H\alpha$, since the metallicity would have to be unprecedentedly low to not also have the [OIII], [OII], and/or [NII] lines visible. There are objects termed weak-oxygen red (WOR) by Lewis (The University of Michigan, 1983) that do have a strong $H\alpha$ line with all lines blueward strongly suppressed, presumably by reddening. These objects tend to have strong [NII] emission, which we do not see here.

The single line in all cases is clearly the [OII]$\lambda3727$ doublet. At the resolution of our spectra this doublet will be noticeably broader than either the [OIII]$\lambda4959,5007$ or Hβ lines. All of the single lines are that broad as illustrated by Fig. 4.2 for one of those lines. This figure shows the single-lined spectrum of FN8-74-19127 displayed at the same scale and contrast as the spectrum of FN8-74-
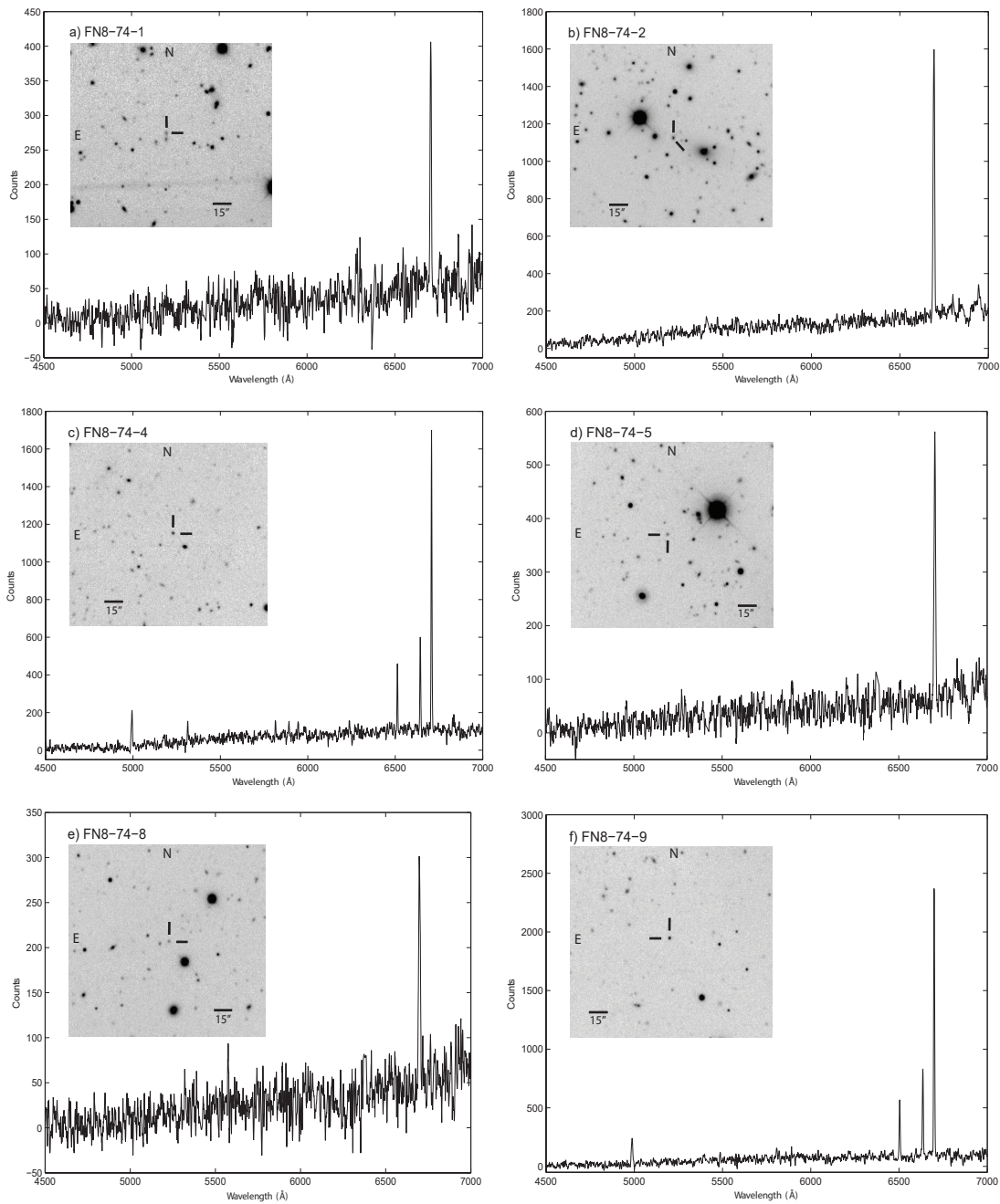
Figure 4.1 Finder charts and spectra for objects FN8-74-20192, FN8-74-19127, FN8-74-6095, FN8-74-4837, FN8-74-12858, and FN8-74-9573. All spectra have been boxcar smoothed with a five pixel window. Object FN8-74-20192b is visible just below object FN8-74-1.
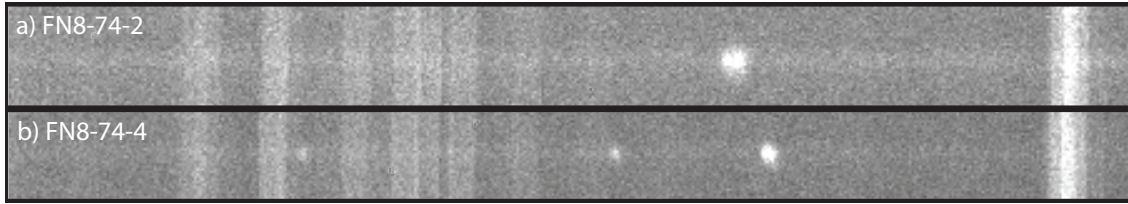
Figure 4.2 a) The spectrum of FN8-74-19127 from 6770 to 7228 Å, and b) the spectrum of FN8-74-6095 over the same wavelength range. Both spectra are wavelength calibrated and bias subtracted only and are displayed at the same base-level contrast. The line of FN8-74-19127 is the [OII]λ3727 doublet and is visibly broader with a hint of a double peak. All vertical stripes are night-sky emission lines.

6095 below it, which contains the [OIII]λ4959,5007 and $H\beta$ lines. The line of FN8-74-19127 is approximately 9 Å FWHM with a suggestion of a double peak. The lines of FN8-74-6095 all have FWHM of 4 or 5 Å. Deblending the FN8-74-19127 line using the *splot* routine in iraf separated it nicely into components peaking 5.0 Å apart, which is exactly the expected separation of the [OII]λ3727.092 Å and 3729.875 Å lines at that redshift. The ratio of [OII]λ3729.875/λ3727.092 of 1.2 corresponds to an electron density of approximately 10^2 electrons-cm^{-3}, which is reasonable for a galactic source. Based on this, it is apparent that we detected the [OII]λ3727 line. Line equivalent widths and magnitudes for all six objects plus FN8-74-20192b are given in Tables 4.1 and 4.2.

For fainter objects FN8-74-20192, FN8-74-4837, and FN8-74-12858, the results were essentially the same. Each has the same line width of about 9 Å found for FN8-74-19127. The separation of the deblended lines were 5.1 and 5.4 Å for FN8-74-20192, FN8-74-4837, respectively, and the λ3729.875/λ3727.092 ratios were 1.1 and 1.5. These values are highly uncertain and statistically no different from 1.0. The S/N was too low on object FN8-74-12858 to deblend the lines.

Object FN8-74-20192b was a weaker-signalled twin of FN8-74-20192. While the S/N was lowest of all the spectra, the line width was still measurable at 9 Å , which confirms it to be the [OII]λ3727 line.

As a further confirmation, FN8-74-19127, FN8-74-4837, and FN8-74-12858 have weak [NeIII]λ3869 lines barely visible above the noise. Being weak, they were identified by being both

Table 4.1 Observational Data 1: Locations and Magnitudes

Object ID	RA	DEC	m_R	M_R	z	σ_z
FN8-74-20192	13:13:27.065	72:57:41.56	21.5	-21.2	0.79812	0.00005
FN8-74-20192b	13:13:27.111	72:57:37.01	21.9	-20.8	0.79635	0.00029
FN8-74-19127	13:12:58.334	72:55:16.79	20.5	-22.2	0.79474	0.00004
FN8-74-6095	13:12:51.297	72:29:45.21	21.1	-19.7	0.33916	0.00004
FN8-74-4837	13:11:52.105	72:27:15.03	21.5	-21.1	0.79798	0.00006
FN8-74-12858	13:10:47.186	72:42:58.59	21.6	-21.1	0.79649	0.00002
FN8-74-9573	13:11:13.453	72:36:45.81	20.7	-20.1	0.33753	0.00005

Table 4.2 Observational Data 2: Emission-line Equivalent Width

Object ID	[OII]λ3727	[NeIII]λ3869	Hβ	[OIII]λ4959	[OIII]λ5007
FN8-74-20192	115	...	...	...	...
FN8-74-20192b	18	...	...	...	...
FN8-74-19127	77	7	...	...	...
FN8-74-6095	107	...	18	22	74
FN8-74-4837	83	3	...	...	...
FN8-74-12858	58	5	...	...	...
FN8-74-9573	123	...	56	49	136

the largest spike in that vicinity and by having the same redshift as the [OII]λ3727 line.

We note that redshifts were determined using the rest wavelengths for the [OII], $H\beta$, [OIII], and $H\alpha$ emission-lines in vacuum from SDSS (see http://classic.sdss.org/dr7/algorithms/linestable.html). These values were 3727.092 Å, 3729.875 Å, 4862.68 Å, 4960.295 Å, 5008.240 Å, and 6564.61 Å , respectively. When considering the [OII] doublet as a single line, we used an average value of 3728.48 Å. In converting from z to cz, we used a value of c = 299792.458 km·sec^{-1}.

4.2   Discussion

In chapter 2 we estimated both redshift and line equivalent width from the ratios of each object's photon count in the different intermediate-band filters, assuming the emission is Hα. We find the measured equivalent width of the total emission in the bandpass to be less than the estimated value by 10% with an rms scatter of $\sim$ 35%. This is an important point since a robust survey needs to accurately guide observers in establishing spectral observation times. The estimated line strengths from chapter 2 appear to be reliable.

Even though none of our objects had Hα in the bandpasses, our spectra can still be used to measure the accuracy of the redshift estimates from chapter 2. A "pseudo-redshift" can be formed that treats the [OII]λ3727 doublet for objects FN8-74-20192, FN8-74-20192b, FN8-74-19127, FN8-74-4837, and FN8-74-12858 and the [OIII]λ5007 emission line for FN8-74-6095 and 9 as being Hα. This assumption for FN8-74-6095 and FN8-74-9573 will cause their redshifts to be underestimated because the Hβ and [OIII]λ4959 lines blueward of [OIII]λ5007 will lower the redshift estimate. Even so, we find the value of (estimated redshift $-$ pseudo-redshift) to be -127 ± 204 km·sec^{-1}, a remarkably good agreement. When considering only the four objects with [OII]λ3727 emission, the agreement improves to -84 ± 186 km·sec^{-1}.

Six objects are not many, and it is wise not to infer too much about void populations from just

these. We do, however, note that if these objects had been at the center of the void, they would have M_R values in the range of -12.4 to -13.8. This is within the dwarf galaxy range pertinent to theory and confirms that if dwarf galaxies more luminous than an M_R of -12.4 are present in the void center, we should be able to detect them. Clearly, more followup redshift measurements are necessary to establish this as fact.

As mentioned previously in Chapter 2, the spectrum of these objects were able to be used to help confirm the use of the broadband color-color relation to begin separating which type of emission has been detected by the intermediate band filters. Objects FN8-74-20192, FN8-74-19127, and FN8-74-4837 fall in the 2σ regions where it is not clear if the object shows $H\alpha$ or [OII], though there is a greater probability that it is [OII]. As shown all of these do have [OII] emission captured. The objects FN8-74-6095, and FN8-74-9573 have broadband color-color placing them in the region where only [OIII] is located, and both objects have [OIII] captured. The last object FN8-74-12858, has a color-color value that places it in the [OII] emission only being captured, and that was in fact the case.

Chapter 5

Conclusion

I have presented a new photometric method for determining distances to emission galaxies, partic-
ularly galaxies with strong $H\alpha$, [OIII], and [OII] emission, though the method could be adapted
for any emission line and distance depending on the filters chosen. For our goals we use a set of
three intermediate-band $H\alpha$ filters which have been shifted by 8 nm, 12 nm, and 16 nm from the
standard $H\alpha$ filter, and the Sloan g$'$, r$'$, and i$'$ filters, we were then able to use a wide field survey
to identify emission line galaxies, determine their distances, and find the equivalent width of the
detected line. We have been particularly interested in how this method can be used to probe the
dwarf galaxy density through large, well-defined galaxy voids.

This method can improve the accuracy of photometric distance determination. This is particularly
evident if a better method is developed to determine which type of emission is being detected. Of
particular interest, this will allow a much faster determination of the large-scale-structure, with an
eye toward searching for dwarf galaxies in voids. From this, the density of objects in galaxy voids
can be determined depending on how tightly we use the color-color broadband comparison. If using
the 2σ region defined in chapter 2, we will be able to show the mean density of the void is no more
than 1% with as few as 22 spectra of the candidate objects. If using the more restricted 1σ region
we will be able to show the mean density is no more than 1% with as few as 9 spectra.

To apply the methods described in chapter 2, we performed a large field survey of the voids FN2 and FN8. This has yielded a total number of 2374 emission line galaxies. 23 of these fall in the $H\alpha$ region, 75 in the 1σ region, and 452 in the 2σ region. If all 23 $H\alpha$ candidate objects do fall within the void then the void has a galaxy density of 30% of the cosmic mean. However, all of these very faint objects have large enough magnitude errors to move them out of the $H\alpha$ only region. To positively identify if the emission line is $H\alpha$, and to confirm the equivalent width and the distance to the objects we must obtain follow-up spectra.

We were given time on the Gemini telescope to begin taking spectra of our objects. At the time we had not yet finished our analysis of the emission line objects, so we took a representative sample of objects only from the field 74. Though none of the 7 objects for which we obtained spectra were $H\alpha$, 2 being [OIII], the other 5 being [OII], we were able to estimate both redshift and line equivalent width from the ratios of each object's photon count in the different intermediate-band filters, treating the emission as Hα. We found the measured equivalent width of the total emission in the bandpass to be less than the estimated value by 10% with an rms scatter of $\sim 35\%$. This is an important point since a robust survey needs to accurately guide observers in establishing spectral observation times. The estimated line strengths from the method described in chapter 2 appear to be reliable.

Using the detected spectral lines of the objects observed we were able to determine a "pseudo-redshift" that treats the [OII]$\lambda 3727$ doublet and the [OIII]$\lambda 5007$ emission line as being Hα. This assumption for the [OIII] line will cause the redshift to be underestimated because the Hβ and [OIII]$\lambda 4959$ lines blueward of [OIII]$\lambda 5007$ will lower the redshift estimate. Using this we found the agreement to be -127 ± 204 km·sec^{-1} compared with estimates based on the $H\alpha 12/H\alpha 8$ vs. $H\alpha 12/H\alpha 16$ values determined from the look up table described in chapter 2.

Though we have been able to obtain a few spectra, to completely establish the method, and to more fully determine the galaxy density of the void, many more spectra are needed. We hope to

get time on a large telescope within the next year to allow us to get the spectra on all of the $H\alpha$ emission candidates, and begin to get spectra on the objects in the 1σ and 2σ objects. After defining the density of objects throughout voids we will be able to constrain dark matter models. If there is a population of dwarf galaxies through the void, then it confirms the standard model of cold dark matter. However, if there is not a dwarf galaxy population then some alternate dark matter, such as warm dark matter or self-interacting dark matter must be considered. If there are dwarf galaxies in the void, these objects will be the most isolated galaxies known. Studying them will lead to a better understanding of galaxy formation and evolution.

Appendix A

Example Stellar Spectra through $H\alpha$ Bandpasses

This contains spectra of six stars of most concern for causing false positives instead of detecting emission line galaxies. Each of these show that the spectrum of the stars compared to the three transmission profiles of the three redshifted $H\alpha$ filters. This shows that these stars will not be detected in our method.
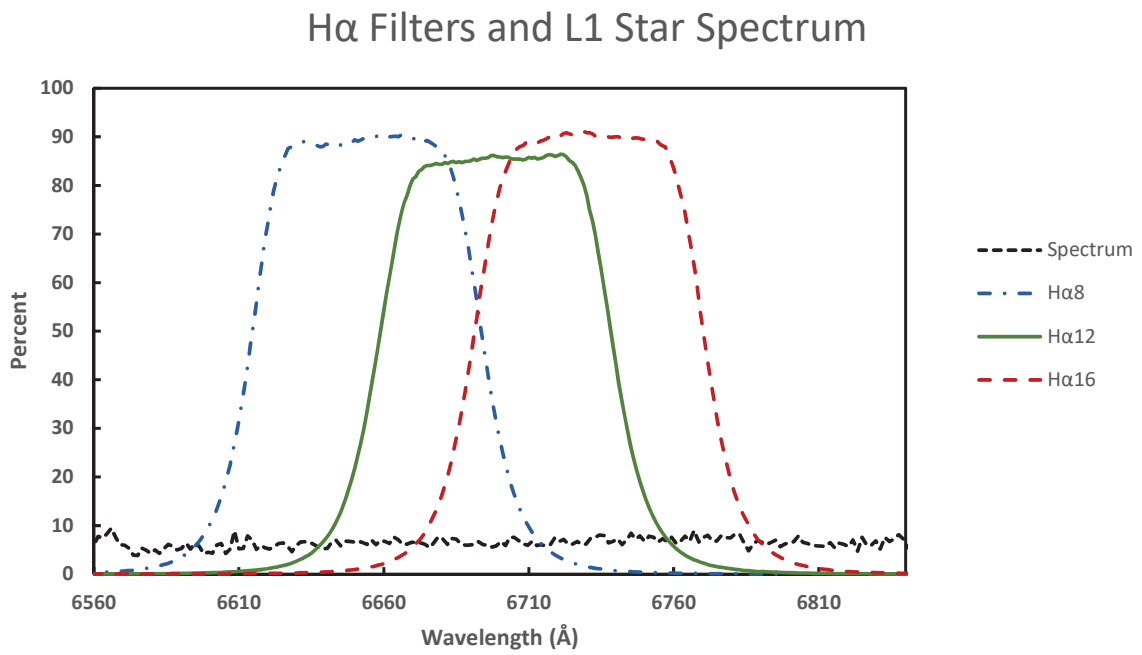
Figure A.1 The spectrum of an L1 star taken from Zehavi et al. (2002).
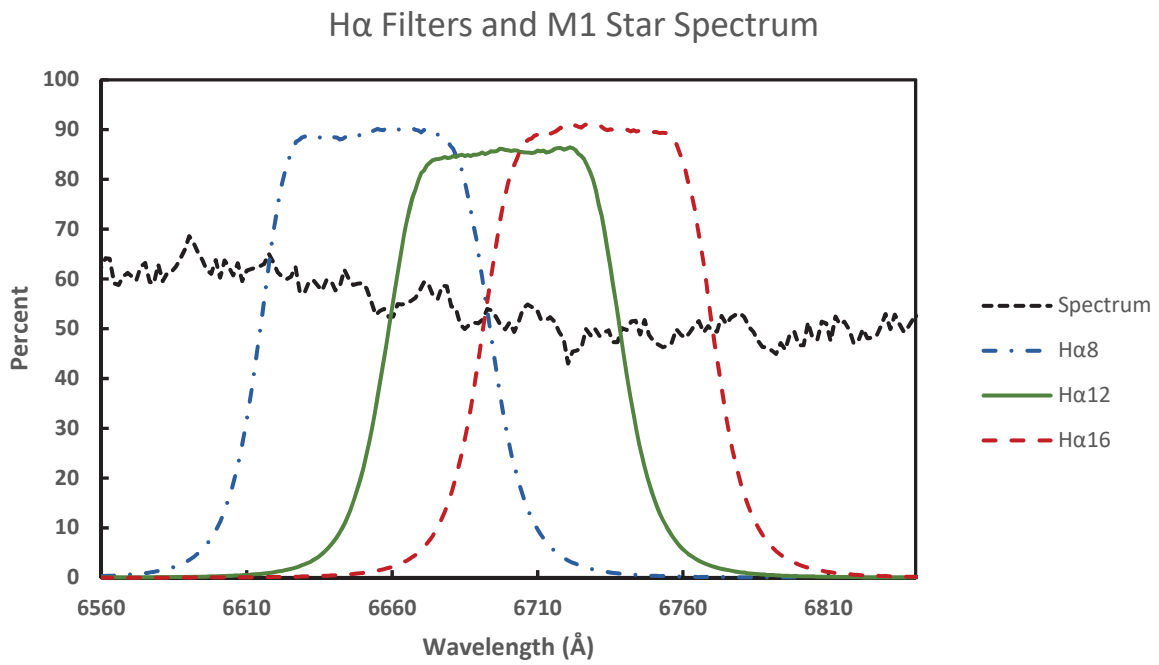
Figure A.2 The spectrum of an M1 star taken from Zehavi et al. (2002).
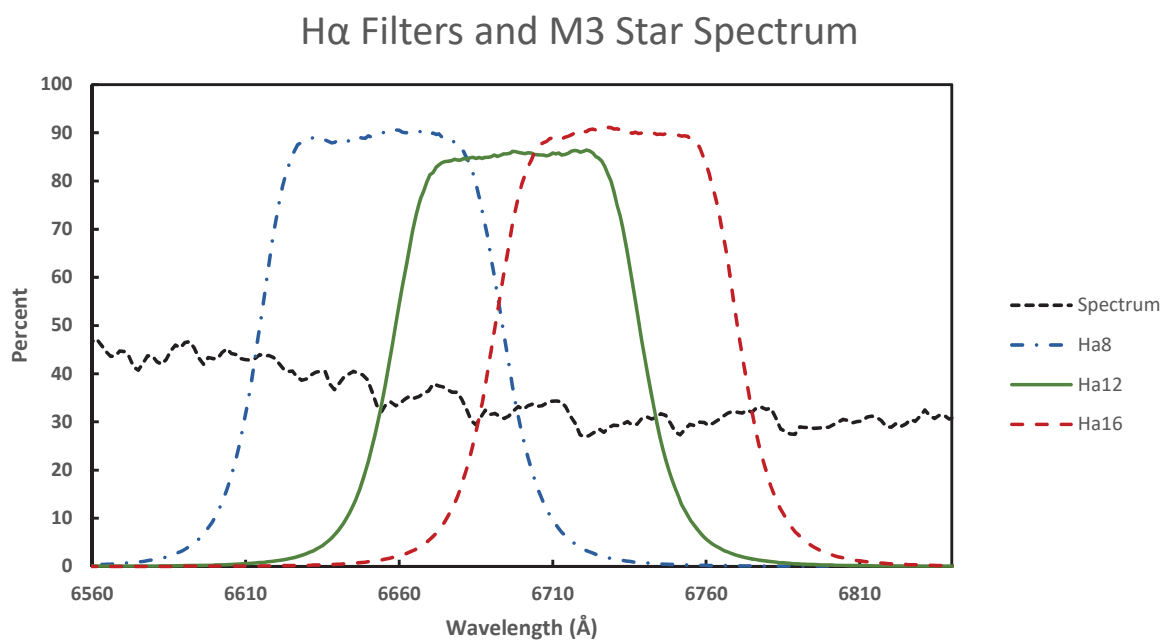
Figure A.3 The spectrum of an M3 star taken from Zehavi et al. (2002).
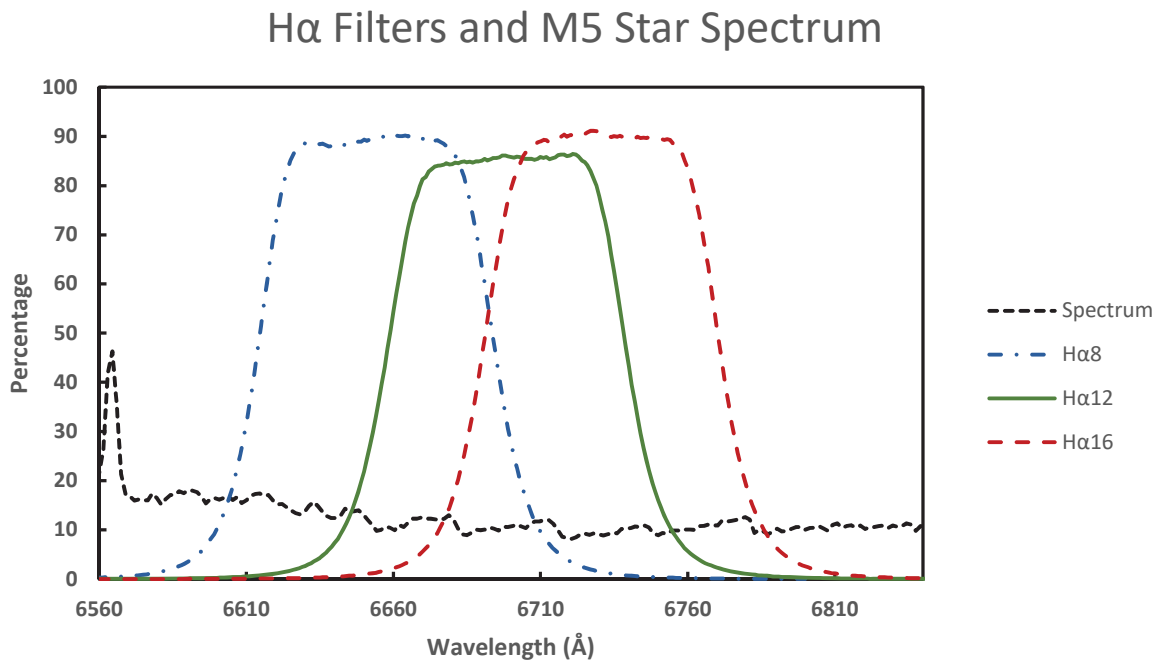
Figure A.4 The spectrum of an M5 star taken from Zehavi et al. (2002).

Hα Filters and M8 Star Spectrum
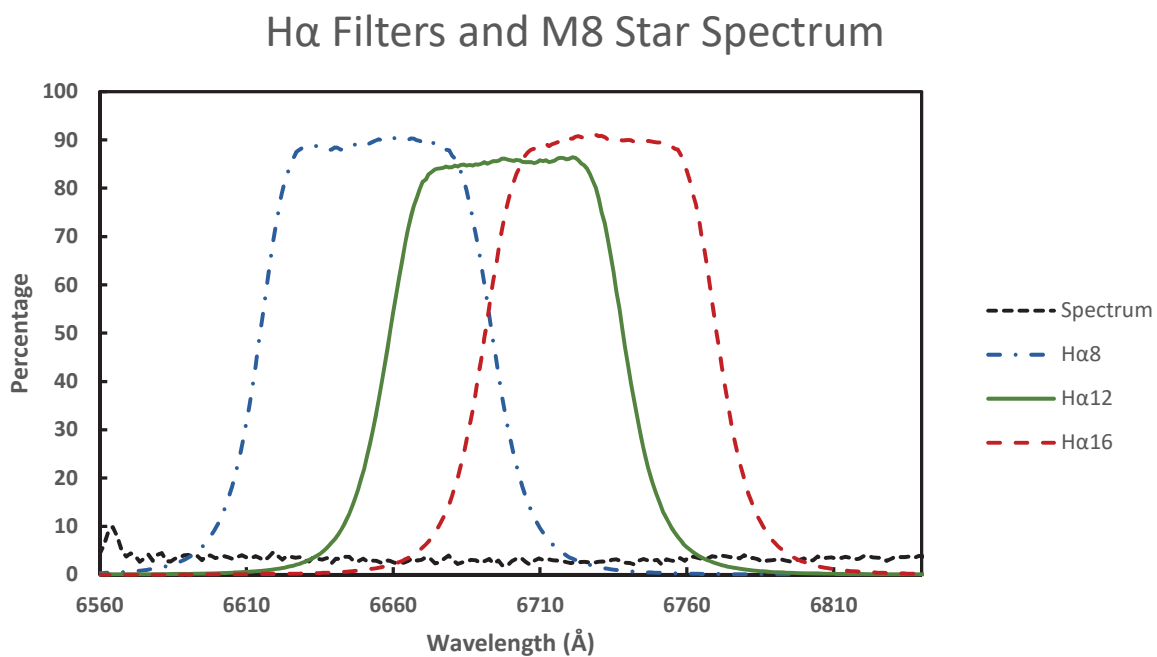
Figure A.5 The spectrum of an M8 star taken from Zehavi et al. (2002).
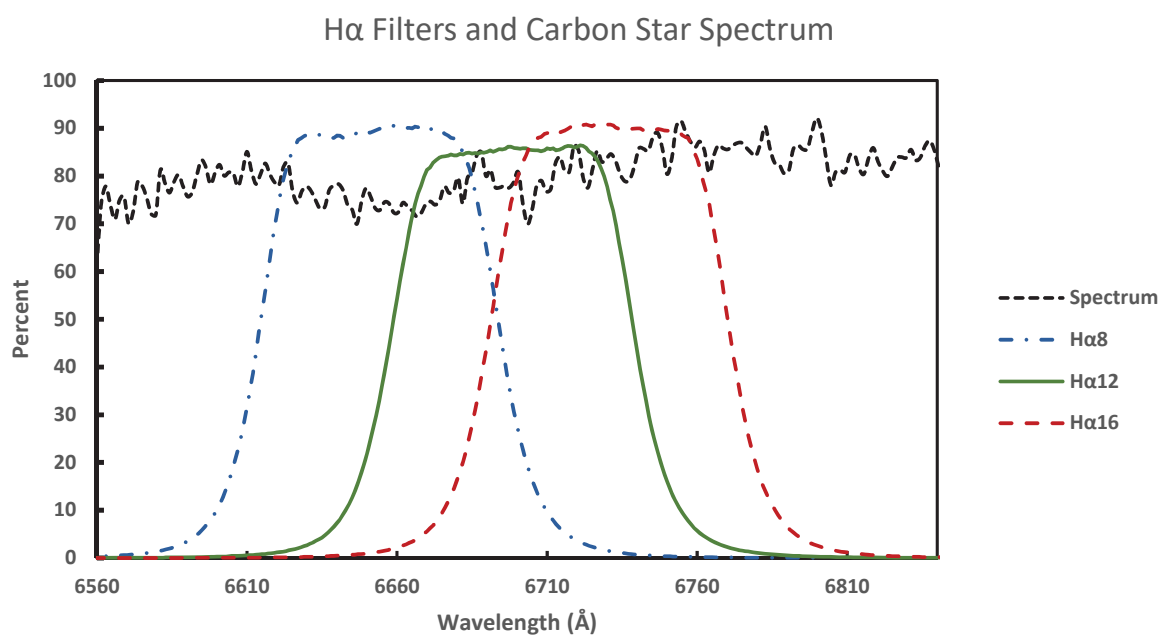
Figure A.6 The spectrum of a Carbon star taken from Zehavi et al. (2002).

Appendix B

EW Look-up Table

This is the look-up table for the equivalent width based off the values of the ratios $H\alpha12/H\alpha8$ and $H\alpha12/H\alpha16$. Any entry that is blank are from values where the errors were too large.

Table B.1 Equivalent-width Look-up Table: Part 1

$\frac{H\alpha12}{H\alpha16}$ → $\frac{H\alpha12}{H\alpha8}$ ↓	0.95	1.00	1.05	1.10	1.15	1.20	1.25	1.30	1.35	1.40	1.45
0.25										341.2	368.8
0.30								258.1	285.0	309.7	332.2
0.35							217.5	238.9	259.2	278.7	297.1
0.40						181.8	199.4	216.4	232.8	248.7	264.0
0.45					145.4	158.9	172.3	185.6	198.9	212.1	225.1
0.50					122.6	133.5	144.5	155.6	166.8	177.9	189.2
0.55				98.6	105.9	113.5	121.4	129.6	138.0	146.6	155.5
0.60				80.3	85.6	91.2	97.2	103.5	110.1	117.0	124.2
0.65			61.7	64.8	68.3	72.2	76.4	81.0	85.9	91.2	96.7
0.70			49.1	50.9	53.2	55.8	58.8	62.1	65.8	69.8	74.2
0.75			38.5	39.6	41.1	42.9	45.1	47.7	50.7	53.9	57.5
0.80			29.7	30.7	32.1	33.8	35.9	38.3	41.1	44.3	47.7
0.85		23.5	24.4	25.7	27.4	29.5	32.0	34.9	38.2	41.8	45.7
0.90		15.4	18.0	21.0	24.5	28.3	32.4	37.0	41.9	47.1	52.6
0.95		8.1	13.4	19.1	25.2	31.7	38.5	45.7	53.3	61.1	69.2
1.00	0.0	4.7	13.1	22.0	31.4	41.3	51.5	62.2	73.2	84.6	96.4
1.05	2.3	8.4	16.3	25.9	37.1	49.7	63.6	78.7	94.8	111.9	129.8
1.10	14.7	15.0	19.9	29.0	41.9	58.3	77.8	99.9	124.3	150.5	178.2

Table B.2 Equivalent-width Look-up Table: Part 2

$\frac{H\alpha 12}{H\alpha 16}$ $\frac{H\alpha 12}{H\alpha 8}$	1.5	1.55	1.6	1.65	1.7	1.75	1.8	1.85	1.9	1.95	2
0.25	392.4	412.3	428.8	442.3	453.0	461.4	467.7	472.2	475.4	477.4	478.7
0.30	352.6	371.1	387.8	402.7	416.0	427.8	438.1	447.1	454.9	461.5	467.2
0.35	314.7	331.3	346.9	361.6	375.5	388.3	400.3	411.4	421.6	430.9	439.2
0.40	278.7	292.9	306.6	319.8	332.4	344.7	356.4	367.7	378.6	389.0	399.1
0.45	238.1	250.9	263.6	276.0	288.4	300.5	312.4	324.1	335.6	346.8	357.7
0.50	200.4	211.7	222.9	234.1	245.3	256.4	267.5	278.5	289.3	300.1	310.8
0.55	164.6	173.8	183.2	192.8	202.4	212.2	222.1	232.1	242.1	252.1	262.2
0.60	131.6	139.2	147.1	155.1	163.4	171.8	180.5	189.2	198.1	207.1	216.2
0.65	102.6	108.7	115.1	121.8	128.7	135.9	143.2	150.8	158.5	166.5	174.6
0.70	78.9	83.8	89.1	94.6	100.5	106.5	112.8	119.4	126.1	133.1	140.3
0.75	61.5	65.7	70.2	75.1	80.2	85.5	91.1	97.0	103.1	109.5	116.0
0.80	51.5	55.6	60.0	64.6	69.6	74.8	80.3	86.0	91.9	98.1	104.5
0.85	50.0	54.6	59.5	64.7	70.2	76.0	82.0	88.2	94.7	101.5	108.4
0.90	58.4	64.6	71.0	77.7	84.6	91.8	99.2	106.8	114.7	122.7	130.9
0.95	77.7	86.4	95.3	104.5	114.0	123.6	133.5	143.5	153.7	164.0	174.5
1.00	108.4	120.8	133.4	146.3	159.4	172.7	186.2	199.8	213.6	227.5	241.5
1.05	148.5	167.7	187.4	207.4	227.6	247.9	268.2	288.4	308.3	327.8	346.8
1.10	207.1	236.6	266.4	296.1	325.3	353.7	380.8	406.2	429.5	450.4	468.4

Table B.3 Equivalent-width Look-up Table: Part 3

$\frac{H\alpha12}{H\alpha16}$ $\frac{H\alpha12}{H\alpha8}$	2.05	2.1	2.15	2.2	2.25	2.3	2.35	2.4	2.45	2.5	2.55
0.25	479.6	480.3	481.3	482.8							
0.30	471.9	475.9	479.1	481.8	484.0						
0.35	446.7	453.4	459.1	464.0	468.0	471.2	473.5	475.0	475.6	475.4	
0.40	408.7	418.0	426.9	435.4	443.6	451.5	459.1	466.3	473.3	480.1	486.5
0.45	368.4	378.7	388.8	398.5	407.9	417.0	425.6	433.9	441.8	449.3	456.4
0.50	321.3	331.7	341.9	352.0	361.8	371.5	380.9	390.2	399.1	407.7	416.3
0.55	272.3	282.3	292.4	302.3	312.3	322.1	331.8	341.4	350.9	360.2	369.3
0.60	225.4	234.7	244.0	253.4	262.7	272.2	281.6	290.9	300.3	309.6	318.8
0.65	182.8	191.2	199.7	208.3	217.0	225.8	234.7	243.6	252.5	261.5	270.5
0.70	147.7	155.2	162.9	170.8	178.8	186.9	195.1	203.5	211.9	220.5	229.1
0.75	122.8	129.7	136.9	144.2	151.7	159.3	167.1	175.0	183.0	191.2	199.4
0.80	111.1	117.9	124.9	132.1	139.4	146.9	154.5	162.3	170.2	178.2	186.3
0.85	115.5	122.8	130.3	137.9	145.7	153.6	161.7	169.8	178.1	186.4	194.8
0.90	139.3	147.8	156.4	165.2	174.1	183.1	192.2	201.4	210.6	219.8	229.1
0.95	185.1	195.8	206.6	217.5	228.4	239.4	250.4	261.4	272.4	283.5	294.4
1.00	255.6	269.8	284.0	298.1	312.3	326.5	340.6	354.6	368.5	382.3	396.0
1.05	365.2	382.8	399.5	415.3	429.9	443.3	455.3	465.9	474.9	482.1	487.5
1.10	483.2	494.4	501.5	504.3							

Table B.4 Equivalent-width Look-up Table: Part 4

$\frac{H\alpha 12}{H\alpha 16}$	2.05	2.1	2.15	2.2	2.25	2.3	2.35	2.4	2.45	2.5	2.55
$\frac{H\alpha 12}{H\alpha 8}$											
0.25	479.6	480.3	481.3	482.8							
0.30	471.9	475.9	479.1	481.8	484.0						
0.35	446.7	453.4	459.1	464.0	468.0	471.2	473.5	475.0	475.6	475.4	
0.40	408.7	418.0	426.9	435.4	443.6	451.5	459.1	466.3	473.3	480.1	486.5
0.45	368.4	378.7	388.8	398.5	407.9	417.0	425.6	433.9	441.8	449.3	456.4
0.50	321.3	331.7	341.9	352.0	361.8	371.5	380.9	390.2	399.1	407.7	416.3
0.55	272.3	282.3	292.4	302.3	312.3	322.1	331.8	341.4	350.9	360.2	369.3
0.60	225.4	234.7	244.0	253.4	262.7	272.2	281.6	290.9	300.3	309.6	318.8
0.65	182.8	191.2	199.7	208.3	217.0	225.8	234.7	243.6	252.5	261.5	270.5
0.70	147.7	155.2	162.9	170.8	178.8	186.9	195.1	203.5	211.9	220.5	229.1
0.75	122.8	129.7	136.9	144.2	151.7	159.3	167.1	175.0	183.0	191.2	199.4
0.80	111.1	117.9	124.9	132.1	139.4	146.9	154.5	162.3	170.2	178.2	186.3
0.85	115.5	122.8	130.3	137.9	145.7	153.6	161.7	169.8	178.1	186.4	194.8
0.90	139.3	147.8	156.4	165.2	174.1	183.1	192.2	201.4	210.6	219.8	229.1
0.95	185.1	195.8	206.6	217.5	228.4	239.4	250.4	261.4	272.4	283.5	294.4
1.00	255.6	269.8	284.0	298.1	312.3	326.5	340.6	354.6	368.5	382.3	396.0
1.05	365.2	382.8	399.5	415.3	429.9	443.3	455.3	465.9	474.9	482.1	487.5
1.10	483.2	494.4	501.5	504.3							

Table B.5 Equivalent-width Look-up Table: Part 5

$\frac{H\alpha12}{H\alpha16}$ / $\frac{H\alpha12}{H\alpha8}$	2.6	2.65	2.7	2.75	2.8	2.85	2.9	2.95	3
0.25									
0.30									
0.35									
0.40	492.8	498.8	504.6	510.2					
0.45	463.0	469.2	474.9	480.1	484.8	489.0	492.7	495.9	498.4
0.50	424.4	432.3	439.8	447.0	453.9	460.4	466.6	472.4	477.8
0.55	378.3	387.0	395.5	403.8	411.8	419.5	426.9	434.0	440.8
0.60	328.0	337.0	346.0	354.8	363.5	372.1	380.4	388.6	396.6
0.65	279.5	288.5	297.5	306.4	315.3	324.1	332.8	341.5	350.0
0.70	237.8	246.5	255.2	264.0	272.8	281.6	290.4	299.2	307.9
0.75	207.8	216.2	224.7	233.2	241.8	250.5	259.2	267.9	276.6
0.80	194.5	202.8	211.2	219.6	228.1	236.7	245.3	253.9	262.5
0.85	203.3	211.8	220.4	229.0	237.6	246.2	254.8	263.4	271.9
0.90	238.5	247.8	257.1	266.5	275.7	285.0	294.2	303.3	312.4
0.95	305.4	316.3	327.1	337.8	348.4	358.9	369.3	379.5	389.5
1.00	409.5	422.8	435.9	448.8	461.4	473.8	485.9	497.6	509.1
1.05	490.9								
1.10									

Table B.6 Equivalent-width Look-up Table: Part 6

$\frac{H\alpha 12}{H\alpha 16}$	0.95	1.00	1.05	1.10	1.15	1.20	1.25	1.30	1.35	1.40	1.45
$\frac{H\alpha 12}{H\alpha 8}$											
1.15	18.0	8.2	26.2	42.5	61.6	90.3	103.9	135.3	161.9	205.5	231.0
1.20	22.4	12.5	33.9	55.3	76.5	112.9	139.3	182.0	221.7	270.4	303.7
1.25	26.8	18.5	43.3	70.2	94.3	138.7	183.0	239.1	295.3	348.1	390.9
1.30	31.4	26.4	54.4	87.3	115.0	167.7	235.3	307.0	383.9	439.3	493.6
1.35	36.0	35.8	67.1	106.3	138.5	199.8	296.8	386.5	488.3	544.7	
1.40	40.7	46.7	81.4	127.2	164.9	234.8	368.1	478.3	609.7		
1.45	45.5	59.0	97.0	149.8	194.2	272.8	449.6	582.9			
1.50	50.4	72.6	114.1	174.0	226.4	313.5	541.8				
1.55	55.4	87.4	132.4	199.8	261.5	357.1	645.3				
1.60	60.5	103.2	151.9	226.8	299.5	403.2	760.7				
1.65	65.7	119.9	172.6	255.1	340.4	452.0					
1.70	71.1	137.5	194.3	284.6	384.3	503.2					
1.75	76.5	155.7	217.0	315.0	431.1	556.9					
1.80	82.1	174.5	240.6	346.3	480.8						
1.85	87.8	193.8	265.1	378.3	533.6						
1.90	93.6	213.5	290.3	411.0	589.3						
1.95	99.5	233.3	316.1	444.2							
2.00	105.6	253.3	342.6	477.7							
2.05	111.8	273.3	369.6	511.5							

Table **B.7** Equivalent-width Look-up Table: Part 7

$\frac{H\alpha 12}{H\alpha 16}$	1.5	1.55	1.6	1.65	1.7	1.75	1.8	1.85	1.9	1.95	2
$\frac{H\alpha 12}{H\alpha 8}$											
1.15	285.1	329.5	352.4	374.7	441.0	471.6	480.4				
1.20	378.2	426.9	460.6	485.9							
1.25	489.8										
1.30											

Table B.8 Equivalent-width Look-up Table: Part 8

$\frac{H\alpha12}{H\alpha16}$ / $\frac{H\alpha12}{H\alpha8}$	0.95	1.00	1.05	1.10	1.15	1.20	1.25	1.30	1.35	1.40	1.45
2.10	118.2	293.2	397.0	545.5							
2.15	124.7	312.9	424.9								
2.20	131.4	332.2	453.0								
2.25	138.3	351.0	481.3								
2.30	145.2	369.3	509.8								
2.35	152.4	386.9	538.3								
2.40	159.7	403.7									
2.45	167.2	419.5									
2.50	174.9	434.4									
2.55	182.8	448.0									
2.60	190.8	460.4									
2.65	199.1	471.5									
2.70	207.5	481.0									
2.75	216.1	488.9									
2.80	225.0	495.1									
2.85	234.0	499.4									
2.90	243.3	501.8									
2.95	252.7	502.1									
3.00	262.4	500.2									

Appendix C

cz Look-up Table

This is the look-up table for the cz based off the values of the ratios $H\alpha12/H\alpha8$ and $H\alpha12/H\alpha16$.

Any entry that is blank are from values where the errors were too large.

Table C.1 cz Look-up Table: Part 1

$\frac{H\alpha 12}{H\alpha 16}$	0.95	1.00	1.05	1.10	1.15	1.20	1.25	1.30	1.35
$\frac{H\alpha 12}{H\alpha 8}$									
0.25									
0.30								3327.3	3343.4
0.35							3394.4	3403.5	3412.7
0.40						3207.8	3256.2	3300.1	3339.7
0.45					3226.1	3274.0	3318.4	3359.4	3397.2
0.50				3205.9	3261.1	3312.4	3359.9	3403.6	3443.9
0.55			3251.7	3324.9	3390.5	3449.0	3500.8	3546.7	3587.0
0.60			3348.4	3415.3	3475.4	3529.1	3576.9	3619.2	3656.5
0.65			3518.4	3559.5	3597.5	3632.6	3665.0	3694.8	3722.2
0.70		3256.8	3383.9	3491.4	3581.5	3656.6	3718.6	3769.3	3810.4
0.75		3540.5	3599.3	3653.3	3702.8	3748.0	3789.3	3826.8	3860.9
0.80		3416.4	3525.6	3623.0	3709.6	3786.0	3853.2	3911.7	3962.3
0.85		3659.5	3733.5	3800.8	3861.9	3917.0	3966.7	4011.2	4051.0
0.90		3652.5	3765.1	3866.2	3956.6	4036.9	4107.9	4170.2	4224.5
0.95		4086.1	4152.9	4213.9	4269.4	4319.9	4365.6	4406.9	4444.2
1.00		5128.4	5109.7	5093.5	5079.5	5067.7	5057.8	5049.8	5043.5
1.05		5826.2	5695.3	5585.1	5494.0	5420.4	5362.7	5319.2	5288.4
1.10		5788.2	5702.2	5630.8	5572.6	5526.2	5490.1	5463.0	5443.4
1.15		5920.9	5789.1	5688.8	5615.7	5565.4	5533.8	5516.6	5509.5

Table C.2 cz Look-up Table: Part 2

$\frac{H\alpha 12}{H\alpha 16}$ $\rightarrow$ $\frac{H\alpha 12}{H\alpha 8}$ $\downarrow$	1.4	1.45	1.5	1.55	1.6	1.65	1.7	1.75	1.8
0.25	3205.0	3198.5	3200.2	3210.1	3228.2	3254.5	3289.0	3331.8	3382.7
0.30	3358.7	3373.0	3386.6	3399.2	3411.0	3421.9	3431.9	3441.1	3449.4
0.35	3421.7	3430.8	3439.8	3448.7	3457.6	3466.4	3475.2	3483.9	3492.6
0.40	3375.2	3406.8	3434.9	3459.5	3481.1	3499.8	3515.8	3529.5	3541.0
0.45	3431.8	3463.5	3492.3	3518.5	3542.1	3563.3	3582.3	3599.2	3614.1
0.50	3480.8	3514.4	3545.1	3572.8	3597.8	3620.2	3640.1	3657.8	3673.4
0.55	3622.2	3652.9	3679.3	3702.0	3721.4	3737.7	3751.5	3762.9	3772.4
0.60	3689.2	3717.8	3742.5	3763.8	3782.0	3797.5	3810.6	3821.5	3830.6
0.65	3747.4	3770.4	3791.4	3810.6	3828.1	3844.1	3858.5	3871.6	3883.5
0.70	3843.5	3869.9	3890.8	3907.3	3920.4	3930.7	3939.2	3946.3	3952.6
0.75	3891.8	3919.6	3944.7	3967.2	3987.4	4005.4	4021.4	4035.6	4048.2
0.80	4005.8	4042.7	4073.7	4099.4	4120.3	4137.1	4150.1	4160.1	4167.3
0.85	4086.4	4117.7	4145.3	4169.5	4190.5	4208.7	4224.3	4237.6	4248.9
0.90	4271.4	4311.5	4345.5	4373.8	4397.0	4415.7	4430.2	4441.2	4449.0
0.95	4477.6	4507.7	4534.5	4558.4	4579.7	4598.5	4615.2	4630.0	4643.0
1.00	5038.8	5035.5	5033.6	5032.9	5033.2	5034.5	5036.5	5039.3	5042.5
1.05	5268.7	5258.4	5256.1	5259.9	5268.4	5280.0	5293.0	5305.9	5317.0
1.10	5429.9	5421.1	5415.6	5411.9	5408.7	5404.5	5397.8	5387.4	5371.7
1.15	5508.2	5508.5	5506.0	5496.6	5476.0	5439.9	5384.0	5304.0	

Table C.3 cz Look-up Table: Part 3

$\frac{H\alpha 12}{H\alpha 16}$ / $\frac{H\alpha 12}{H\alpha 8}$	1.85	1.9	1.95	2	2.05	2.1	2.15	2.2	2.25
0.25									
0.30	3456.8	3463.3	3469.0	3473.8	3477.8	3480.8	3483.0	3484.4	3484.8
0.35	3501.2	3509.8	3518.3	3526.8	3535.2	3543.6	3551.9	3560.2	3568.4
0.40	3550.6	3558.6	3565.1	3570.5	3575.0	3578.8	3582.1	3585.2	3588.4
0.45	3627.2	3638.7	3648.6	3657.2	3664.5	3670.7	3676.0	3680.4	3684.3
0.50	3686.9	3698.7	3708.8	3717.5	3724.7	3730.8	3735.8	3740.0	3743.4
0.55	3780.2	3786.6	3791.9	3796.3	3799.9	3803.1	3805.9	3808.5	3811.1
0.60	3838.2	3844.5	3849.6	3854.0	3857.7	3860.9	3863.8	3866.6	3869.3
0.65	3894.2	3903.9	3912.7	3920.6	3927.8	3934.4	3940.3	3945.7	3950.7
0.70	3958.4	3964.1	3969.9	3975.9	3982.3	3989.0	3996.1	4003.6	4011.2
0.75	4059.3	4069.1	4077.8	4085.4	4092.2	4098.1	4103.4	4108.2	4112.5
0.80	4172.2	4175.3	4176.9	4177.4	4177.1	4176.4	4175.4	4174.5	4173.9
0.85	4258.3	4266.2	4272.7	4278.0	4282.3	4285.8	4288.7	4291.0	4293.0
0.90	4454.1	4456.8	4457.6	4456.8	4454.8	4451.8	4448.2	4444.2	4440.0
0.95	4654.5	4664.7	4673.7	4681.7	4688.9	4695.4	4701.3	4706.7	4711.8
1.00	5046.2	5050.1	5054.2	5058.3	5062.2	5065.9	5069.2	5072.0	5074.1
1.05	5324.7	5327.4	5323.6	5311.6	5289.8	5256.6	5210.5	5149.7	5072.7
1.10	5349.4	5319.0	5279.2	5228.4					
1.15									

Table C.4 cz Look-up Table: Part 4

$\frac{H\alpha 12}{H\alpha 16}$ $\frac{H\alpha 12}{H\alpha 8}$	2.3	2.35	2.4	2.45	2.5	2.55	2.6	2.65	2.7
0.25									
0.30									
0.35	3576.6	3584.7	3592.8	3600.8	3608.8				
0.40	3591.9	3595.9	3600.7	3606.5	3613.6	3622.2	3632.5	3644.9	3659.4
0.45	3687.6	3690.6	3693.3	3696.0	3698.7	3701.6	3704.9	3708.8	3713.2
0.50	3746.3	3748.7	3750.9	3753.0	3755.1	3757.4	3760.1	3763.3	3767.2
0.55	3813.7	3816.5	3819.5	3822.8	3826.4	3830.3	3834.5	3838.9	3843.6
0.60	3872.2	3875.2	3878.6	3882.3	3886.4	3890.9	3895.9	3901.3	3907.2
0.65	3955.3	3959.5	3963.5	3967.2	3970.8	3974.3	3977.6	3980.8	3984.0
0.70	4019.0	4026.7	4034.1	4041.2	4047.8	4053.7	4058.7	4062.7	4065.7
0.75	4116.4	4120.1	4123.5	4126.8	4130.0	4133.2	4136.4	4139.5	4142.8
0.80	4173.7	4174.2	4175.5	4177.6	4180.7	4184.9	4190.1	4196.4	4203.8
0.85	4294.8	4296.5	4298.1	4299.9	4301.7	4303.8	4306.2	4308.8	4311.8
0.90	4436.0	4432.3	4429.0	4426.3	4424.5	4423.5	4423.4	4424.4	4426.5
0.95	4716.6	4721.2	4725.7	4730.1	4734.5	4738.9	4743.4	4747.8	4752.3
1.00	5075.5	5075.9	5075.3	5073.5	5070.3	5065.8	5059.6	5051.7	5042.0
1.05									

Table C.5 cz Look-up Table: Part 5

$\frac{H\alpha 12}{H\alpha 16}$	2.75	2.8	2.85	2.9	2.95	3
$\frac{H\alpha 12}{H\alpha 8}$						
0.25						
0.30						
0.35						
0.40	3676.5					
0.45	3718.5	3724.7	3732.0	3740.5	3750.4	3761.8
0.50	3771.9	3777.6	3784.4	3792.5	3802.1	3813.2
0.55	3848.5	3853.4	3858.2	3862.8	3867.1	3870.9
0.60	3913.5	3920.1	3926.9	3934.0	3941.1	3948.2
0.65	3987.2	3990.3	3993.5	3996.6	3999.7	4002.8
0.70	4067.6	4068.4	4068.1	4066.9	4064.8	4062.2
0.75	4146.0	4149.4	4152.8	4156.3	4159.9	4163.4
0.80	4212.1	4221.4	4231.6	4242.4	4253.7	4265.4
0.85	4315.2	4318.9	4322.9	4327.3	4331.9	4336.8
0.90	4429.6	4433.9	4439.2	4445.5	4452.7	4460.9
0.95	4756.8	4761.2	4765.6	4769.9	4774.0	4777.8
1.00	5030.4	5016.6	5000.5	4982.2	4961.3	4937.7
1.05						

Table **C.6** cz Look-up Table: Part 6

$\frac{H\alpha 12}{H\alpha 16}$	0.95	1.00	1.05	1.10	1.15	1.20	1.25	1.30	1.35
$\frac{H\alpha 12}{H\alpha 8}$									
1.20		5996.8	5887.1	5791.8	5710.8	5644.1	5591.8	5553.9	5530.3
1.25		6041.7	5913.9	5805.3	5715.8	5645.4	5594.3	5562.3	5549.4
1.30		6030.8	5913.9	5817.0	5740.1	5683.2	5646.3	5629.4	5632.4
1.35		6057.0	5936.1	5837.0	5759.6	5704.0	5670.1	5658.0	5667.6
1.40		6108.1	5992.7	5898.0	5838.5	5737.8	5704.1	5689.6	5729.6
1.45		6134.1	6015.6	5918.3	5847.0	5742.7	5729.9	5780.0	
1.50		6157.0	6034.3	5934.5	5851.0	5753.2	5773.1		
1.55		6177.1	6049.2	5947.3	5853.7	5775.5	5842.2		
1.60		6194.6	6060.8	5957.4	5858.6	5816.0			
1.65		6209.7	6069.6	5965.7	5868.8	5880.8			
1.70		6222.5	6076.0	5972.9	5887.9				
1.75		6233.2	6080.5	5979.9	5919.0				
1.80		6242.0	6083.6	5987.4	5965.7				
1.85		6249.2	6085.7	5996.2					
1.90		6254.8	6087.4	6007.1					
1.95		6259.2	6089.0	6020.8					
2.00		6262.4	6091.0	6038.2					
2.05		6264.7	6093.9						

Table C.7 cz Look-up Table: Part 7

$\frac{H\alpha12}{H\alpha16}$ $\frac{H\alpha12}{H\alpha8}$	1.4	1.45	1.5	1.55	1.6	1.65	1.7	1.75	1.8
1.20	5521.1	5526.2	5545.7	5579.6	5627.8	5690.3			
1.25	5555.7	5581.2	5625.8	5689.6	5772.6				
1.30	5655.5	5698.5	5761.6						
1.35	5699.0								

Table C.8 cz Look-up Table: Part 8

$\frac{H\alpha 12}{H\alpha 16}$ $\frac{H\alpha 12}{H\alpha 8}$	0.95	1.00	1.05	1.10	1.15	1.20	1.25	1.30	1.35
2.10		6266.2	6098.2						
2.15		6267.2	6104.2						
2.20		6267.9	6112.6						
2.25		6268.3	6123.7						
2.30		6268.8							
2.35		6269.4							
2.40		6270.5							
2.45		6272.1							
2.50		6274.5							
2.55		6277.8							
2.60		6282.3							
2.65		6288.2							
2.70		6295.5							
2.75		6304.6							
2.80		6315.5							
2.85		6328.6							
2.90		6343.9							
2.95		6361.7							
3.00		6382.2							

Appendix D

$H\alpha$ Candidate Objects

The table for the emission line candidate objects found in the survey in the $H\alpha$ region. The columns are the Field designation, ID, RA, Dec, r' magnitude, equivalent width and cz of the objects. Entries which are blank are not listed because they fall within a region of large error on the look-up table from Chapter 2.

Field	ID	RA	Dec	r'	EW (Å)	cz (km·s^{-1})
FN8-74	12783	13:13:28.446	72 °43'01.906"	23.3	195	4300
FN8-74	20280	13:13:32.278	72 °57'52.557"	22.4		
FN8-74	13993	13:11:11.503	72 °45'8.622"	23	210	4200
FN8-63	12974	13:3:29.223	73 °24'59.824"	26.2		3800
FN8-63	10903	13:3:19.059	73 °19'55.135"	27		4200
FN8-63	3857	12:59:57.453	73 °05'4.278"	27.3		
FN8-63	13682	12:59:56.617	73 °26'35.753"	25		4000
FN8-54	14139	12:53:1.616	72 °55'43.476"	26		

Field	ID	RA	Dec	r'	EW (Å)	cz (km·s^{-1})
FN8-74	12783	13:13:28.446	72°43'01.906"	23.3	195	4300
FN8-74	20280	13:13:32.278	72°57'52.557"	22.4		
FN8-74	13993	13:11:11.503	72°45'8.622"	23	210	4200
FN8-63	12974	13:3:29.223	73°24'59.824"	26.2		3800
FN8-63	10903	13:3:19.059	73°19'55.135"	27		4200
FN8-63	3857	12:59:57.453	73°05'4.278"	27.3		
FN8-63	13682	12:59:56.617	73°26'35.753"	25		4000
FN8-54	14139	12:53:1.616	72°55'43.476"	26		
FN8-53	4906	12:48:52.314	73°06'19.575"	21.8	290	6100
FN8-53	5811	12:47:59.666	73°08'15.489"	23.4	290	6100
FN8-45	10718	12:37:46.732	72°05'28.135"	23.2	440	5400
FN8-45	16341	12:41:14.5	72°17'55.159"	16.1	360	5800
FN8-45	6206	12:42:43.449	71°53'40.352"	18.5		
FN8-43	3414	12:36:19.528	73°4'26.73"	22.1	135	6200
FN8-43	11538	12:36:54.459	73°22'38.774"	23.4	350	3700
FN8-43	5593	12:38:56.514	73°08'43.138"	22.8	340	6000
FN8-43	19995	12:39:52.647	73°36'32.729"	23.7		
FN8-43	17313	12:43:19.63	73°35'35.295"	23.2	480	6000
FN8-43	18649	12:43:20.051	73°37'15.281"	22.3	315	6100
FN2-23	8651	3:43:8.247	17°22'44.029"	22.3		44
FN2-22	9153	3:42:0.052	18°3'25.232"	24		4400
FN2-22	11910	3:42:0.09	18°13'54.222"	24.4		
FN2-13	6099	3:39:4.078	17°14'40.457"	23.3		3800

Appendix E

1σ Objects

The table for all objects found in the 1σ region of the color-color plot. The columns are the Field designation, ID, RA, Dec, r' magnitude, equivalent width and cz of the objects. Entries which are blank are not listed because they fall within a region of large error on the look-up table from Chapter 2.

Field	ID	RA	Dec	r'	EW (Å)	cz (km·s^{-1})
FN8-74	9716	13:13:5.751	72°37'11.512"	22.7	210	
FN8-74	3007	13:6:22.353	72°23'3.89"	23.5		
FN8-74	4156	13:12:46.634	72°26'0.643"	22.4		
FN8-74	4709	13:8:51.833	72°26'50.904"	22.3	760	
FN8-74	9530	13:11:50.081	72°36'40.366"	22.7	380	5500
FN8-64	12992	13:2:45.168	72°39'40.016"	22.9		
FN8-64	16541	12:57:24.813	72°45'16.713"	22.7		
FN8-64	20433	12:58:8.591	72°51'46.457"	23.1		

Field	ID	RA	Dec	r'	EW (Å)	cz (km·s^{-1})
FN8-64	12030	13:1:7.36	72°37'57.891"	21		
FN8-64	5824	12:59:47.656	72°27'24.018"	22.6		
FN8-64	5602	12:58:34.532	72°26'55.513"	22.8		
FN8-64	16796	13:0:21.411	72°45'54.034"	23.2		
FN8-64	11937	13:1:27.798	72°37'47.56"	22.4		4300
FN8-64	20349	12:58:18.923	72°51'35.123"	22.3		6100
FN8-64	3746	13:0:54.945	72°23'44.284"	22.7		6100
FN8-64	6388	12:56:33.345	72°28'11.017"	23		
FN8-64	16842	13:0:5.992	72°45'58.604"	23.8		
FN8-63	9712	13:00:29.7	73°17'12.164	22.3	260	4600
FN8-63	12181	13:00:32.53	73°23'12.718	22.7		5300
FN8-63	11687	13:02:24.869	73°21'58.735	22.1		4400
FN8-54	9917	12:47:35.708	72°46'8.313	22.2	1140	4300
FN8-54	6272	12:47:50.757	72°36'36.908	22.2	880	4400
FN8-54	7066	12:48:11.078	72°38'49.397	22.5	910	5400
FN8-74	9716	13:13:5.751	72°37'11.512"	22.7	210	
FN8-74	3007	13:6:22.353	72°23'3.89"	23.5		
FN8-74	4156	13:12:46.634	72°26'0.643"	22.4		
FN8-74	4709	13:8:51.833	72°26'50.904"	22.3	760	
FN8-74	9530	13:11:50.081	72°36'40.366"	22.7	380	5500
FN8-64	12992	13:2:45.168	72°39'40.016"	22.9		
FN8-64	16541	12:57:24.813	72°45'16.713"	22.7		

Field	ID	RA	Dec	r'	EW (Å)	cz (km·s^{-1})
FN8-64	20433	12:58:8.591	72°51'46.457"	23.1		
FN8-64	12030	13:1:7.36	72°37'57.891"	21		
FN8-64	5824	12:59:47.656	72°27'24.018"	22.6		
FN8-64	5602	12:58:34.532	72°26'55.513"	22.8		
FN8-64	16796	13:0:21.411	72°45'54.034"	23.2		
FN8-64	11937	13:1:27.798	72°37'47.56"	22.4		4300
FN8-64	20349	12:58:18.923	72°51'35.123"	22.3		6100
FN8-64	3746	13:0:54.945	72°23'44.284"	22.7		6100
FN8-64	6388	12:56:33.345	72°28'11.017"	23		
FN8-64	16842	13:0:5.992	72°45'58.604"	23.8		
FN8-63	9712	13:00:29.7	73°17'12.164	22.3	260	4600
FN8-63	12181	13:00:32.53	73°23'12.718	22.7		5300
FN8-63	11687	13:02:24.869	73°21'58.735	22.1		4400
FN8-54	9917	12:47:35.708	72°46'8.313	22.2	1140	4300
FN8-54	6272	12:47:50.757	72°36'36.908	22.2	880	4400
FN8-54	7066	12:48:11.078	72°38'49.397	22.5	910	5400
FN8-43	11988	12:39:22.468	73°23'27.994	22.4	310	5800
FN8-43	12856	12:39:26.986	73°25'17.595	20.2	40	4200
FN8-43	17466	12:39:40.611	73°35'28.897	22.3		
FN8-43	2430	12:40:48.703	73°2'12.076	22.7		
FN8-43	7004	12:41:16.322	73°11'30.872	23.3		
FN8-43	15531	12:42:02.357	73°31'5.724	22.4		

Field	ID	RA	Dec	r'	EW (Å)	cz (km·s^{-1})
FN8-43	7157	12:42:07.503	73°11'43.487	22.6	260	6000
FN8-43	17718	12:42:09.39	73°34'35.828	21.6	100	4600
FN8-43	8742	12:42:11.674	73°15'17.494	22.3		
FN8-43	19577	12:42:12.726	73°37'10.92	22.5		
FN8-43	3831	12:42:23.565	73°4'39.444	22.2	210	6300
FN8-43	9212	12:42:50.395	73°16'20.761	22.6		6100
FN8-34	20170	12:27:51.817	72°57'54.855	22.9	500	6400
FN8-34	11052	12:32:27.21	72°41'24.08	23.4	100	4400
FN8-34	11500	12:32:37.54	72°42'22.411	22.4	110	4600
FN8-34	4185	12:32:44.661	72°25'57.66	20.6		
FN2-33	6064	3:45:37.647	17°14'58.389"	19.4		3700
FN2-32	5251	3:44:0.875	17°50'13.051"	21.1	260	4600
FN2-23	7253	3:41:52.176	17°17'46.944"	22.4		
FN2-23	8316	3:41:15.262	17°21'31.226"	21.9		5800
FN2-22	9164	3:41:10.619	18°3'25.759"	20.4		5600
FN2-22	11932	3:41:21.03	18°13'57.115"	20.2	500	5100
FN2-13	2747	3:40:0.852	17°2'55.52"	21.6		4000
FN2-13	4799	3:38:22.529	17°10'11.774"	22.3		
FN2-13	10091	3:38:33.463	17°27'59.07"	21.6		

Appendix F

2σ Objects

The table for all objects found in the 2σ region of the color-color plot, which are not in the 1σ region. All of the 1σ objects also fall within the 2σ region. The columns are the Field designation, ID, RA, Dec, r' magnitude, equivalent width and cz of the objects. Entries which are blank are not listed because they fall within a region of large error on the look-up table from Chapter 2.

Field	ID	RA	Dec	r'	EW (Å)	cz (km·s^{-1})
FN8-74	11290	13:6:49.478	72°39'33.898"	22.3		
FN8-74	13225	13:9:45.108	72°43'30.208"	22.2		
FN8-74	13419	13:11:21.094	72°44'0.348"	23.1	310	4500
FN8-74	18469	13:11:26.202	72°54'20.798"	22.3		
FN8-74	19127	13:12:58.39	72°55'16.217"	20.8	30	5900
FN8-74	3436	13:8:42.078	72°24'14.149"	22.5		
FN8-74	4623	13:11:59.41	72°26'55.96"	21.8		
FN8-74	4837	13:11:52.163	72°27'14.987"	21.8		

Field	ID	RA	Dec	r'	EW (Å)	cz (km·s^{-1})
FN8-74	6422	13:12:35.689	72°30'21.077"	22.7	550	
FN8-74	9084	13:10:52.905	72°35'36.045"	22.2		
FN8-74	14391	13:11:14.337	72°46'0.348"	22.6		
FN8-74	18705	13:13:29.297	72°54'56.949"	22.6		
FN8-74	20192	13:13:27.065	72°57'41.374"	21.5	240	6100
FN8-74	2476	13:9:18.512	72°22'29.025"	22.2		
FN8-74	2509	13:11:4.036	72°22'44.915"	22.8	380	5400
FN8-74	4764	13:11:31.268	72°27'14.03"	22.8		
FN8-74	8760	13:8:24.566	72°34'44.58"	22.6		
FN8-74	9714	13:13:47.6	72°37'10.039"	22.6	150	5000
FN8-74	10916	13:6:6.935	72°38'44.793"	22.4		5700
FN8-74	10982	13:7:48.069	72°39'7.71"	22.2	190	5300
FN8-74	11162	13:10:40.448	72°39'44.002"	22.5	330	5400
FN8-74	14704	13:9:45.373	72°46'33.778"	22.4		
FN8-74	15069	13:9:19.191	72°47'23.451"	22.8	450	5900
FN8-74	15745	13:7:55.139	72°48'40.942"	22.9		
FN8-74	16596	13:8:45.533	72°50'36.056"	22.7		
FN8-64	3389	13:1:42.996	72°23'10.666"	21.9		
FN8-64	3647	12:58:10.013	72°23'27.462"	23.6		5900
FN8-64	3697	13:0:6.568	72°23'41.17"	22.5		6200
FN8-64	4118	12:58:49.756	72°24'21.887"	22.8		
FN8-64	4598	13:1:52.596	72°25'17.641"	22.6	500	5000

Field	ID	RA	Dec	r'	EW (Å)	cz (km·s^{-1})
FN8-64	4756	12:59:17.392	72°25'30.276"	21.8		
FN8-64	5060	12:57:32.873	72°25'52.25"	23.4		
FN8-64	5723	12:58:7.516	72°27'8.793"	19.1		5300
FN8-64	5903	13:0:39.733	72°27'31.492"	22.8		
FN8-64	6416	12:56:16.533	72°28'8.836"	24		5900
FN8-64	6454	13:3:16.309	72°28'32.3"	22.4		
FN8-64	7337	12:59:50.697	72°30'2.619"	23.9		6100
FN8-64	7471	13:0:49.549	72°30'15.663"	22.4		
FN8-64	8175	13:0:38.841	72°31'19.959"	22.8		5900
FN8-64	8458	12:56:58.448	72°31'37.383"	23.2		5300
FN8-64	8541	13:2:53.614	72°31'57.363"	22.2		
FN8-64	9289	13:1:16.638	72°33'13.497"	22.2		6300
FN8-64	9385	12:58:12.411	72°33'13.13"	22.5	260	4600
FN8-64	9585	12:59:53.667	72°33'31.715"	22.7		3400
FN8-64	10418	12:58:54.483	72°35'3.632"	24.1		5900
FN8-64	10613	12:58:3.079	72°35'21.007"	21.2		
FN8-64	11973	12:58:14.092	72°37'43.252"	22.4		
FN8-64	12195	12:59:10.532	72°38'6.44"	21.9		
FN8-64	12331	12:58:38.762	72°38'23.769"	22.8		4200
FN8-64	12883	13:0:2.005	72°39'26.482"	22.5		5700
FN8-64	13625	13:3:18.458	72°40'28.711"	21.2		4400
FN8-64	13784	12:57:5.297	72°40'47.053"	22.4		4100

Field	ID	RA	Dec	r'	EW (Å)	cz (km·s^{-1})
FN8-64	14235	12:57:58.842	72°41'13.237"	21.9	260	
FN8-64	15876	13:2:44.653	72°44'24.52"	23.1		3800
FN8-64	16300	13:0:24.622	72°45'5.114"	23.7		
FN8-64	17328	13:0:24.382	72°46'48.108"	22.5		
FN8-64	17532	13:0:51.724	72°47'10.664"	22.7		
FN8-64	18288	13:1:10.609	72°48'24.413"	23		
FN8-64	18572	12:59:31.995	72°48'50.901"	24		
FN8-64	20351	13:2:43.151	72°51'46.046"	22.1		5800
FN8-64	20362	13:1:24.53	72°51'46.025"	22.6		
FN8-64	21325	13:3:56.199	72°53'19.402"	24.4		5900
FN8-64	21833	13:1:38.432	72°54'10.578"	22.7		
FN8-64	22385	12:56:35.587	72°54'53.513"	22.7		4300
FN8-64	22495	12:56:46.416	72°55'7.521"	21.8		3900
FN8-64	25585	12:57:47.138	72°57'9.005"	22.3		5600
FN8-63	11069	13:03:44.911	73°20'21.798"	22.5		
FN8-63	8313	13:03:40.833	73°14'7.942"	22.7		6000
FN8-63	11567	13:03:36.911	73°21'37.578"	21.7		5900
FN8-63	14327	13:03:36.563	73°28'1.58"	22.5		4300
FN8-63	2724	13:03:13.868	73°3'1.774"	22.3		6200
FN8-63	5272	13:03:6.358	73°7'51.474"	22.9		3800
FN8-63	17329	13:02:54.954	73°34'24.189"	22.8		
FN8-63	3079	13:02:52.643	73°3'40.286"	21.8		

Field	ID	RA	Dec	r'	EW (Å)	cz (km·s^{-1})
FN8-63	2225	13:02:34.612	73°2'14.613"	22.9		
FN8-63	13674	13:02:29.498	73°26'36.162"	22.2	260	4600
FN8-63	7442	13:02:12.49	73°12'16.877"	22.1		
FN8-63	17062	13:02:5.202	73°33'51.37"	22.5		5600
FN8-63	16346	13:02:4.347	73°32'20.884"	21.8		5400
FN8-63	12741	13:01:51.001	73°24'30.47"	22.3		5400
FN8-63	5153	13:01:31.938	73°7'38.48"	22.1		
FN8-63	10393	13:01:25.19	73°18'48.938"	22.5	500	5100
FN8-63	14319	13:01:23.147	73°28'0.9"	22.9		
FN8-63	7044	13:01:19.445	73°11'26.409"	22.9		
FN8-63	8133	13:01:17.426	73°13'46.892"	22.5		4200
FN8-63	17205	13:01:2.283	73°34'7.178"	23.3		6400
FN8-63	16342	13:00:49.767	73°32'23.009"	22.5		4200
FN8-63	6660	13:00:48.598	73°10'37.037"	22.3		5400
FN8-63	19979	13:00:44.96	73°38'11.394"	22.1		
FN8-63	4653	13:00:38.366	73°6'40.349"	22.8		3800
FN8-63	20290	13:00:37.732	73°36'33.771"	22.6		5300
FN8-63	8135	13:00:32.141	73°13'46.22"	22.4		5300
FN8-63	15952	13:00:27.359	73°31'35.078"	22.2		
FN8-63	14671	13:00:21.589	73°28'47.952"	21.6		6100
FN8-63	15603	13:00:16.726	73°30'50.322"	22.1		5400
FN8-63	14683	13:00:13.846	73°28'52.253"	22.4		4100

Field	ID	RA	Dec	r'	EW (Å)	cz (km·s^{-1})
FN8-63	6519	13:00:13.381	73°10'19.259"	22.2	260	4700
FN8-63	20417	13:00:8.344	73°37'33.063"	22.5		3800
FN8-63	10136	13:00:5.029	73°18'14.022"	22.4		5300
FN8-63	16614	12:59:26.653	73°32'50.648"	22.8		
FN8-63	9897	12:59:24.265	73°17'39.561"	22.1	500	4900
FN8-63	5809	12:58:33.018	73°8'49.482"	22.6	500	5100
FN8-63	6485	12:58:27.008	73°10'12.135"	22.3		
FN8-63	15416	12:58:22.4	73°30'25.42"	23.1		
FN8-63	3658	12:58:4.112	73°4'40.659"	22.6		
FN8-63	2671	12:57:37.979	73°2'48.795"	21.9	500	5000
FN8-63	14439	12:57:29.073	73°28'8.796"	22.6		3900
FN8-63	20326	12:57:27.618	73°35'49.212"	22.8		5600
FN8-63	20049	12:57:18.444	73°36'35.506"	21.8		5400
FN8-63	10836	12:57:10.129	73°19'41.746"	22.6		
FN8-63	6189	12:56:38.986	73°9'28.93"	23	500	5000
FN8-63	16115	12:56:36.937	73°31'38.964"	21.8		5500
FN8-63	12196	12:56:36.731	73°22'58.37"	22.6		4300
FN8-63	2659	12:56:18.139	73°2'33.345"	21.5		4200
FN8-63	6357	12:56:17.154	73°9'44.847"	22.7		5500
FN8-63	9827	12:56:15.829	73°17'14.315"	22.3		
FN8-54	8392	12:46:35.708	72°42'9.809"	22.9	590	4400
FN8-54	4575	12:46:42.168	72°31'58.491"	22.5	930	

Field	ID	RA	Dec	r'	EW (Å)	cz (km·s^{-1})
FN8-54	9912	12:46:42.257	72°46'8.971"	22.8		
FN8-54	1560	12:47:5.567	72°23'48.514"	22.6	760	5900
FN8-54	4041	12:47:18.874	72°30'24.179"	22.7	530	6000
FN8-54	12563	12:47:30.233	72°52'48.764"	22.7		
FN8-54	11755	12:47:46.113	72°50'41.871"	22.2	740	5600
FN8-54	1598	12:47:47.116	72°23'58.452"	22.5	820	5900
FN8-54	7212	12:47:49.728	72°39'11.398"	22.1	1250	5600
FN8-54	4759	12:47:54.569	72°32'28.93"	21.9	850	4200
FN8-54	13231	12:48:10.821	72°57'41.382"	22.9		
FN8-54	6527	12:48:15.526	72°37'18.882"	22.6	510	4200
FN8-54	7172	12:48:23.489	72°39'7.829"	22.4	0	6400
FN8-54	13646	12:48:36.074	72°57'37.701"	23		
FN8-54	10547	12:48:38.106	72°47'46.179"	22.5		5900
FN8-54	1580	12:48:51.376	72°23'51.064"	24.7		
FN8-54	3933	12:48:59.098	72°30'3.898"	22.2	570	4300
FN8-54	10542	12:49:5.15	72°47'42.248"	22	1510	5300
FN8-54	7169	12:49:6.527	72°39'5.728"	22.7	510	3900
FN8-54	5265	12:49:14.438	72°33'54.066"	22.7	560	4200
FN8-54	4809	12:49:27.349	72°32'36.243"	22.2		6100
FN8-54	13051	12:49:45.051	72°54'37.709"	22.8		
FN8-54	1977	12:50:11.522	72°24'53.755"	22.6	770	4000
FN8-54	12432	12:50:38.774	72°52'4.03"	21.9	1220	5400

Field	ID	RA	Dec	r'	EW (Å)	cz (km·s^{-1})
FN8-54	8598	12:50:49.03	72°42'35.486"	22.3	510	6000
FN8-54	6121	12:51:4.616	72°36'4.618"	22.1	1100	
FN8-54	13905	12:51:8.57	72°56'42.462"	22.6	730	5000
FN8-54	13493	12:51:18.782	72°57'12.859"	22.4	1130	5200
FN8-54	10512	12:51:41.771	72°47'34.322"	22.4	510	5900
FN8-54	5642	12:51:44.148	72°34'47.599"	22.1	2100	6000
FN8-54	9891	12:51:54.038	72°45'57.951"	23	770	4300
FN8-54	10038	12:52:31.583	72°46'15.523"	23.4		4700
FN8-54	7761	12:52:45.881	72°40'24.239"	22.9		
FN8-54	1716	12:52:54.798	72°24'0.316"	22.3	600	0
FN8-54	6670	12:53:42.006	72°37'22.735"	23		6100
FN8-54	13605	12:53:42.539	72°57'14.464"	21.8		
FN8-53	20989	12:46:4.016	73°37'35.916"	22.8	290	6100
FN8-53	4428	12:46:5.979	73°5'26.516"	22.1		
FN8-53	6557	12:46:8.272	73°9'43.601"	21.7	330	5500
FN8-53	22058	12:46:29.029	73°36'53.683"	22		5800
FN8-53	14941	12:46:50.984	73°26'48.248"	21.7	430	5600
FN8-53	17395	12:47:2.956	73°32'24.95"	22.6		5900
FN8-53	8402	12:47:5.044	73°13'20.531"	22.4	80	4500
FN8-53	3400	12:47:32.444	73°3'26.374"	22.7		5900
FN8-53	14537	12:47:33.241	73°25'59.354"	22.6	440	5400
FN8-53	5088	12:47:34.768	73°6'40.393"	22	250	5300

Field	ID	RA	Dec	r'	EW (Å)	cz (km·s^{-1})
FN8-53	19021	12:47:35.457	73°35'56.323"	22.5		5800
FN8-53	2773	12:47:36.015	73°2'21.403"	22.6	430	5600
FN8-53	8234	12:47:51.699	73°12'58.976"	22.5	460	6300
FN8-53	3724	12:47:53.831	73°3'52.984"	22	470	5200
FN8-53	5811	12:47:59.666	73°8'15.489"	23.4	290	6100
FN8-53	15226	12:48:0.948	73°27'38.954"	22.5	390	5600
FN8-53	3011	12:48:4.469	73°2'44.487"	22.4	350	5400
FN8-53	5169	12:48:33.177	73°6'52.822"	22.4	550	6100
FN8-53	12764	12:48:44.969	73°22'12.169"	23.1		
FN8-53	10323	12:48:57.731	73°17'9.981"	22.4	380	5900
FN8-53	7840	12:48:57.797	73°12'7.483"	21	90	5800
FN8-53	4458	12:49:1.443	73°5'30.917"	22.9	160	5000
FN8-53	16222	12:49:3.143	73°29'52.853"	22.9	290	5500
FN8-53	12635	12:49:9.874	73°21'55.242"	22.6	210	5300
FN8-53	8006	12:49:24.356	73°12'30.413"	23.1	330	5100
FN8-53	7644	12:49:26.042	73°11'57.87"	22.8		6500
FN8-53	17134	12:49:29.37	73°31'53.251"	22.4	210	5300
FN8-53	3652	12:49:29.955	73°3'52.76"	22.1	290	5500
FN8-53	6025	12:49:34.279	73°8'41.144"	21.9		6300
FN8-53	15566	12:49:37.725	73°28'16.531"	22.3		
FN8-53	3951	12:49:41.569	73°4'27.423"	22.8	240	5400
FN8-53	13323	12:49:51.486	73°23'23.111"	22.7	210	6300

Field	ID	RA	Dec	r'	EW (Å)	cz (km·s^{-1})
FN8-53	2998	12:50:17.057	73°2'39.632"	22.5	430	5300
FN8-53	15939	12:50:40.658	73°29'7.111"	22.3	170	5300
FN8-53	13028	12:50:41.977	73°22'38.548"	21.9	470	5200
FN8-53	18058	12:50:44.561	73°33'41.416"	21.6	240	5400
FN8-53	16555	12:50:53.559	73°30'30.47"	22.3		5800
FN8-53	7007	12:51:27.896	73°10'34.457"	22.7		5800
FN8-53	16430	12:52:21.033	73°30'0.323"	20.6	210	5300
FN8-53	12130	12:52:21.134	73°20'45.763"	22	230	5300
FN8-53	14876	12:52:26.224	73°26'30.398"	22.6		
FN8-53	18057	12:52:43.848	73°33'32.496"	21.8		6600
FN8-53	15443	12:53:0.383	73°27'42.524"	20.2	20	6000
FN8-53	16544	12:53:8.552	73°30'19.806"	22.3		5700
FN8-53	16335	12:53:29.066	73°29'51.359"	22	350	5500
FN8-53	6826	12:53:32.664	73°9'55.257"	21.9	110	4600
FN8-53	9863	12:53:34.74	73°16'1.133"	23.1		10000
FN8-53	6781	12:53:40.844	73°9'56.425"	22.9		
FN8-53	9348	12:53:48.473	73°14'50.704"	22.9	320	3500
FN8-45	16248	12:36:06.707	72°17'38.418"	22.6	480	3800
FN8-45	9617	12:36:15.523	72°1'57.361"	22.7		
FN8-45	7497	12:36:26.122	71°56'7.487"	22.2	430	5900
FN8-45	5341	12:36:40.201	71°50'23.69"	22.3	110	4100
FN8-45	13087	12:36:42.673	72°11'24.336"	22.7	260	6000

Field	ID	RA	Dec	r'	EW (Å)	cz (km·s^{-1})
FN8-45	6285	12:36:54.131	71°52'57.1"	21.6	120	3800
FN8-45	11878	12:36:59.148	72°8'2.413"	16.4		6100
FN8-45	11331	12:37:23.216	72°7'11.165"	22.2	480	6000
FN8-45	10718	12:37:46.732	72°5'28.135"	23.2	440	5400
FN8-45	6961	12:38:01.17	71°55'5.448"	22.3		
FN8-45	8937	12:38:14.541	72°0'34.454"	21.6	200	5900
FN8-45	7502	12:38:19.687	71°56'24.562"	22.7		
FN8-45	10211	12:38:27.048	72°4'5.228"	22	760	5900
FN8-45	13325	12:38:28.012	72°12'13.535"	22.1	90	4400
FN8-45	13991	12:38:34.878	72°13'42.965"	22.3	420	6100
FN8-45	2913	12:38:39.443	71°43'41.935"	22.6		
FN8-45	2928	12:39:00.907	71°43'45.181"	22	400	5100
FN8-45	6913	12:39:01.583	71°54'58.968"	20.9	130	5000
FN8-45	13064	12:39:11.385	72°11'42.955"	22.1	120	3800
FN8-45	17284	12:39:16.835	72°15'39.66"	21.7	480	5200
FN8-45	9160	12:39:18.791	72°1'11.145"	22.1	310	3700
FN8-45	7567	12:39:22.405	71°56'41.99"	22.1	350	5400
FN8-45	8694	12:39:29.451	71°59'55.853"	24.3	150	4300
FN8-45	3130	12:39:32.502	71°44'24.459"	21.1		
FN8-45	13406	12:39:40.212	72°12'38.247"	22.4	760	5900
FN8-45	5681	12:39:43.49	71°51'44.797"	22.3		
FN8-45	4077	12:39:44.723	71°46'56.864"	22.1		5900

Field	ID	RA	Dec	r'	EW (Å)	cz (km·s^{-1})
FN8-45	2249	12:39:53.173	71°42'7.719"	23.5		
FN8-45	7019	12:39:54.708	71°55'30.06"	22.3	100	4400
FN8-45	5821	12:39:55.496	71°52'4.597"	21.1	260	6000
FN8-45	7844	12:40:00.477	71°57'28.693"	22.4		
FN8-45	11043	12:40:11.558	72°6'45.44"	22.5		
FN8-45	2887	12:40:13.791	71°44'0.389"	19.5	40	5500
FN8-45	16620	12:40:33.51	72°16'36.65"	22.6	190	4400
FN8-45	4052	12:40:45.396	71°46'58.436"	22.2	290	6100
FN8-45	16341	12:41:14.5	72°17'55.159"	16.1	360	5800
FN8-45	5655	12:41:20.815	71°51'51.464"	22.3	160	4000
FN8-45	7755	12:41:43.508	71°57'23.195"	23.4	310	4100
FN8-45	6571	12:41:46.991	71°54'24.422"	22.4	280	3400
FN8-45	9264	12:42:06.296	72°1'48.748"	22.3	170	6200
FN8-45	7617	12:42:17	71°57'15.887"	19.6		
FN8-45	3921	12:42:33.129	71°46'46.279"	22.2		5800
FN8-45	3713	12:42:52.384	71°46'17.284"	21.5		
FN8-45	7732	12:43:01.427	71°57'23.239"	22.6	230	3800
FN8-45	9430	12:43:09.98	72°2'21.631"	22.2	170	5000
FN8-45	5536	12:43:12.119	71°51'35.699"	21.8	270	6100
FN8-45	2994	12:43:25.828	71°44'24.744"	21.6	340	5900
FN8-43	7529	12:36:07.84	73°12'55.658"	22.6	480	5200
FN8-43	3119	12:36:13.042	73°3'46.466"	22.2	200	3400

Field	ID	RA	Dec	r'	EW (Å)	cz (km·s^{-1})
FN8-43	3414	12:36:19.528	73°4'26.73"	22.1	140	6200
FN8-43	6351	12:36:29.56	73°10'22.85"	22.3	280	4700
FN8-43	12604	12:37:04.864	73°24'59.267"	22.8	310	6000
FN8-43	5572	12:37:29.937	73°8'43.354"	22.6		
FN8-43	17343	12:37:35.252	73°35'55.103"	22.3		6300
FN8-43	3408	12:37:58.096	73°4'21.554"	23	250	6300
FN8-43	11742	12:38:02.573	73°22'55.354"	22.3		
FN8-43	6309	12:38:12.023	73°10'16.126"	22.5	410	6000
FN8-43	15937	12:38:24.291	73°32'14.852"	22		
FN8-43	8135	12:38:27.269	73°14'16.534"	22.9	590	6100
FN8-43	2912	12:38:28.427	73°3'21.859"	22.7		
FN8-43	3348	12:38:33.42	73°4'7.978"	21.9	60	6100
FN8-43	5335	12:38:33.632	73°8'14.997"	22.4		
FN8-43	15768	12:38:36.8	73°31'56.407"	21.8	340	5900
FN8-43	2795	12:38:43.347	73°3'6.677"	22	140	4500
FN8-43	3283	12:39:04.198	73°4'4.426"	22.8		
FN8-43	4367	12:39:06.511	73°6'13.247"	22.3	360	5800
FN8-43	12494	12:39:11.247	73°24'36.012"	22.7	490	5100
FN8-43	13203	12:39:29.465	73°26'8.372"	22.6	500	6000
FN8-43	19140	12:39:43.984	73°38'15.092"	22.4	230	5100
FN8-43	16300	12:39:50.302	73°33'0.931"	22		
FN8-43	5190	12:39:53.243	73°7'46.82"	22.1		6300

Field	ID	RA	Dec	r'	EW (Å)	cz (km·s^{-1})
FN8-43	7722	12:40:09.762	73°13'7.676"	22.4	230	4700
FN8-43	12503	12:40:12.407	73°24'31.563"	22.7		5900
FN8-43	3325	12:40:24.752	73°3'57.883"	21.1	170	5900
FN8-43	5215	12:40:40.462	73°7'46.658"	22.7	260	5100
FN8-43	12068	12:40:42.369	73°23'28.224"	21.6	190	6100
FN8-43	15113	12:41:01.252	73°30'14.112"	22.2		6400
FN8-43	14643	12:41:08.883	73°29'4.164"	22		
FN8-43	8884	12:41:12.147	73°15'46.493"	22.4		6300
FN8-43	4099	12:41:19.055	73°5'28.884"	23.1	240	3500
FN8-43	3136	12:41:19.28	73°3'29.309"	22.3		5900
FN8-43	9567	12:41:36.568	73°17'22.885"	22.4	760	5900
FN8-43	3299	12:41:37.255	73°3'46.954"	22.4		6500
FN8-43	7603	12:41:38.38	73°12'40.528"	22.6	650	5800
FN8-43	7014	12:41:46.409	73°11'29.417"	23	340	5900
FN8-43	12879	12:41:51.456	73°25'6.575"	20.9	70	5900
FN8-43	12951	12:42:05.799	73°25'18.1"	22.6		
FN8-43	7916	12:42:07.884	73°13'19.479"	22.9		
FN8-43	12351	12:42:18.213	73°23'51.798"	20.8	60	4400
FN8-43	10463	12:42:19.856	73°19'25.434"	22.4		
FN8-43	10135	12:42:25.907	73°18'42.529"	22.6	400	5800
FN8-43	11179	12:42:45.6	73°21'11.657"	23		
FN8-43	2765	12:42:45.907	73°2'32.487"	22.8		

Field	ID	RA	Dec	r'	EW (Å)	cz (km·s^{-1})
FN8-43	3457	12:42:54.102	73°3'51.251"	22.4	340	6100
FN8-43	19701	12:42:56.636	73°36'47.946"	22.6		
FN8-43	3685	12:43:00.134	73°4'14.31"	21.7		
FN8-43	19998	12:43:05.955	73°36'18.486"	22.6		
FN8-43	17313	12:43:19.63	73°35'35.295"	23.2	480	6000
FN8-43	18649	12:43:20.051	73°37'15.281"	22.3	320	6100
FN8-43	7993	12:43:24.205	73°13'14.241"	22	270	3700
FN8-43	6090	12:43:35.515	73°9'8.686"	22.6	560	6100
FN8-43	12279	12:43:51.888	73°23'33.484"	22.5		
FN8-34	15362	12:26:28.394	72°50'42.795"	20.8	30	5800
FN8-34	12785	12:26:40.496	72°44'54.859"	22	270	6100
FN8-34	3605	12:26:47.786	72°24'38.412"	22.4		
FN8-34	17741	12:27:10.176	72°56'44.675"	22.3	90	4300
FN8-34	11633	12:27:45.074	72°42'21.254"	22.5	310	4500
FN8-34	15209	12:28:02.458	72°50'41.956"	21.8		
FN8-34	9118	12:28:24.316	72°36'36.184"	22.4		
FN8-34	7911	12:28:35.567	72°34'11.366"	21.6	50	4100
FN8-34	10799	12:28:45.834	72°40'38.015"	22.3	190	6200
FN8-34	7503	12:29:25.176	72°33'28.742"	22.8	150	4000
FN8-34	3904	12:29:34.829	72°25'28.059"	22.2	300	5400
FN8-34	3193	12:29:51.031	72°24'13.445"	22.1	300	5100
FN8-34	13948	12:30:20.385	72°48'1.353"	22.5	380	5300

Field	ID	RA	Dec	r'	EW (Å)	cz (km·s^{-1})
FN8-34	11736	12:30:20.638	72°42'48.339"	21.6		5800
FN8-34	12067	12:30:23.616	72°43'33.559"	22.8		5900
FN8-34	15454	12:30:39.972	72°51'29.735"	22.2	410	5300
FN8-34	12047	12:30:44.486	72°43'36.992"	22.6		4700
FN8-34	11580	12:30:44.824	72°42'28.509"	23.2	160	3800
FN8-34	6530	12:31:07.852	72°31'25.911"	19.6	20	4200
FN8-34	16713	12:31:11.107	72°54'33.165"	22.3	500	6000
FN8-34	16372	12:31:15.908	72°53'40.43"	23.2	550	6100
FN8-34	16531	12:31:25.131	72°54'6.428"	21.6	100	4400
FN8-34	18621	12:31:39.58	72°56'50.162"	22.6	420	5100
FN8-34	8185	12:31:43.222	72°34'50.793"	19.7	50	4200
FN8-34	14300	12:31:46.382	72°48'57.459"	22.5		
FN8-34	15493	12:31:54.37	72°51'40.323"	22.4	190	4200
FN8-34	10773	12:31:54.812	72°40'42.825"	21.8		
FN8-34	13853	12:32:13.134	72°47'53.08"	21.6	100	4600
FN8-34	15039	12:32:22.086	72°50'35.909"	22.4		
FN8-34	6595	12:32:26.834	72°31'55.079"	22.3		6900
FN8-34	15666	12:32:35.401	72°51'59.35"	22.4	200	4700
FN8-34	6620	12:32:37.932	72°31'59.438"	22.5	490	5700
FN8-34	13093	12:32:47.203	72°46'10.69"	22.7		5700
FN8-34	15610	12:32:53.169	72°51'56.35"	22.9	370	6300
FN8-34	17528	12:33:09.486	72°56'57.726"	22.7	210	4700

Field	ID	RA	Dec	r'	EW (Å)	cz (km·s^{-1})
FN8-34	8497	12:33:10.362	72°35'35.256"	21.2	60	4300
FN8-34	10395	12:33:10.669	72°39'42.754"	19.2	40	6100
FN8-34	20205	12:33:18.875	72°57'48.904"	22	140	4700
FN8-34	11439	12:33:39.44	72°42'14.705"	20.8	150	4500
FN8-34	7659	12:33:47.618	72°34'2.307"	22.6		6900
FN2-33	5065	3:45:17.737	17°10'24.67""	21.3		
FN2-33	5619	3:45:23.589	17°12'53.246""	23.0		
FN2-33	5799	3:46:12.689	17°13'42.486""	21.2		
FN2-33	5829	3:44:19.617	17°13'50.816""	20.9		
FN2-33	6630	3:45:8.284	17°17'4.513""	21.3	500	5000
FN2-33	6759	3:46:8.607	17°17'37.989""	21.5		
FN2-33	10077	3:44:6.069	17°31'11.772""	21.2		
FN2-33	10853	3:44:20.266	17°34'12.744""	21.6		5900
FN2-33	11196	3:45:48.648	17°35'35.388""	20.9		
FN2-33	11219	3:45:33.577	17°35'42.779""	21.3		
FN2-33	13666	3:44:18.526	17°37'7.664""	21.5		5900
FN2-32	3836	3:44:10.58	17°45'15.379""	21.5		5400
FN2-32	4700	3:44:50.192	17°48'9.339""	21.9		3900
FN2-32	5001	3:44:6.787	17°49'13.447""	22.2		5800
FN2-32	5190	3:45:46.719	17°49'54.49""	21.4		4200
FN2-32	5741	3:45:20.801	17°51'56.686""	22.1		5300

Field	ID	RA	Dec	r'	EW (Å)	cz (km·s^{-1})
FN2-32	5942	3:45:50.647	17°52'36.279""	22		4000
FN2-32	7134	3:44:53.499	17°56'47.715""	22		4300
FN2-32	7157	3:45:23.911	17°56'51.54""	21.6		
FN2-32	9077	3:43:55.542	18°3'21.631""	22.1		4200
FN2-32	9130	3:44:41.05	18°3'29.602""	21.5	500	5000
FN2-32	9186	3:45:13.796	18°3'39.45""	22.2		
FN2-32	9252	3:45:52.011	18°3'48.669""	23.1		
FN2-32	9507	3:45:25.202	18°4'35.965""	22.3		5400
FN2-32	9640	3:44:8.418	18°5'2.906""	22.2		5300
FN2-32	10088	3:44:33.469	18°6'50.316""	19.4		5500
FN2-32	10868	3:43:56.129	18°9'1.119""	21.6		4100
FN2-32	11152	3:45:50.735	18°9'43.714""	21.4		
FN2-32	11229	3:44:44.404	18°9'55.991""	22.4	500	5100
FN2-32	11257	3:45:13.662	18°10'2.941""	20.4		5500
FN2-32	11446	3:45:32.822	18°10'35.602""	21.6	260	4600
FN2-32	11879	3:45:58.453	18°11'57.289""	22.5		
FN2-32	12456	3:46:0.093	18°13'35.191""	21.4	500	5000
FN2-32	12575	3:44:51.671	18°14'3.247""	22.6		
FN2-32	12658	3:44:30.441	18°14'15.887""	22.3		4200
FN2-32	12921	3:44:30.376	18°14'55.888""	22.6		4000

Field	ID	RA	Dec	r'	EW (Å)	cz (km·s^{-1})
FN2-32	12989	3:44:14.232	18°15'6.277''''	23.1		4200
FN2-32	13093	3:45:25.728	18°15'21.91''''	22		5300
FN2-32	13222	3:44:44.106	18°15'45.988''''	22.5		5300
FN2-23	3745	3:41:30.241	17°5'18.38''''	21.9		4500
FN2-23	4412	3:41:10.528	17°7'55.188''''	21.3		4400
FN2-23	4526	3:41:32.642	17°8'20.395''''	20	260	4100
FN2-23	4588	3:41:35.188	17°8'26.408''''	22		5800
FN2-23	4647	3:41:41.676	17°8'36.936''''	21.9		5400
FN2-23	5603	3:41:56.154	17°12'8.447''''	18.7		3800
FN2-23	5780	3:41:34.554	17°12'35.903''''	21.7		5600
FN2-23	6451	3:42:3.799	17°15'5.926''''	19.5		5700
FN2-23	6570	3:40:58.843	17°15'20.51''''	21.9		
FN2-23	6632	3:43:2.299	17°15'31.683''''	22.4		
FN2-23	6865	3:41:42.123	17°16'22.93''''	22.3	260	4700
FN2-23	7035	3:41:49.698	17°17'6.444''''	20	500	5100
FN2-23	7179	3:42:56.203	17°17'39.805''''	18.5	500	5100
FN2-23	7579	3:41:25.641	17°18'58.334''''	22.6		4000
FN2-23	7651	3:41:28.503	17°19'18.855''''	19.7	260	4100
FN2-23	7699	3:43:5.221	17°19'18.61''''	22		5600
FN2-23	8525	3:42:13.341	17°22'14.364''''	22.5		
FN2-23	8674	3:41:49.452	17°23'7.431''''	19.3	500	

Field	ID	RA	Dec	r'	EW (Å)	cz (km·s^{-1})
FN2-23	8840	3:41:4.149	17°23'23.575''''	22.2	500	5000
FN2-23	9169	3:41:48.753	17°24'30.927''''	22.2		
FN2-23	10007	3:41:46.096	17°27'29.912''''	20.3		5600
FN2-23	10411	3:42:15.869	17°28'31.825''''	21.9		6200
FN2-23	10469	3:41:25.373	17°28'53.801''''	19.6	260	4100
FN2-23	10947	3:41:44.278	17°30'19.896''''	22.3		5300
FN2-23	11205	3:41:20.474	17°31'14.246''''	22.4		
FN2-23	11461	3:41:14.283	17°32'15.173''''	20.2		
FN2-23	11809	3:41:48.471	17°33'27.388''''	21.8		3400
FN2-23	12512	3:42:37.775	17°35'59.045''''	21.7		
FN2-23	13175	3:42:35.006	17°34'19.094''''	21.7		4000
FN2-23	13604	3:41:28.123	17°33'56.298''''	21.5		5300
FN2-23	14726	3:42:53.828	17°36'28.27''''	21.8		5300
FN2-23	8651	3:43:8.247	17°22'44.029''''	22.3		4400
FN2-22	4803	3:41:33.984	17°45'55.578''''	19.8		5600
FN2-22	5864	3:42:41.143	17°49'27.361''''	22.6		
FN2-22	5955	3:42:43.137	17°49'51.878''''	22.3		3200
FN2-22	6323	3:42:18.829	17°51'32.09''''	19.7	500	5100
FN2-22	6411	3:41:19.327	17°51'55.094''''	20.3		
FN2-22	6936	3:42:30.201	17°54'16.746''''	20.2	500	
FN2-22	7394	3:41:32.457	17°56'2.516''''	20.7		

Field	ID	RA	Dec	r'	EW (Å)	cz (km·s^{-1})
FN2-22	7633	3:41:42.609	17°57'7.308''''	20.3	500	5100
FN2-22	8135	3:41:27.452	17°59'17.854''''	21.6		
FN2-22	8150	3:42:34.038	17°59'23.789''''	19.9		5600
FN2-22	8445	3:42:49.807	18°0'31.921''''	20.7		
FN2-22	8528	3:42:23.904	18°0'49.162''''	21.4		
FN2-22	8759	3:41:56.522	18°1'48.654''''	21.7		
FN2-22	9134	3:42:11.236	18°3'23.956''''	20	500	
FN2-22	9337	3:42:26.695	18°4'2.699''''	22.2	500	4900
FN2-22	9416	3:42:29.534	18°4'25.236''''	20.1		5600
FN2-22	9463	3:41:28.664	18°4'31.886''''	20.6		5700
FN2-22	9777	3:41:53.375	18°5'44.077''''	22		
FN2-22	10740	3:41:51.558	18°9'41.028''''	20.2	260	
FN2-22	11348	3:42:42.911	18°11'44.87''''	20.6		5600
FN2-22	15006	3:41:16.633	18°14'55.956''''	21.9		5800
FN2-22	9193	3:41:30.286	18°3'34.939''''	20.1	500	5100
FN2-13	2767	3:39:36.413	17°2'55.482''''	21.8		
FN2-13	4432	3:39:8.082	17°8'58.36''''	21.8		5300
FN2-13	6149	3:39:34.617	17°14'47.019''''	21.8		5700
FN2-13	6327	3:38:40.105	17°15'24.989''''	21.9		
FN2-13	7074	3:39:59.647	17°18'11.523''''	22.1		
FN2-13	7079	3:40:3.418	17°18'10.858''''	22.2		

Field	ID	RA	Dec	r'	EW (Å)	cz (km·s^{-1})
FN2-13	7263	3:37:55.293	17°18'50.006''''	21.6		
FN2-13	7354	3:39:24.012	17°19'3.865''''	21.8		4300
FN2-13	7455	3:39:31.662	17°19'25.108''''	21.4		
FN2-13	9020	3:39:18.194	17°24'27.027''''	22.5		6000
FN2-13	9193	3:38:43.65	17°25'0.896''''	22.3	500	5100
FN2-13	10026	3:37:55.724	17°27'50.978''''	21.7		4300
FN2-13	10153	3:40:6.655	17°28'8.157''''	22		5800
FN2-13	10893	3:39:28.137	17°30'31.675''''	21.8		6000
FN2-13	11283	3:39:53.63	17°31'45.702''''	21.6		5700
FN2-13	12353	3:39:31.187	17°34'59.039''''	22.8		

Bibliography

Abazajian, K., Adelman-McCarthy, J., & M. Agueros, e. a. 2009, The Astrophysical Journal Supplement, 182, 543

Aghanim, N., et al. 2018, arXiv:1807.06209 [astro-ph.CO]

Alcock, C., et al. 2000, The Astrophysical Journal, 542, 281

Bertin, E., & Arnouts, S. 1996, A&AS, 117, 393

Bond, J. R., Efstathiou, G., & Silk, J. 1980, Physical Review Letters, 45, 1980

Boylan-Kolchin, M., Bullock, J. S., & Kaplinghat, M. 2011, Monthly Notice of the Royal Astronomical Society, 415, L40

Bullock, J. S., & Boylan-Kolchin, M. 2017, Annual Review of Astronomy and Astrophysics, 55, 343

Carlson, E. D., Machacek, M. E., & Hall, L. J. 1992, Astrophysical Journal, 398, 45

Ceccarelli, L., Paz, D., Lares, M., Padilla, N., & Lambas, D. G. 2013, Monthly Notice of the Royal Astronomical Society, 434, 1435

Collaboration, P. Accessed June 1, 2019, http://sci.esa.int/planck/51553-cosmic-microwave-background-seen-by-planck/

—. Accessed June 3, 2019, http://sci.esa.int/planck/51555-planck-power-spectrum-of-temperature-\
  fluctuations-in-the-cosmic-microwave-background/

Colless, M., et al. 2001, Monthly Notice of the Royal Astronomical Society, 328, 1039

Davis, M., Huchra, J., Latham, D. W., & Tonry, J. 1982, Astrophysical Journal, 253, 423

Dawoodbhoy, T., et al. 2018, Monthly Notice of the Royal Astronomical Society, 480, 1740

de Swart, J. G., Bertone, G., & van Dongen, J. 2017, Nature Astronomy, 1

Djorgovski, S., Spinrad, H., McCarthy, P., & Strauss, M. A. 1985, The Astrophysical Journal, 299,
  L1

Foster, C., & Nelson, L. A. 2009, Astrophysical Journal, 699, 1252

Frenk, C. S., & White, S. M. D. 2012, Annalen der Physik, 524, 507

Garrison-Kimmel, S., Boylan-Kolchin, M., Bullock, J. S., & Lee, K. 2014, Monthly Notice of the
  Royal Astronomical Society, 438, 2578

Gregory, S. A., Tifft, W. G., Moody, J. W., Newberry, M. V., & Hall, S. M. 2000, The Astronomical
  Journal, 119, 573

Griffen, B. F., Ji, A., Dooley, G. A., Gomez, F. A., Vogelsberger, M., O'Shea, B. W., & Frebel, A.
  2016, The Astrophysical Journal, 818

Hoyle, F., Rojas, R. R., Vogeley, M. S., & Brinkmann, J. 2005, The Astrophysical Journal, 620, 618

Hoyle, F., & Vogeley, M. S. 2002, The Astrophysical Journal, 566, 641

Kennicutt, R. C. 1992, Astrophysical Journal Supplement, 79, 255

Lewis, D. W. The University of Michigan, 1983, Ph.D. dissertation

Lilly, S. J., Hammer, F., Févre, O. L., & Crampton, D. 1995, The Astrophysical Journal, 455, 75

Matthee, J., Sobral, D., Best, P., Smail, I., Bian, F., Darvish, B., Rottgering, H., & Fan, X. 2017, Monthly Notice of the Royal Astronomical Society, 471, 629

Mihos, C. Accessed June 4, 2019, http://burro.case.edu/Academics/Astr222/Cosmo/Structure/darkmatter.html

Nakamura, O., Fukugita, M., Brinkmann, J., & Schneider, D. P. 2004, The Astrophysical Journal, 127, 2511

Navarro, J. F., Frenk, C. S., & White, S. D. M. 1997, Astrophysical Journal, 490, 495

Ouchi, M., et al. 2018, Publications of the Astronomical Society of Japan, 70, S13

Paillas, E., Lagos, C. D. P., Padilla, N., Tissera, P., Helly, J., & Schaller, M. 2017, Monthly Notice of the Royal Astronomical Society, 470, 4434

Press, W. H., & Schechter, P. 1974, Astrophysical Journal, 187, 425

Rhoads, J., Malhotra, S., Dey, A., Stern, D., Spinrad, H., & Jannuzi, B. 2000, The Astrophysical Journal, 545, L85

Riess, A. G., Casertano, S., Yuan, W., Macri, L. M., & Scolnic, D. 2019, The Astrophysical Journal, 876, 13

Roos, M. 2015, Introduction to Cosmology, 4th edn. (West Sussex, UK: Wiley)

Rubin, V. C., Ford, W. K., & Thonnard, N. 1980, Astrophysical Journal, 238, 471

Schaye, J., et al. 2015, Monthly Notices of the Royal Astronomical Society, 446, 521

Sheth, R. K., Mo, H. J., & Tormen, G. 2001, Monthly Notice of the Royal Astronomical Society, 323, 1

Sobral, D., et al. 2018, Monthly Notices of the Royal Astronomical Society, 477, 2817

Springel, V., et al. 2005, Nature, 435, 629

Thompson, D., Mannucci, F., & Beckwith, S. 1996, Astronomical Journal, 112, 1794

Tollerud, E. J., Boylan-Kolchin, M., & Bullock, J. S. 2014, Monthly Notice of the Royal Astronomical Society, 440, 3511

Valdez, F., & Tody, D. 1998, in Optical Astronomical Instrumentation, Vol. 3355

Valli, M., & Yu, H. B. 2018, Nature Astronomy, 2, 907

Walker, M. G., & Penarrubia, J. 2011, Astrophysical Journal, 742, 20

Weignberg, D. H., Mortonson, M. J., Eisenstein, D. J., Hirata, C., Riess, A. G., & Rozo, E. 2013, Physics Reports, 530, 87

White, S. D. M., Frenk, C. S., & Davis, M. 1983, Astrophysical Journal Letters, 74, L1

White, S. D. M., & Rees, M. J. 1978, Monthly Notice of the Royal Astronomical Society, 183, 341

Yang, L. F., Neyrinck, M. C., Aragon-Calvo, M. A., Falck, B., & Silk, J. 2015, Monthly Notice of the Royal Astronomical Society, 451, 3606

Zehavi, I., et al. 2002, The Astrophysical Journal, 571, 172

Zwicky, F. 1933, Helvetica Physica Acta, 6, 110